

Stellar evolution and nucleosynthesis

- ▶ Instructor: Falk Herwig
- ▶ Goals and learning outcomes
 - Provide an overview of the physics of stars required to calculate stellar evolution models
 - Describe the evolution of a 2Msun star and a 20Msun star in sufficient detail that students can distinguish the different nucleosynthesis burning phases
 - Describe 3D hydrodynamic simulations as an example for a research frontier in stellar evolution (Jones+ 17)
 - Describe convective-reactive nucleosynthesis as an example for research frontier in stellar nucleosynthesis
 - Students will learn how to explore the NuGrid stellar evolution and nucleosynthesis data Set I
- ▶ Computational stellar astrophysics: <http://csa.phys.uvic.ca>



NuGrid stellar data set – II. Stellar yields from H to Bi for stellar models with $M_{\text{ZAMS}} = 1\text{--}25 M_{\odot}$ and $Z = 0.0001\text{--}0.02$

ABSTRACT

We provide here a significant extension of the NuGrid Set 1 models in mass coverage and towards lower metallicity, adopting the same physics assumptions. The combined data set now includes the initial masses $M_{\text{ZAMS}} / M_{\odot} = 1, 1.65, 2, 3, 4, 5, 6, 7, 12, 15, 20, 25$ for $Z = 0.02, 0.01, 0.006, 0.001, 0.0001$ with α -enhanced composition for the lowest three metallicities. These models are computed with the MESA stellar evolution code and are evolved up to the AGB, the white dwarf stage, or until core collapse. The nucleosynthesis was calculated for all isotopes in post-processing with the NuGrid MPPNP code. Explosive nucleosynthesis is based on semi-analytic 1D shock models. Metallicity-dependent mass-loss, convective boundary mixing in low- and intermediate-mass models and H and He core burning massive star models are included. Convective O-C shell mergers in some stellar models lead to the strong production of odd-Z elements P, Cl, K, and Sc. In AGB models with hot dredge-up, the convective boundary mixing efficiency is reduced to accommodate for its energetic feedback. In both low-mass and massive star models at the lowest metallicity, H-ingestion events are observed and lead to *i*-process nucleosynthesis and substantial ^{15}N production. Complete yield data tables, derived data products and online analytic data access are provided.

Resources and prerequisites

- ▶ Some overview papers and resources
 - Herwig's ASTR 501 graduate course, link to book chapters and review articles:
<http://helix.phys.uvic.ca:8080/ASTR501>
- ▶ Textbooks:
 - Kippenhahn & Weigert, Clayton, Rolfs & Rodney, Kavalier & Hansen, Prialnik
- ▶ The most important resource:
 - NASA ADS: <https://ui.adsabs.harvard.edu/#classic-form>
 - astro-ph: <https://arxiv.org/archive/astro-ph/Astrophysics>
 - dept home page: <http://www.uvic.ca/science/physics/research/research/online/index.php>
- ▶ Python
 - basic programming skills in python at the level of PHYS248 (<https://github.com/UVic-CompPhys/physmath248-2018>)
 - Data Science Handbook: <https://github.com/jakevdp/PythonDataScienceHandbook>
- ▶ Other recommended techniques/tools
 - Markdown
 - Slack
- ▶ jupyterhub servers^[1]:
 - ▶ <https://wendi.nugridstars.org>

[1] F. Herwig, R. Andrassy, N. Annau, O. Clarkson, B. Côté, A. D'Sa, S. Jones, B. Moa, J. O'Connell, D. Porter, C. Ritter, and P. Woodward, "Cyberhubs: Virtual Research Environments for Astronomy," *ASTROPHYS J SUPPL S*, vol. 236, no. 1, p. 2, May 2018.

8 Evolution of Solar and Intermediate-Mass Stars

Falk Herwig

Department of Physics and Astronomy, University of Victoria,
Victoria, BC, Canada

1	<i>Introduction</i>	398
2	<i>The Physics for Stellar Evolution</i>	400
3	<i>The Evolution of a $3 M_{\odot}$ Star</i>	405
3.1	Pre-main Sequence to the End of He-Core Burning	407
3.2	Asymptotic Giant Branch Evolution	412
3.2.1	Thermal-Pulse AGB	414
3.2.2	Nucleosynthesis	421
3.2.3	Post-AGB Evolution	430
4	<i>Evolution as a Function of Initial Mass</i>	432
5	<i>Evolution at Low Metallicity and the Dynamical Star</i>	438
5.1	Rotation	438
5.2	Dynamic Interaction of Nuclear Burning with Convection	439
	<i>Acknowledgments</i>	442
	<i>References</i>	442

Outline

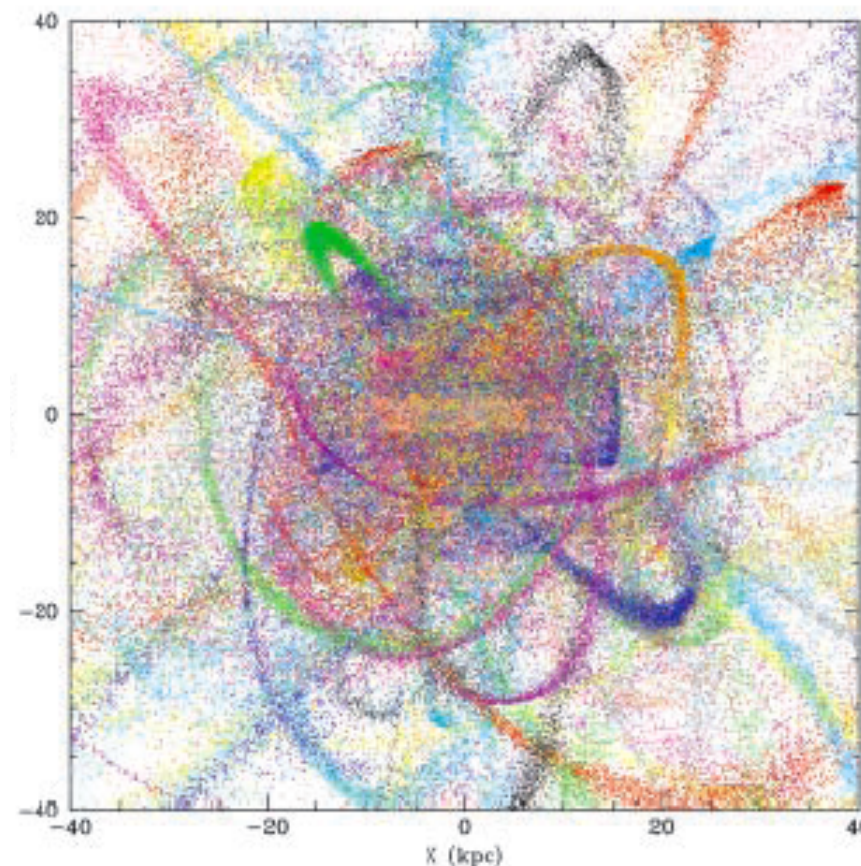
- Introduction
- Part I: Physics for stellar models
- Part II: Stellar models
- Part III: 3D hydro to understand the macrophysics of convection
- Part IV: Convective-reactive nucleosynthesis

Introduction

Why do we care about stellar abundances?

Introduction

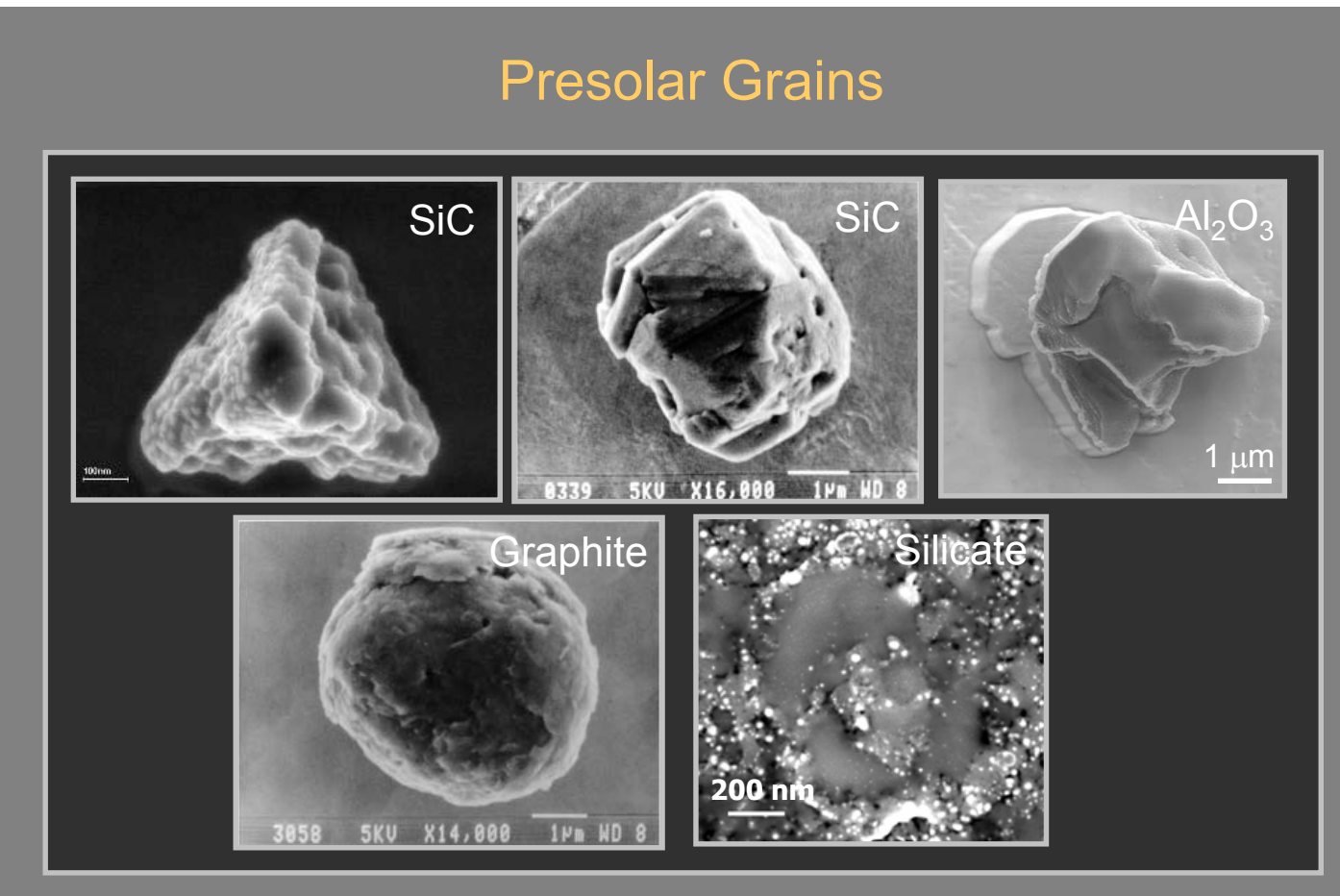
- ▶ One reason to study stars - relation to topics in astronomy and physics
 - how do the elements form
 - stellar physics
 - nuclear physics
 - if we can answer that - use predictive yields as tool for a wide range of astronomy applications:
 - constrain the environment in which the solar system formed
 - investigate the formation and evolution of structure in the Universe
 - determine chemical evolution of galaxies
 - characterize stellar populations



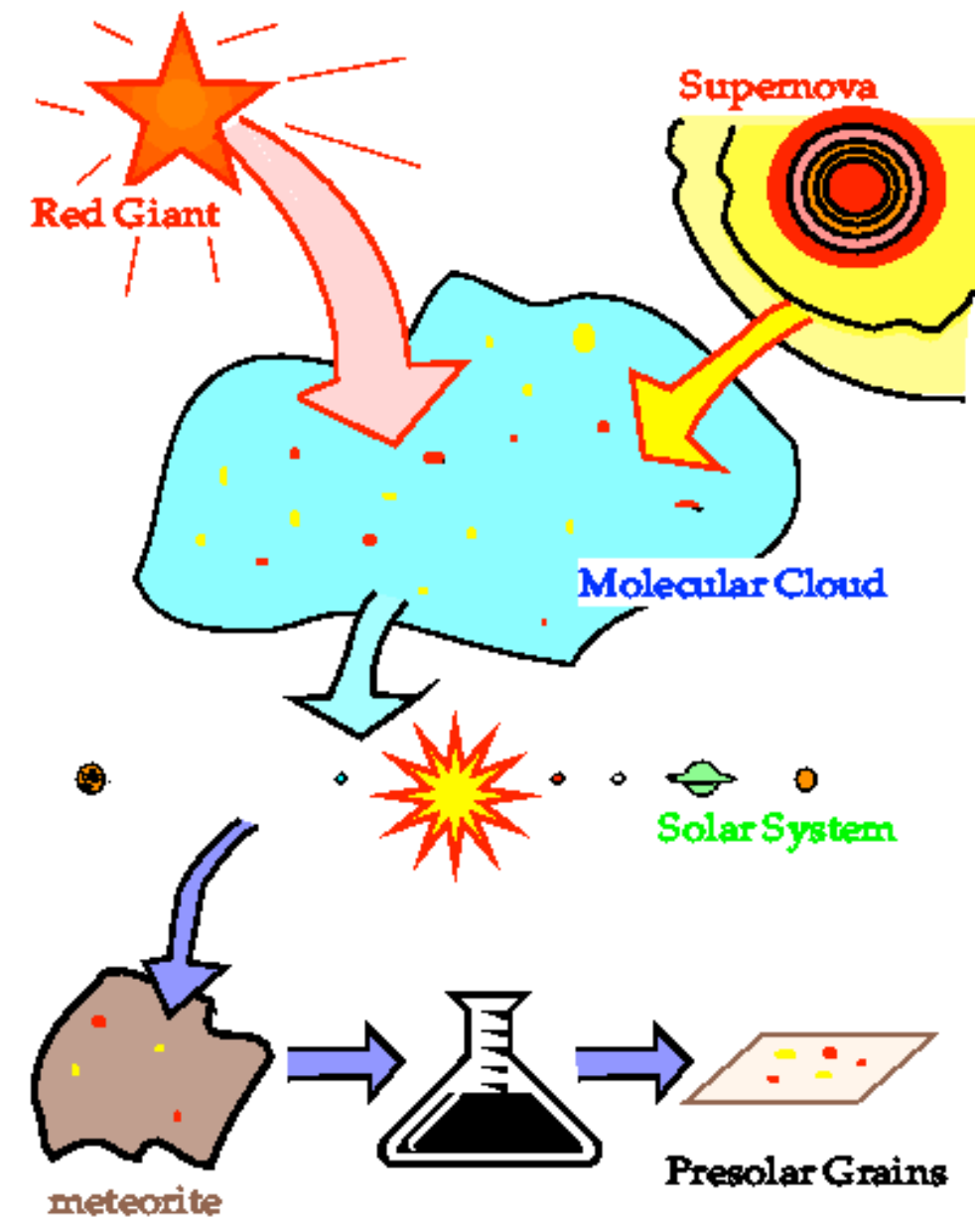
Galaxy formation:
A simulation of the baryon halo built up through accretion of 100 satellite galaxies (Bland-Hawthorn & Freeman, Science 287, 2000).

Introduction - pre-solar grains

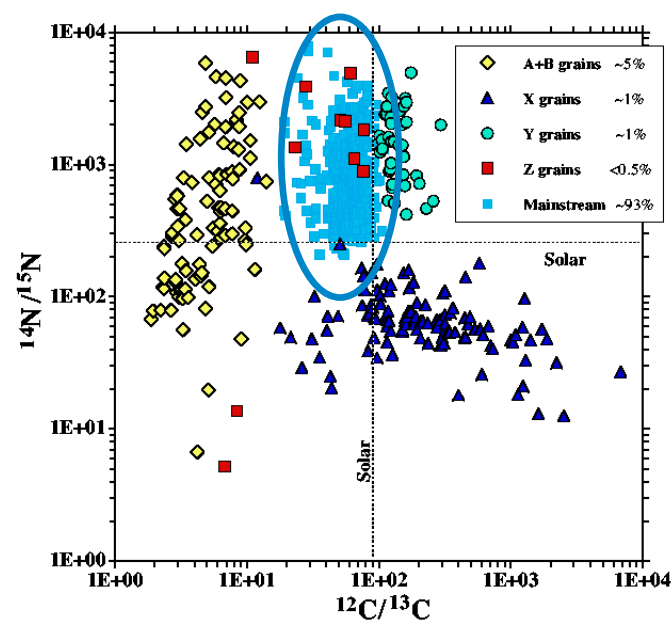
Presolar Grains



► the basic story line:



► isotopic data from pre-solar grains



Zinner E. Annu. Rev. Earth Planet. Sci. (1998)

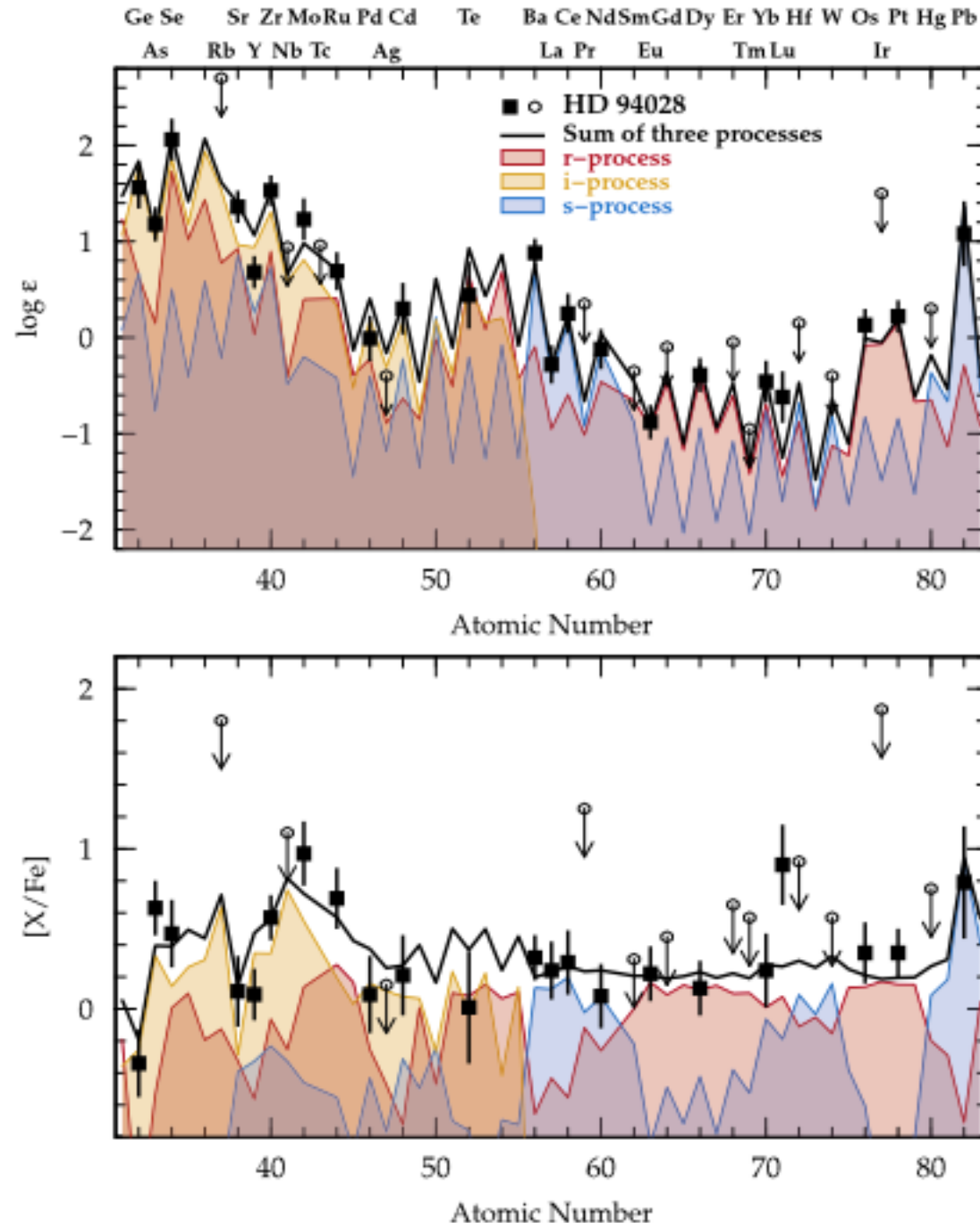
Introduction - Abundance distributions of stars

THE ASTROPHYSICAL JOURNAL, 821:37 (12pp), 2016 April 10
 © 2016. The American Astronomical Society. All rights reserved.

doi:10.3847/0004-637X/821/1/37



THE DIVERSE ORIGINS OF NEUTRON-CAPTURE ELEMENTS IN THE METAL-POOR STAR HD 94028: POSSIBLE DETECTION OF PRODUCTS OF *i*-PROCESS NUCLEOSYNTHESIS*



ABSTRACT

We present a detailed analysis of the composition and nucleosynthetic origins of the heavy elements in the metal-poor ($[\text{Fe}/\text{H}] = -1.62 \pm 0.09$) star HD 94028. Previous studies revealed that this star is mildly enhanced in elements produced by the slow neutron-capture process (*s* process; e.g., $[\text{Pb}/\text{Fe}] = +0.79 \pm 0.32$) and rapid neutron-capture process (*r* process; e.g., $[\text{Eu}/\text{Fe}] = +0.22 \pm 0.12$), including unusually large molybdenum ($[\text{Mo}/\text{Fe}] = +0.97 \pm 0.16$) and ruthenium ($[\text{Ru}/\text{Fe}] = +0.69 \pm 0.17$) enhancements. However, this star is not enhanced in carbon ($[\text{C}/\text{Fe}] = -0.06 \pm 0.19$). We analyze an archival near-ultraviolet spectrum of HD 94028, collected using the Space Telescope Imaging Spectrograph on board the *Hubble Space Telescope*, and other archival optical spectra collected from ground-based telescopes. We report abundances or upper limits derived from 64 species of 56 elements. We compare these observations with *s*-process yields from low-metallicity AGB evolution and nucleosynthesis models. No combination of *s*- and *r*-process patterns can adequately reproduce the observed abundances, including the super-solar $[\text{As}/\text{Ge}]$ ratio ($+0.99 \pm 0.23$) and the enhanced $[\text{Mo}/\text{Fe}]$ and $[\text{Ru}/\text{Fe}]$ ratios. We can fit these features when including an additional contribution from the intermediate neutron-capture process (*i* process), which perhaps operated through the ingestion of H in He-burning convective regions in massive stars, super-AGB stars, or low-mass AGB stars. Currently, only the *i* process appears capable of consistently producing the super-solar $[\text{As}/\text{Ge}]$ ratios and ratios among neighboring heavy elements found in HD 94028. Other metal-poor stars also show enhanced $[\text{As}/\text{Ge}]$ ratios, hinting that operation of the *i* process may have been common in the early Galaxy.

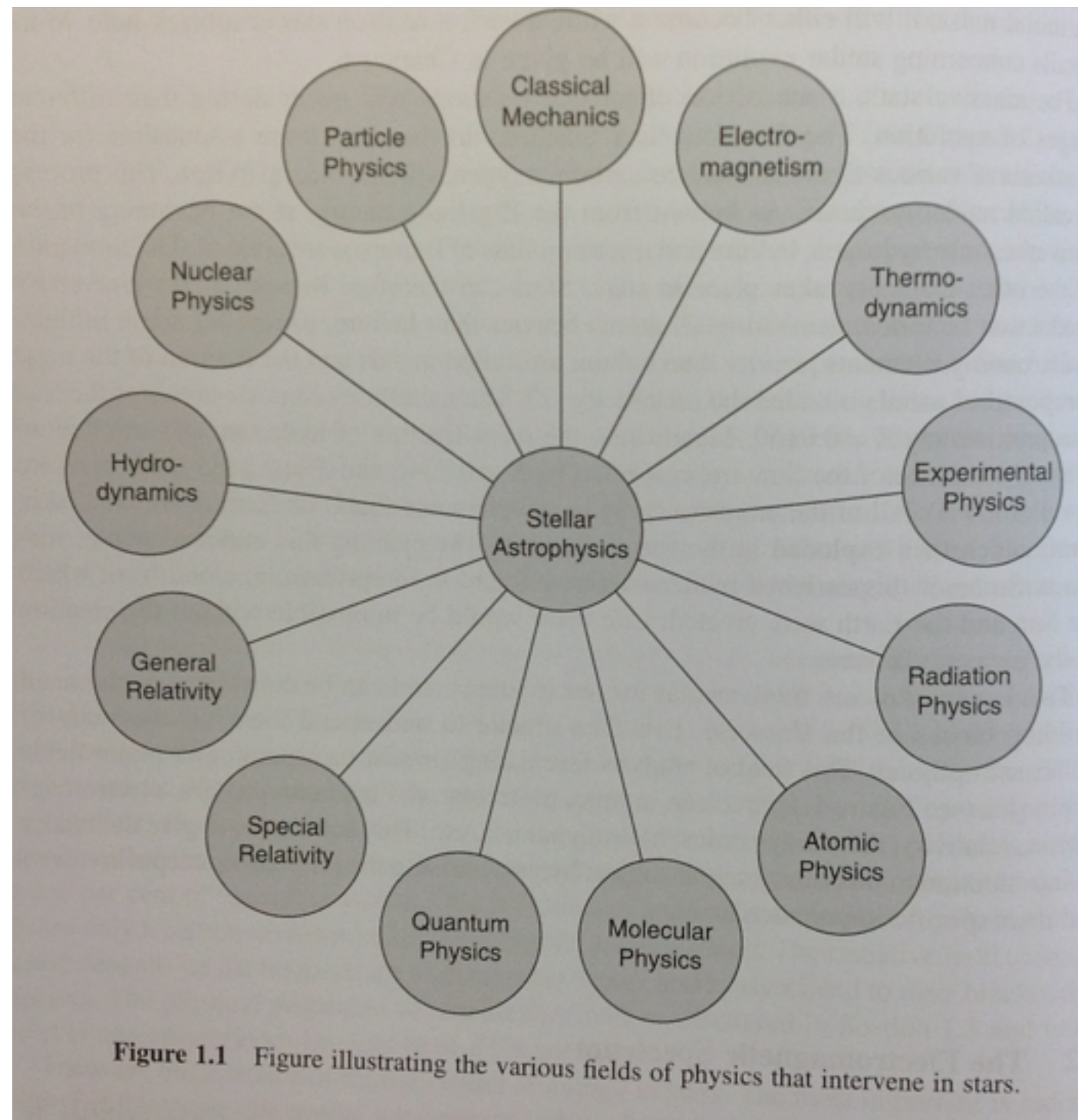
$$\begin{aligned} [\text{A}/\text{B}] &= \log A/\text{B}|_{\star} - \log A/\text{B}|_{\odot} \\ &= \log A_{\star}/A_{\odot} - \log B_{\star}/B_{\odot} \end{aligned}$$

Part I

Physics for stellar models

Stars: multi-physics systems

... that's what makes them so interesting!



CONTENTS

1. INTRODUCTION	2
2. MODULE DESIGN AND IMPLEMENTATION	3
3. NUMERICAL METHODS	3
4. MICROPHYSICS	4
4.1. Mathematical Constants, Physical and Astronomical Data	4
4.2. Equation of State	4
4.3. Opacities	6
4.4. Thermonuclear and Weak Reactions	8
4.5. Nuclear Reaction Networks	8
5. MACROPHYSICS	8
5.1. The Mixing Length Theory of Convection	8
5.2. Convective Overshoot Mixing	9
5.3. Atmosphere Boundary Conditions	10
5.4. Diffusion and Gravitational Settling	10
5.5. Testing MESA Modules in an Existing Stellar Evolution Code	11
6. STELLAR STRUCTURE AND EVOLUTION	11
6.1. Starting Models and Basic Input/Output	12
6.2. Structure and Composition Equations	13
6.3. Convergence to a Solution	14
6.4. Timestep Selection	14
6.5. Mesh Adjustment	14
6.6. Mass Loss and Accretion	15
6.7. Resolution Sensitivity	16
6.8. Multithreading	16
6.9. Visualization with PGstar	17
7. MESA star RESULTS: COMPARISONS AND CAPABILITIES	17
7.1. Low-mass Stellar Structure and Evolution	18
7.1.1. Low-mass Pre-main Sequence Stars, Contracting Brown Dwarfs and Giant Planets	18

7.1.2. Code Comparisons of $0.8 M_{\odot}$ and $1 M_{\odot}$ Models	20
7.1.3. The MESA star Solar Model	20
7.2. Intermediate-mass Structure and Evolution	20
7.2.1. Comparison of EVOL and MESA star	21
7.2.2. Interior Structure of Slowly Pulsating B Stars and Beta Cepheids	22
7.3. High Mass Stellar Structure and Evolution	23
7.3.1. $25 M_{\odot}$ Model Comparisons	23
7.3.2. Comparison of 15, 20, and $25 M_{\odot}$ Models	24
7.3.3. $1000 M_{\odot}$ Metal-free Star Capabilities	25
7.4. Stellar Evolution with Mass Transfer	25
7.4.1. Mass Transfer in a Binary	26
7.4.2. Rapid Helium Accretion onto a Neutron Star	26
8. SUMMARY AND CONCLUSION	27
APPENDIX A. MANIFESTO	28
A.1. Motivation for a New Tool	28
A.2. MESA Philosophy	28
A.3. Establishment of the MESA Council	29
APPENDIX B. CODE TESTING AND VERIFICATION	29

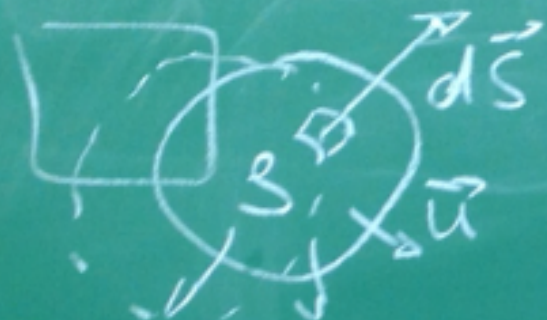
This MESA code paper is recommended reading as an example for how all this physics is implemented in a simulation code

► classification of fluid dynamics regimes

Equations of hydrodynamics treat the fluid as a continuous medium with well-defined macroscopic properties (e.g. pressure or density) at each point.

Distinguish fluids:

- incompressible (e.g. liquids) or compressible (e.g. gases). Very slow flow (subsonic) gases behave incompressible.
- viscous (low Re) vs. inviscid (high Re) flows (Reynolds number: ratio between inertial and viscous forces)
- laminar (low Re) vs. turbulent (high Re)
- steady flow: all $\partial/\partial t = 0$
- Subsonic ($Ma < 1$) vs transonic, supersonic (Mach number: v/c_s)

Conservation lawsfluid element

$$\frac{\partial}{\partial t} \int_V S dV$$

$$-\int_S S \vec{u} \cdot d\vec{s} = \int_V \nabla \cdot S \vec{u} dV$$

$$= \int_V \frac{\partial S}{\partial t} dV$$

→ continuity equation.

Fluids

► conservation laws

general structure of the conservation laws

$$\frac{\partial}{\partial t} (\text{density of quantity}) + \nabla (\text{flux of quantity}) = \text{Sources and sinks of quantity}$$

Mass conservation:

$$\frac{\partial \rho}{\partial t} + \nabla \cdot (\rho \mathbf{u}) = 0 \quad (1)$$

Momentum equation:

- consider forces between fluid elements
- pressure between fluid elements: momentum flux associated with random isotropic motions
- force from gravity: local acceleration \mathbf{g}

$$\rho \frac{\partial \mathbf{u}}{\partial t} + \rho (\mathbf{u} \cdot \nabla) \mathbf{u} = -\nabla p + \rho \mathbf{g} \quad (2)$$

What \mathbf{g} for momentum equation in astrophysical applications? Calculate gravitational field from density distribution.

Fluids - gravity

► gravity

Gravitational acceleration given by **gravitational potential** Ψ :

$$\mathbf{g} = -\nabla\Psi$$

Poisson equation for the gravitational potential Ψ :

$$\nabla^2\Psi = 4\pi G\rho$$

where G is the gravitational constant and ρ is the mass density.

Spherical symmetry:

$$\Psi = \frac{Gm}{r}$$

For suitable symmetry Eq. (10) allows to calculate the gravitational field vector \mathbf{g} directly through identifying *Gaussian surfaces*. As in electrostatics, use integral form of Eq. (10), which can be obtained via Gauss's theorem.

With the mass and momentum equations in place we need expressions for Ψ and p in terms of ρ and \mathbf{u} :

- Ψ from Poisson equation Eq. (11).
- P from equation of state, consider three cases:
 - (a) ideal gas equation of state
 - (b) barotropic equation of state: pressure p depends only on ρ , as for example
 - isothermal: $p \sim \rho$
 - adiabatic: $p = K\rho^\gamma$
 - non-ideal effects are important, e.g. electron degeneracy or radiation pressure

$$P = \frac{R}{\mu} \rho T$$

Fluid instabilities

Sound speed

$$c_s^2 = (\partial p / \partial \rho)_s$$

Mach number

$$Ma = \frac{v}{c_s}$$

CFL condition

$$\Delta t < \frac{\Delta x Ma}{v}$$

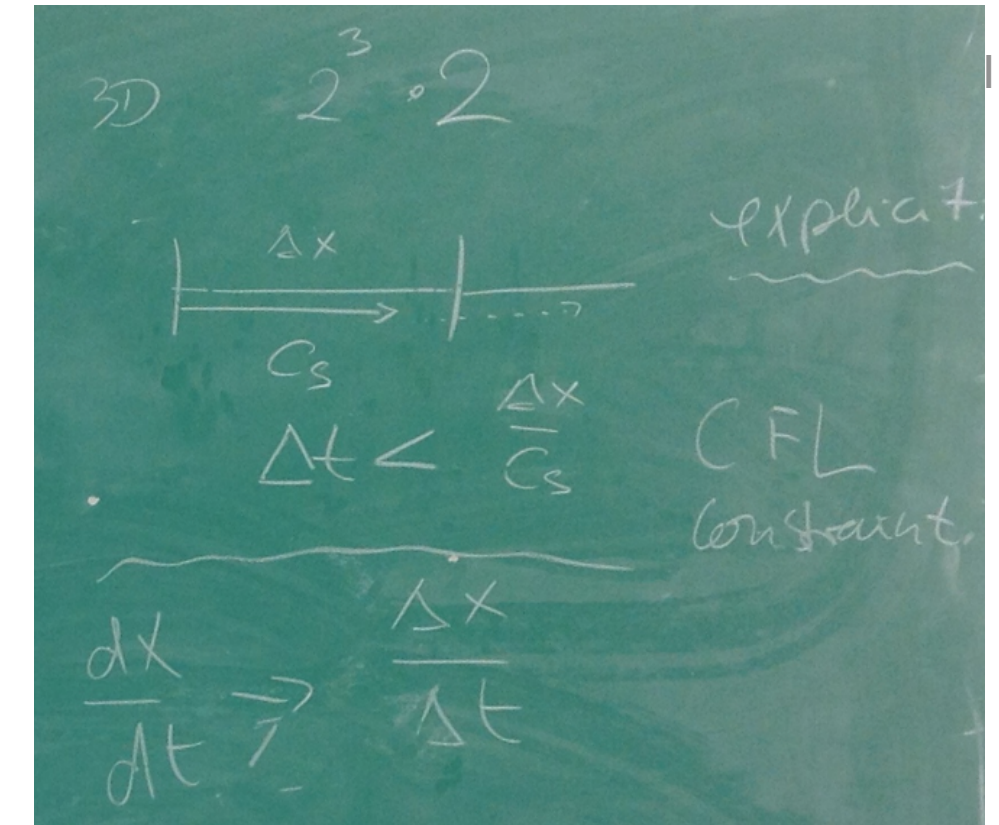
Rayleigh-Taylor instability

Unstable stratification of fluid layers overturns under the influence of gravity. This instability can be observed in two important cases:

- Convective instability: the stability of a fluid element that has some heat excess and rises adiabatically [†24]
- Stratified fluids, in particular, a heavier fluid on top of a lighter fluid [movie]

Kelvin-Helmholtz instability

Instability induced by gradient in horizontal velocity, or shear flows.



movies

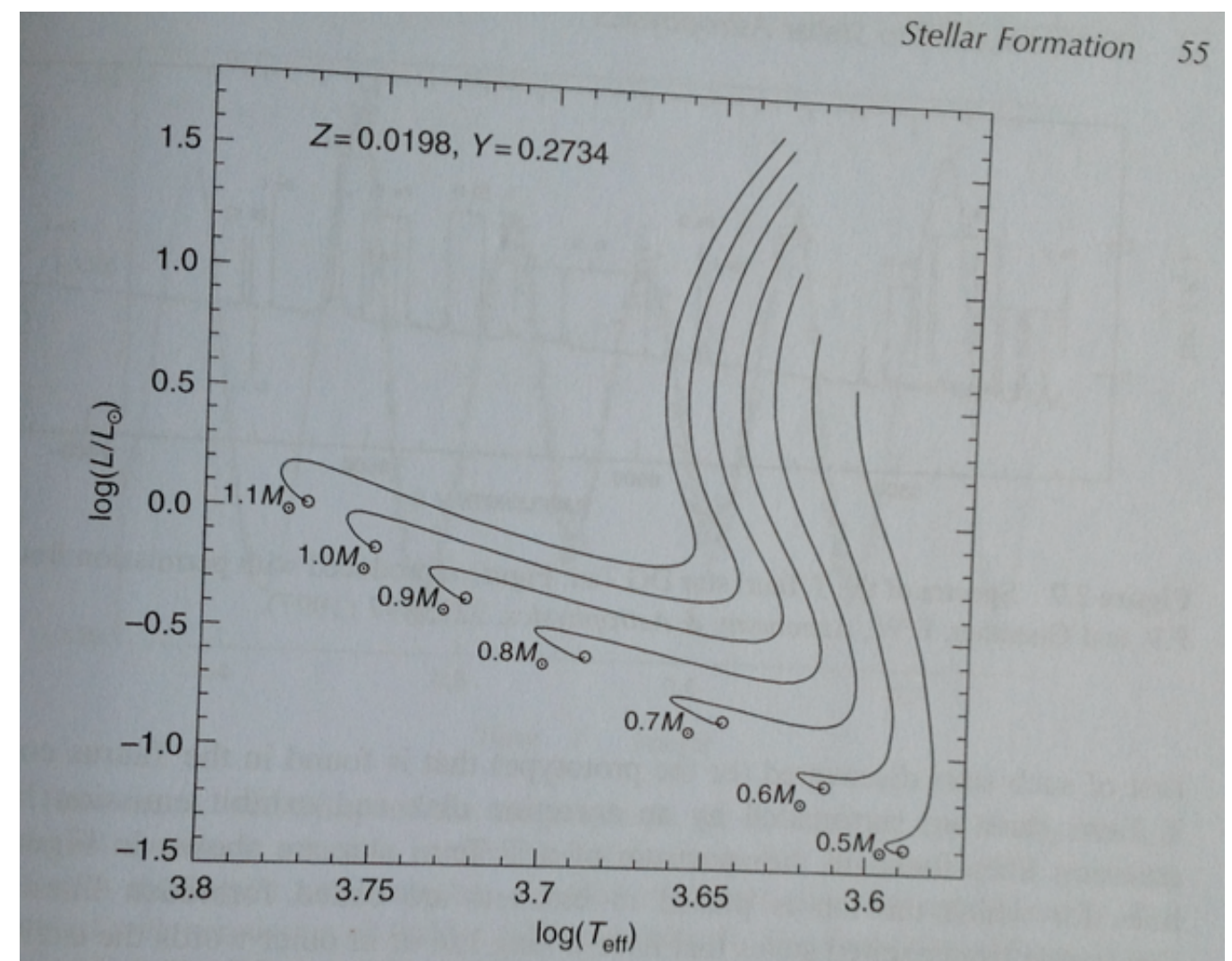
20

Time scales

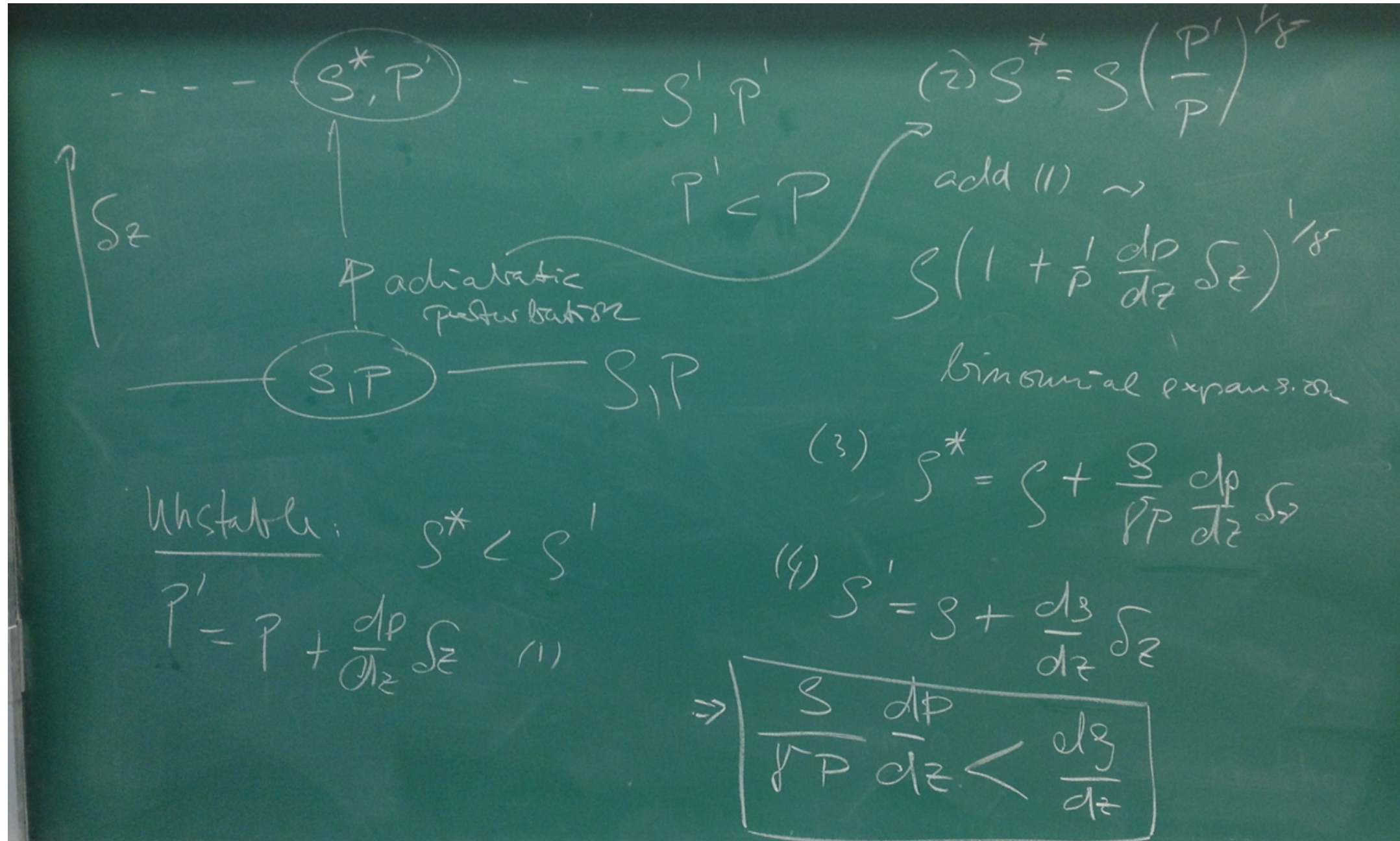
► Timescales

- the free-fall timescale t_{ff} : star reacts on this time scale if you switch off the pressure support from the EOS
- the Kelvin-Helmholtz or thermal timescale $t_{\text{KH}} = t_{\text{th}}$: star reacts on this time scale if you switch off the source of energy (nuclear burning)
- for completeness: the nuclear timescale t_{nuc} : the star consumes its nuclear fuel, e.g. H during main-sequence burning, on this time scale

► Pre-main sequence evolution - an example for stellar evolution on the thermal time scale



Stability of a stratified fluid - energy transport by convection



- ▶ T gradient of an adiabatically stratified layer
- ▶ T gradient that a layer will have with effective transport of energy by convection

$$\frac{\partial T}{\partial r} \Big|_{ad} = \left(1 - \frac{1}{\gamma} \right) \frac{T dP}{P dr}$$

Radiative transport of energy

- depends on mean free path
 - interior:
 - ▶ ℓ_{ph} small \rightarrow diffusion of photons transports energy [\rightarrow radiative temperature gradient]
- $$\frac{\partial T}{\partial r} \Big|_{\text{rad}} = -\frac{3}{16\pi acr^2} \frac{\kappa \rho L}{T^3}$$

- ▶ if L large \rightarrow photons may contribute to total pressure: $P = P_{\text{gas}} + P_{\text{rad}}$
- surface:
 - ▶ ℓ_{ph} large \rightarrow diffusion approximation not valid anymore, needs detailed radiation transport considering in detail the interaction of radiation and matter, requires atomic physics.
- ▶ Schwarzschild condition for instability against convection

$$\left| \frac{\partial T}{\partial r} \right|_{\text{rad}} > \left| \frac{\partial T}{\partial r} \right|_{\text{conv}}$$

[The gradient are often written in terms of $\nabla \equiv \frac{\partial \ln T}{\partial \ln P}$. Rewrite the above as ∇_{ad} and ∇_{rad} .] That way you deal with the negative sign of dT/dr .

The opacity mountain and its consequence for the convective structure of stars as a function of mass:

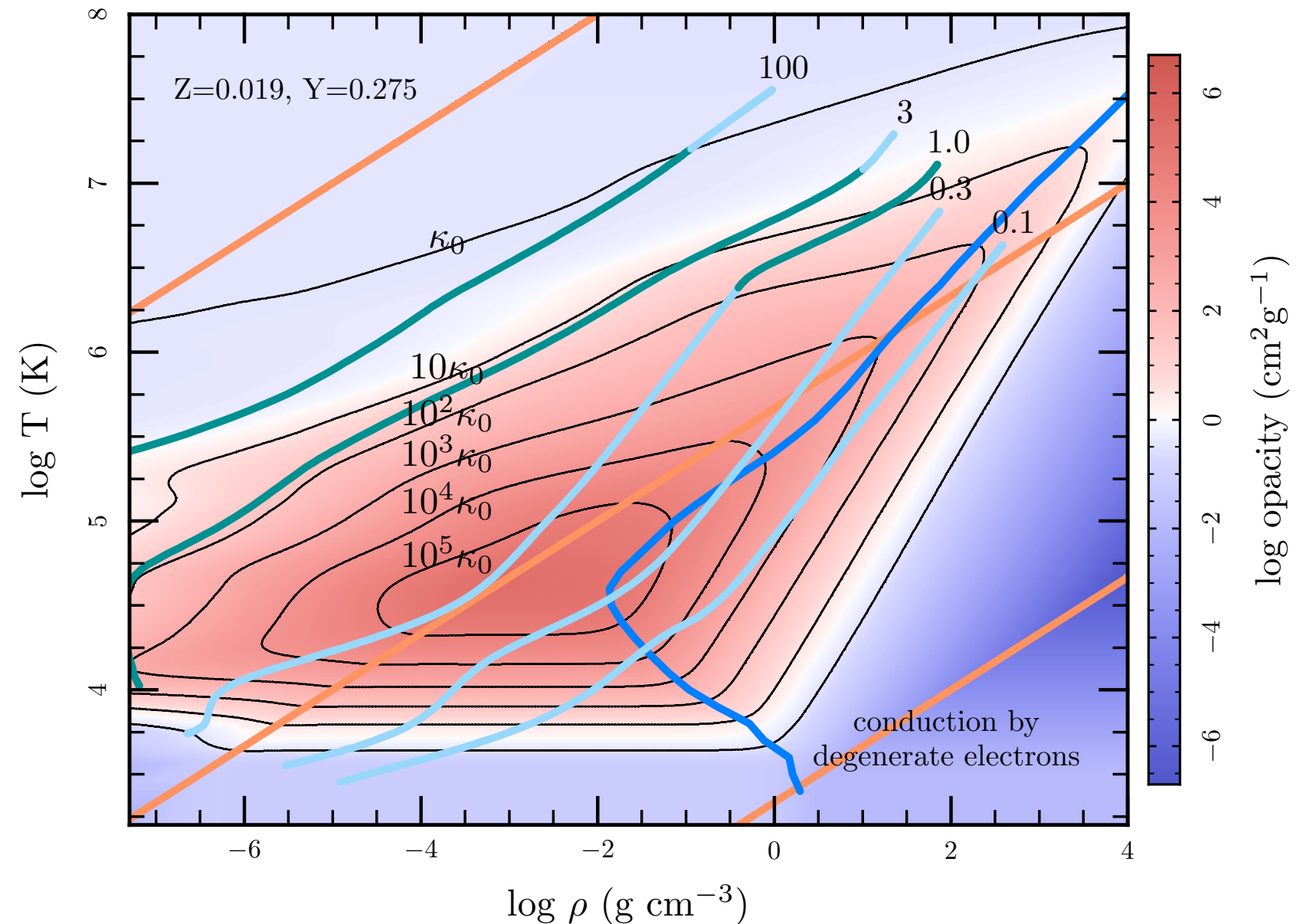
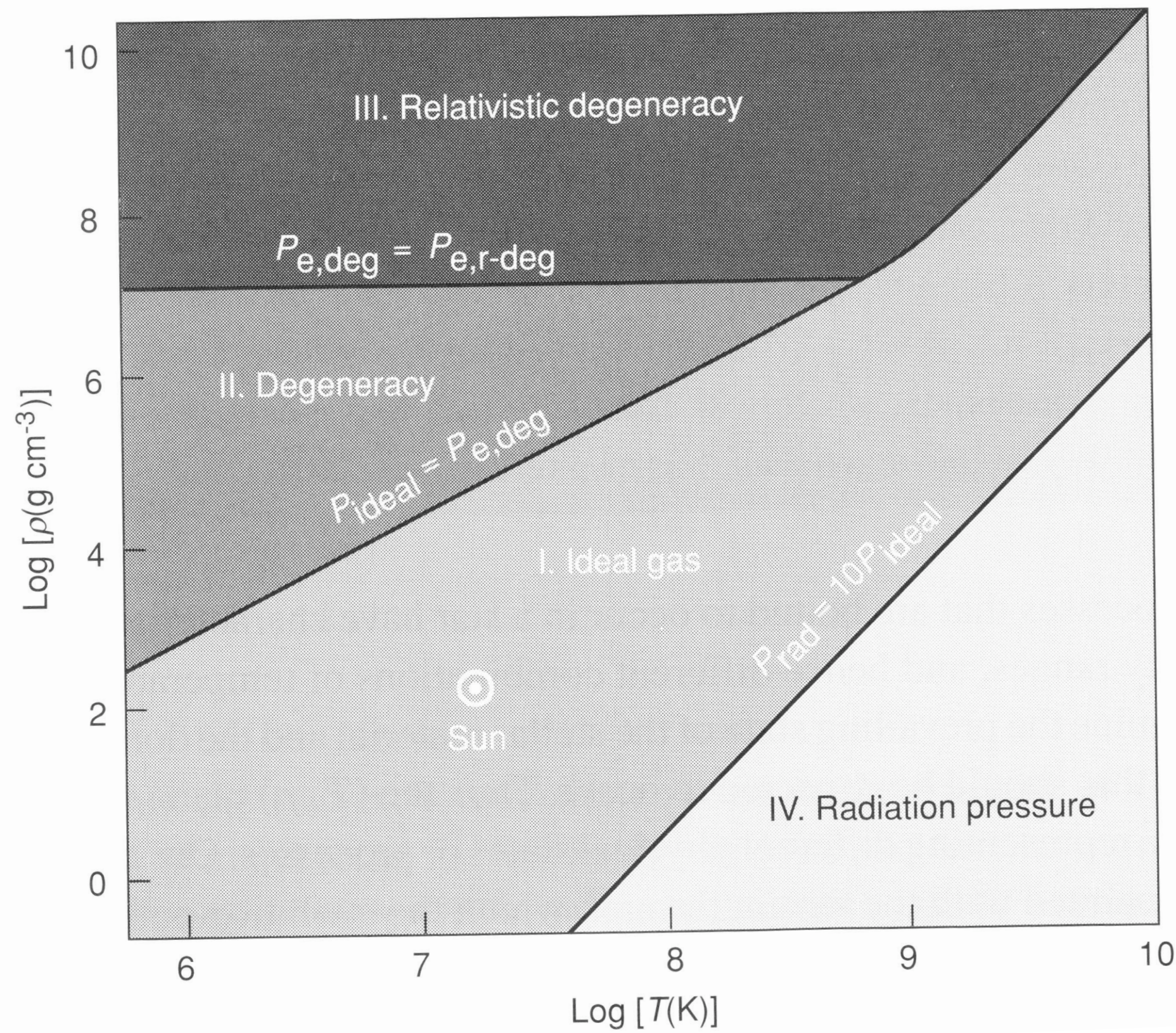


Fig. 3.— The resulting MESA opacities for $Z = 0.019, Y = 0.275$. The underlying shades show the value of κ , whereas the contours are in units of the electron scattering opacity, $\kappa_0 = 0.2(1 + X) \text{ cm}^2 \text{ g}^{-1}$. The orange lines show (top to bottom) where $\log R = -8$, $\log R = 1$ and $\log R = 8$. Stellar interior profiles for main sequence stars of mass $M = 0.1, 0.3, 1.0, 3.0 \& 100M_\odot$ are shown by the green(radiative regions)-light blue(convective regions) lines. Electron conduction dominates the opacity to the right of the dark blue line (which is where the radiative opacity equals the conductive opacity).

Different EOS regimes in the rho-T plane

25



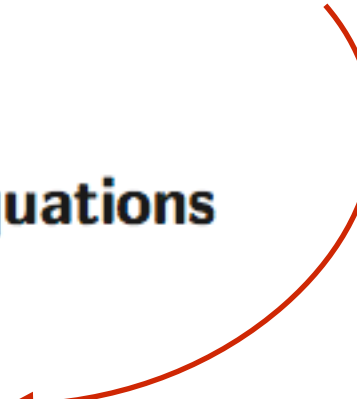
$$\rho \frac{\partial \mathbf{u}}{\partial t} + \rho (\mathbf{u} \cdot \nabla) \mathbf{u} = -\nabla p + \rho \mathbf{g}$$

Stellar structure equations

$$\frac{dP}{dr} = -\frac{GM_r}{r^2}\rho$$

$$\frac{dM_r}{dr} = 4\pi r^2 \rho$$

$$\frac{dL_r}{dr} = 4\pi r^2 \epsilon \rho$$



Material functions

- radiative absorption coefficient, opacity: $\kappa(P, T, \mathbf{X})$
- equation of state, density: $\rho(P, T, \mathbf{X})$
- rate of energy production: $\epsilon(P, T, \mathbf{X})$

Composition change

mixing:

$$\left. \frac{dX_i}{dt} \right|_{\text{mix}} = \frac{\partial}{\partial m} \left[(4\pi r^2 \rho) D \frac{dX_i}{dm} \right]$$

burning:

$$\left. \frac{d\mathbf{X}_j}{dt} \right|_{\text{burn}} = \hat{F}_j \cdot \mathbf{X}_j$$

Temperature gradients:

- radiative:

$$\left. \frac{\partial T}{\partial r} \right|_{\text{rad}} = -\frac{3}{16\pi acr^2} \frac{\kappa \rho L}{T^3}$$

- convective:

$$\left. \frac{\partial T}{\partial r} \right|_{\text{ad}} = \left(1 - \frac{1}{\gamma} \right) \frac{T}{P} \frac{dP}{dr}$$

Nuclear network and nucleosynthesis

the energy generation ϵ_{nuc} from nuclear reactions needs to be taken into account, and these are simultaneously responsible for composition changes:

$$\frac{d\mathbf{X}_j}{dt} \Big|_{\text{burn}} = \hat{F}_j \cdot \mathbf{X}_j \quad (8.4)$$

where \mathbf{X}_j is a vector containing the mass fractions of all species in zone j and the operator \hat{F}_j represents all reactions through which these species can interact. Instead of in terms of mass fraction X , the network equations are rather written in terms of the number density N_m of species m by collecting all production and destruction terms of reactions of the type $k + l \rightarrow m + n$:

$$\frac{dN_m}{dt} = N_k N_l \langle \sigma v \rangle_{kl,m} - N_m N_n \langle \sigma v \rangle_{mn,o} + \dots + N_i \lambda_{i,m} - N_j \lambda_{m,j} \quad (8.5)$$

where $\langle \sigma v \rangle$ is the product of the cross section and the relative velocity in the center-of-mass system averaged over the appropriate distribution function and λ is the rate for β decays. Reaction rates can be obtained, for example, from (Angulo et al. 1999, http://pntpmp.ulb.ac.be/Nacre/nacre_d.htm). The number density is expressed in terms of a number fraction or mole fraction $Y = X/A$, with A the atomic mass number, by $N = Y \rho N_A$ where $N_A = 1/M_u$ is the Avogadro number and M_u is the atomic mass number. For each reaction, an amount of energy Q is released, which is partly in the form of neutrinos and therefore lost. The energy released from ΔN reactions is therefore $\epsilon_{\text{nuc}} = \Delta N Q = \Delta Y \rho N_A Q$.

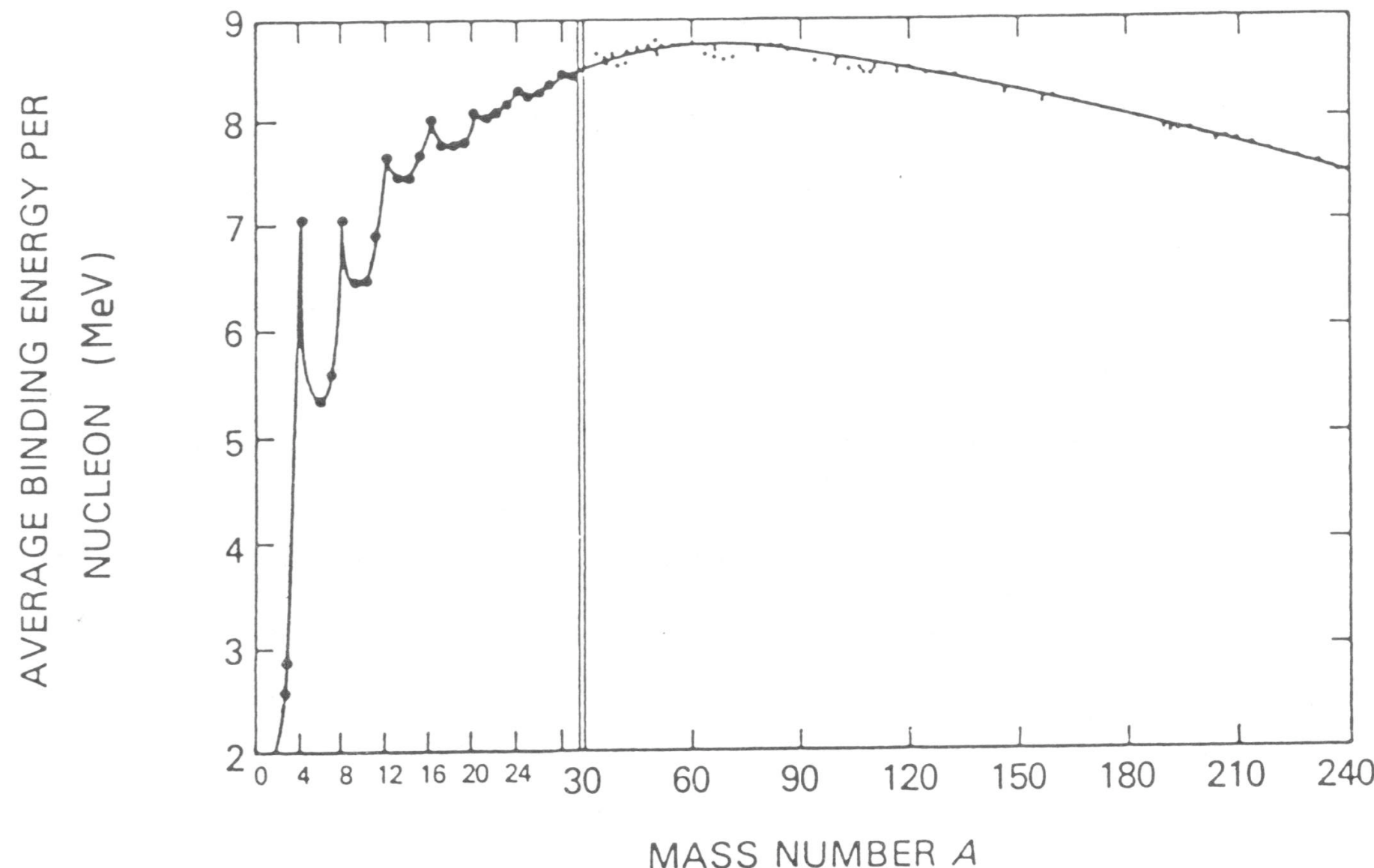


FIGURE 3.1. Binding energy per nucleon shown as a function of atomic mass number A . The highest nuclear binding energy (stability) is found for elements near iron.

From Rolfs & Rodney: Cauldrons in the Cosmos

Nuclear network and nucleosynthesis

29

Reaction rates

- ▶ particles follow Boltzmann distribution
 - ▶ $\sigma(E)$ energy-dependent reaction rate cross section

$$\langle \sigma v \rangle = \left(\frac{8}{\pi \mu} \right)^{1/2} \frac{1}{(kT)^{3/2}} \int_0^\infty \sigma(E) \cdot E \cdot \exp \left(-\frac{E}{kT} \right) dE,$$

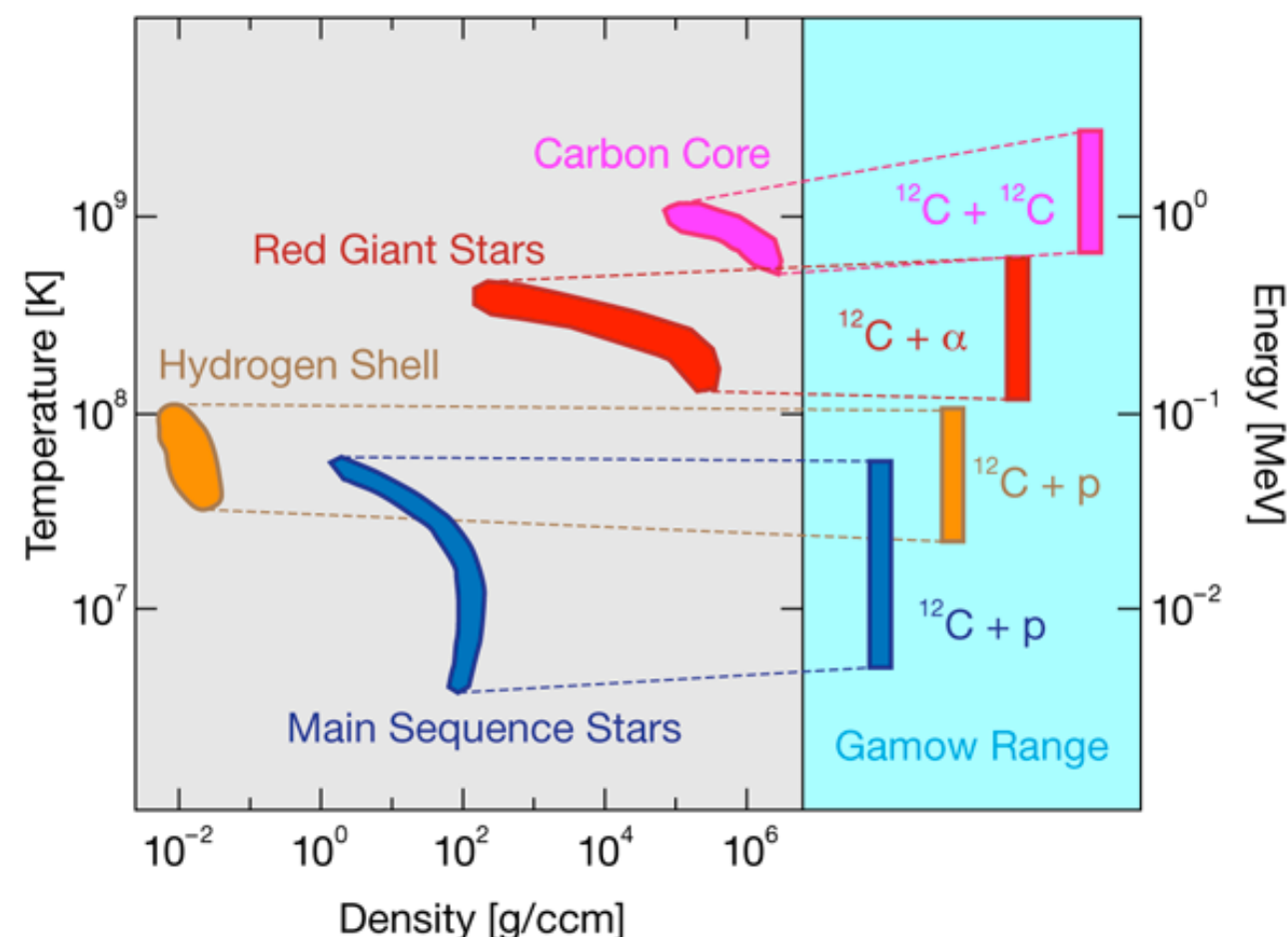
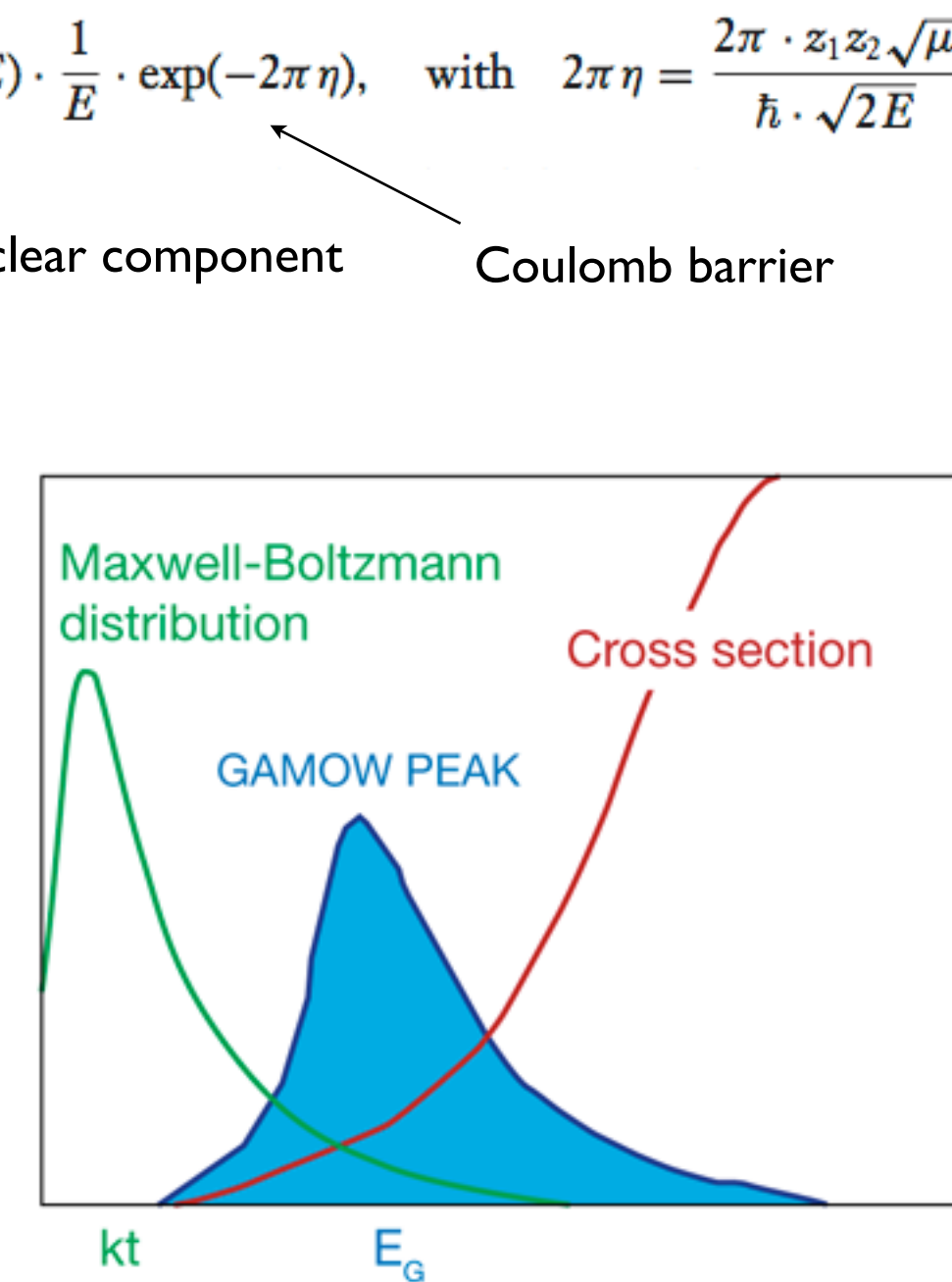


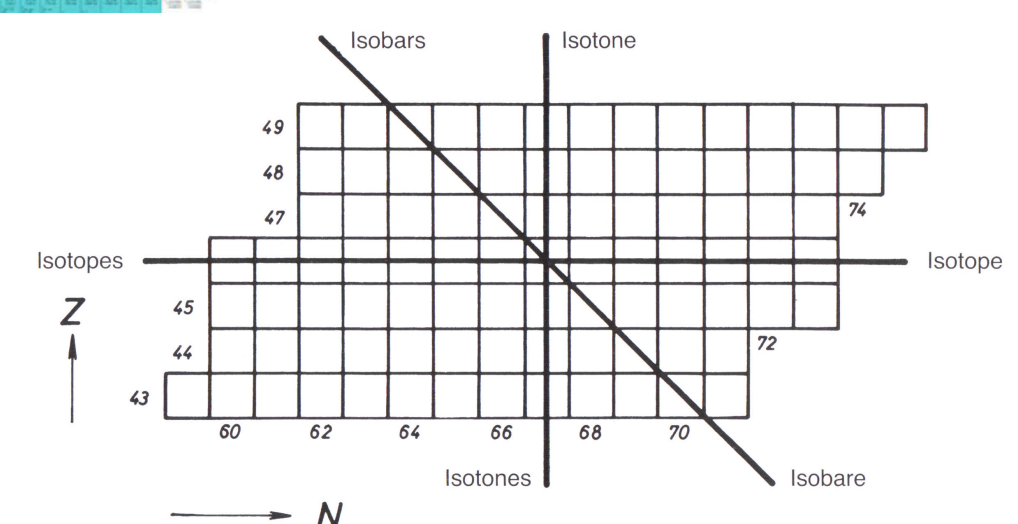
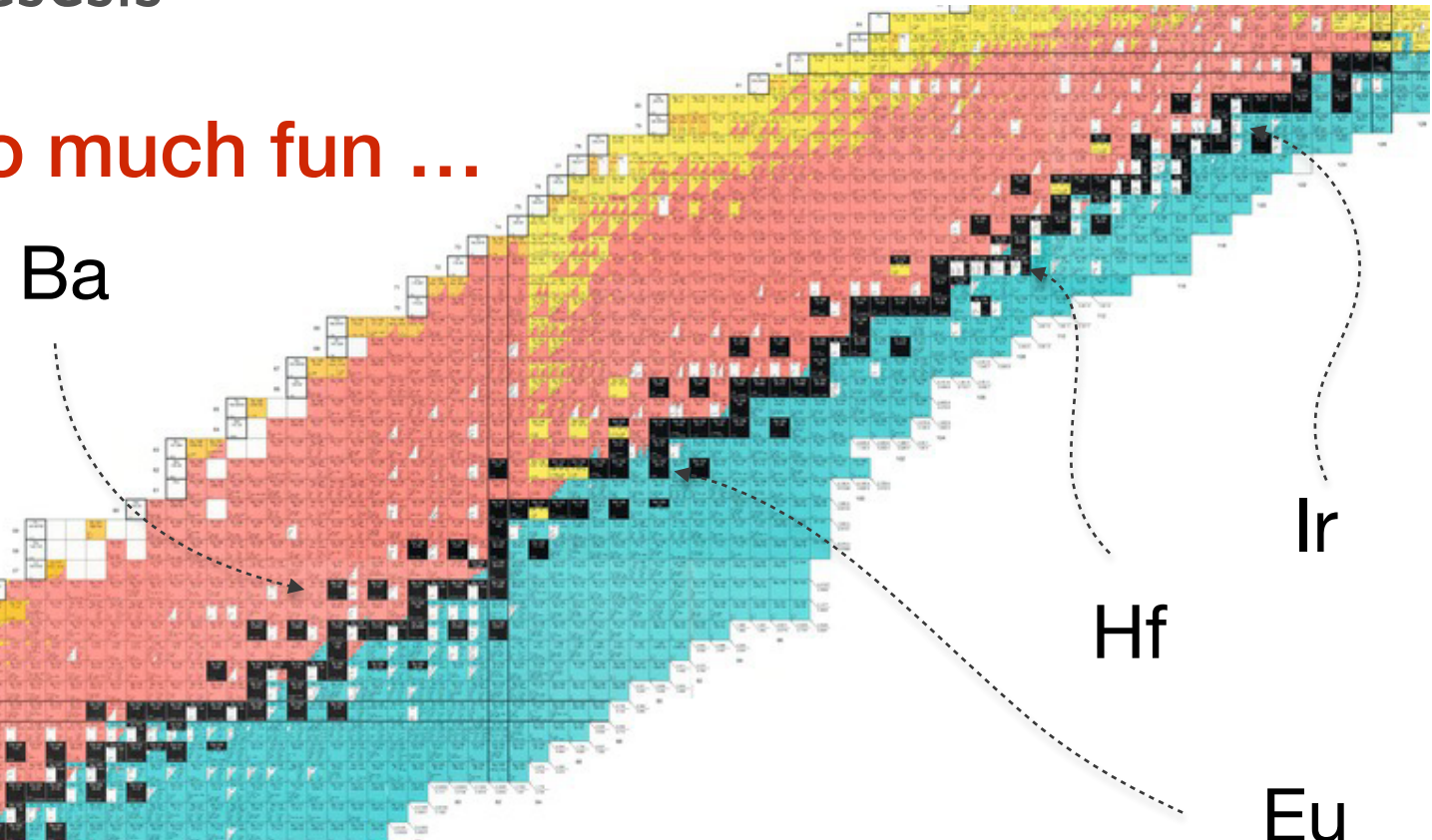
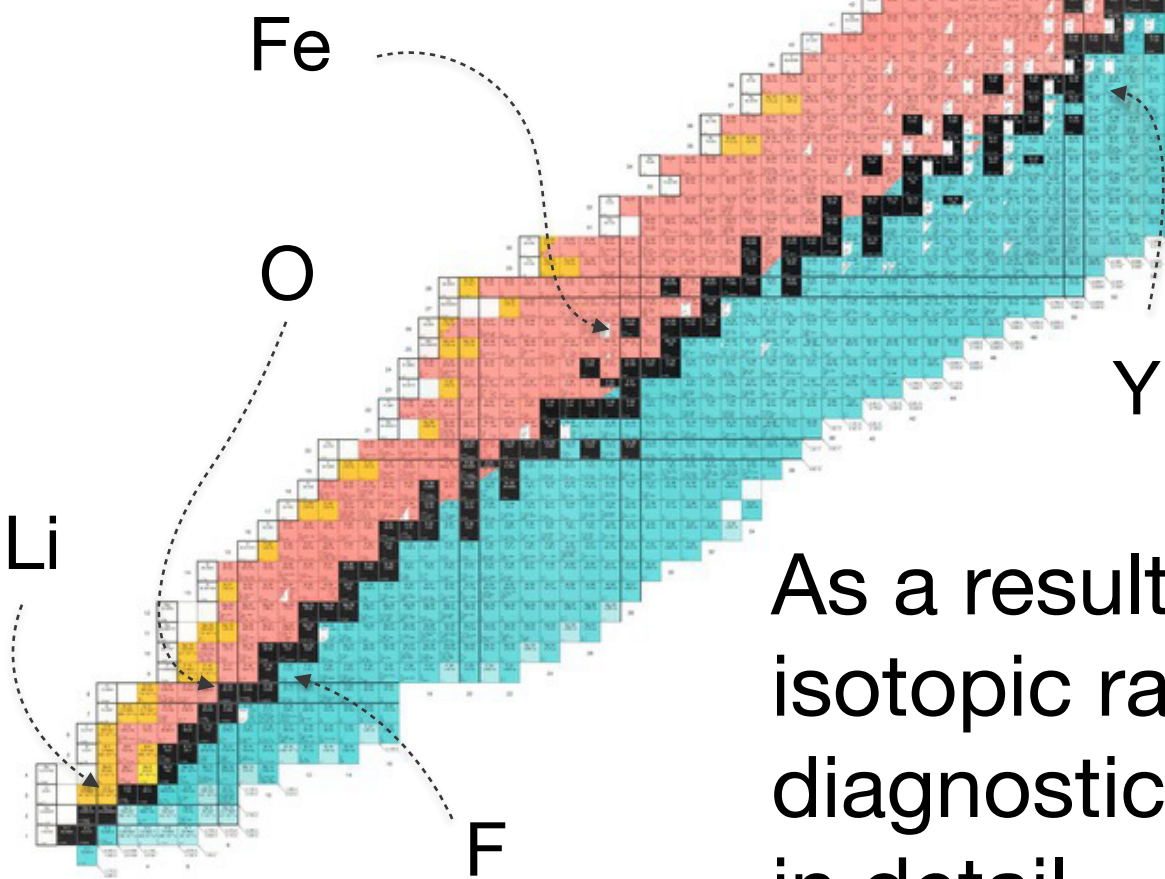
Figure 3: The Gamow window is the range of energies where nuclear reactions occur in stars. (Top) The window is shown as the overlap region between the Maxwell Boltzmann distribution of the interacting particles and the low-energy tail of the reaction cross section. (Bottom) Typical temperature-density regimes for a variety of core and shell burning stages during stellar evolution in correlation with the Gamow energy ranges for carbon-induced reactions at these conditions.



Nuclear network and nucleosynthesis

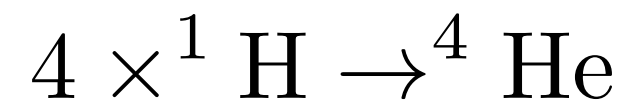
So many different elements ... so much fun ...

Abundances are the result
of the details of the
thermodynamic and
mixing evolution of the
progenitor evolution

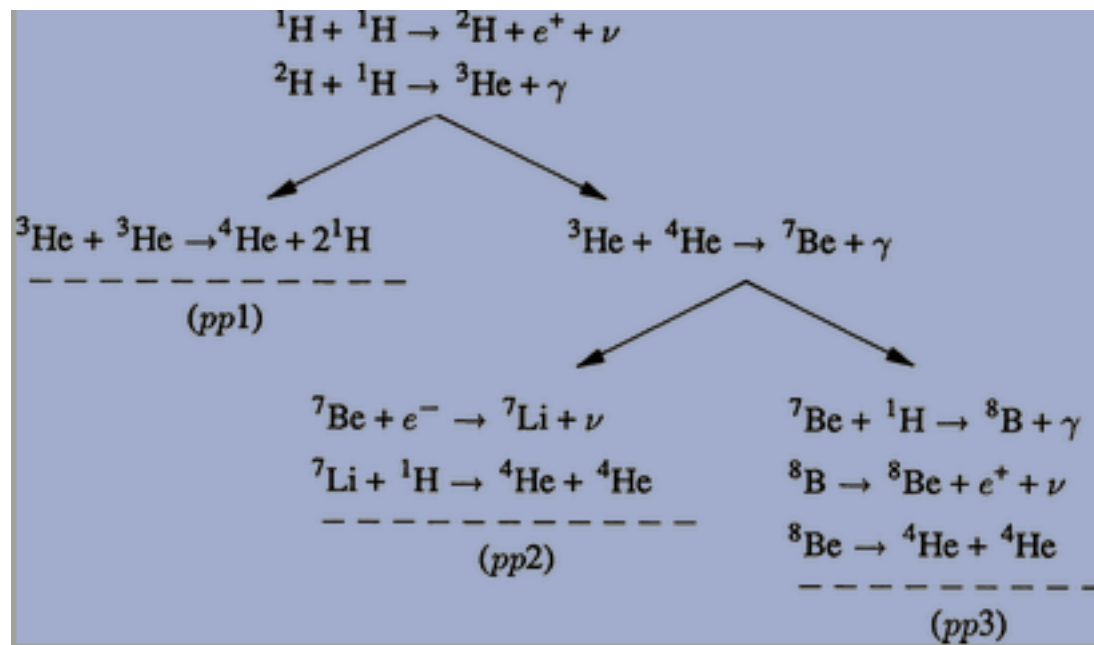


As a result elemental abundances and especially isotopic ratios are an enormously powerful diagnostic tool for understanding how stars work in detail.

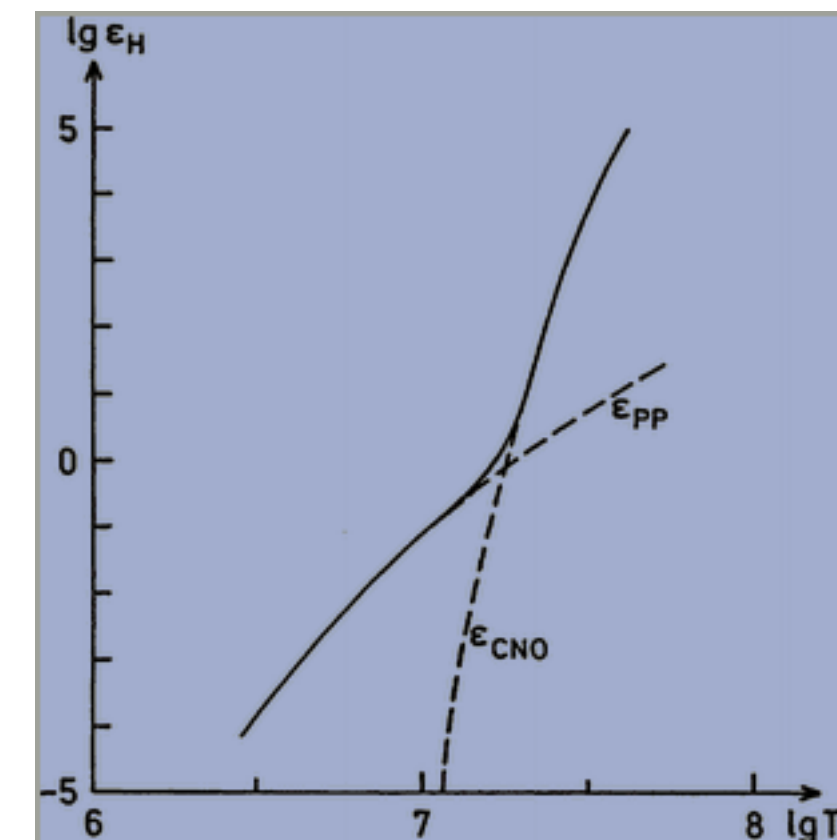
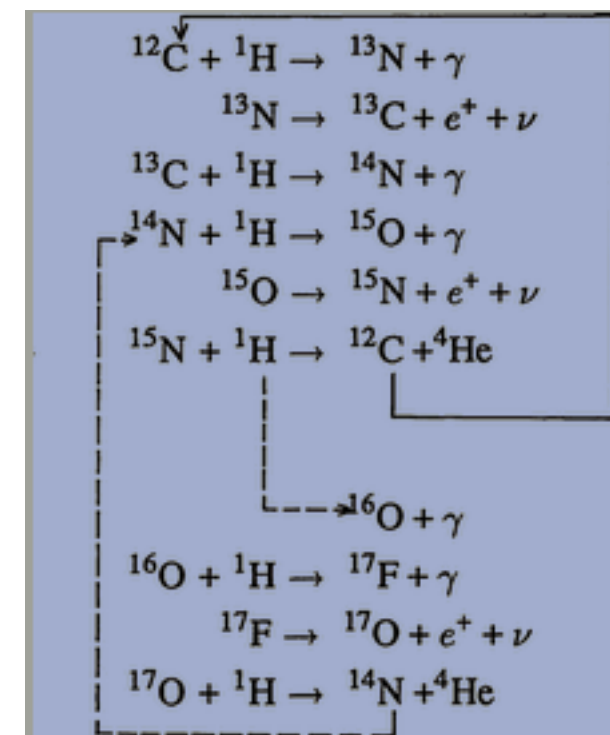
H burning



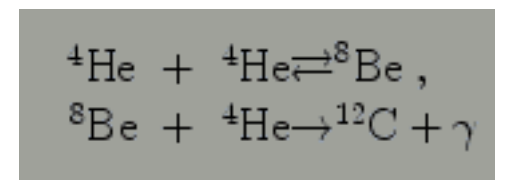
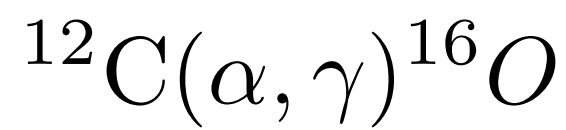
PP chain



CNO cycle

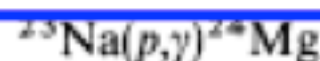
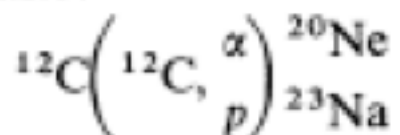


H burning

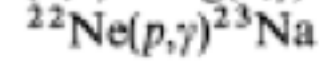
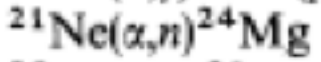
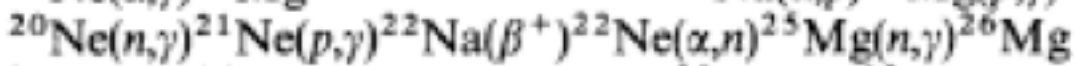
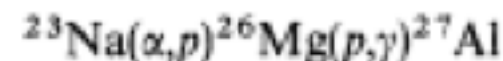
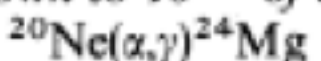


IMPORTANT REACTIONS IN CARBON BURNING

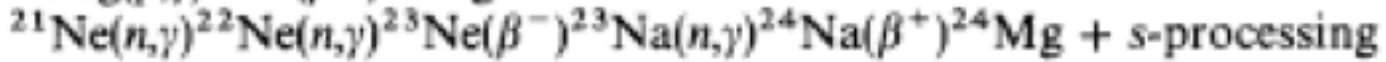
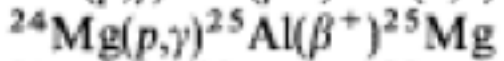
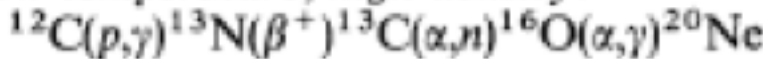
Basic:



Down to 10^{-2} of above:

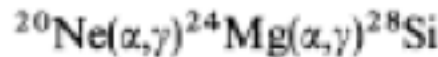


Low-temperature, high-density:

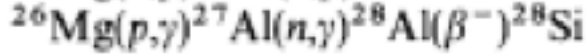
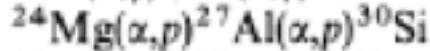
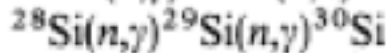
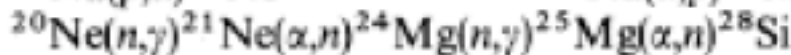
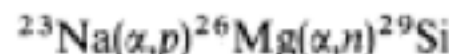


NEON BURNING

Basic reactions:



Flows $> 10^{-2}$ times the above:



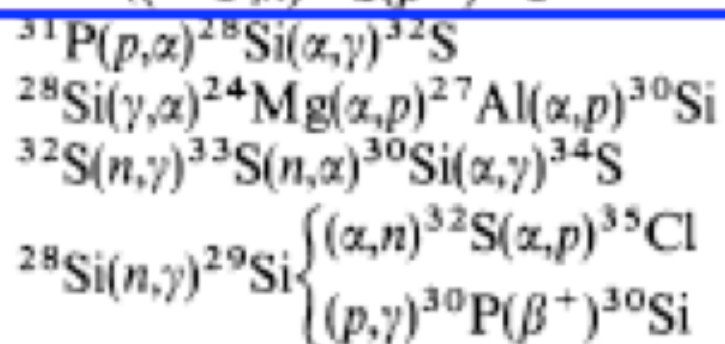
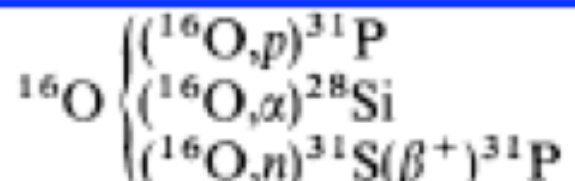
At low temperature and high density

(^{22}Ne left from prior n -rich C burning):

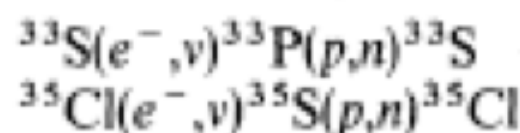


OXYGEN BURNING

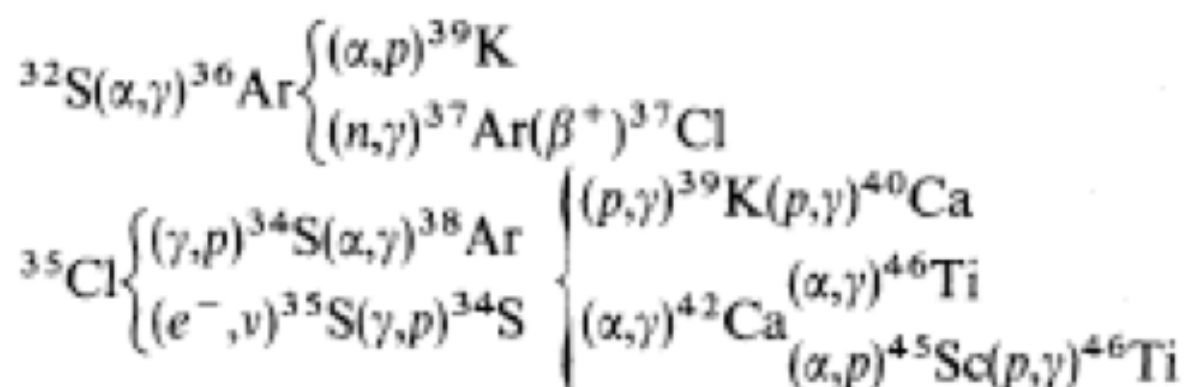
Basic reactions:



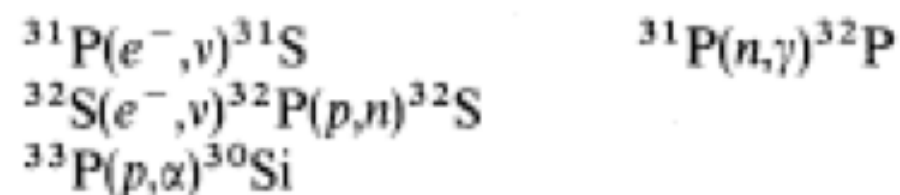
Electron captures:



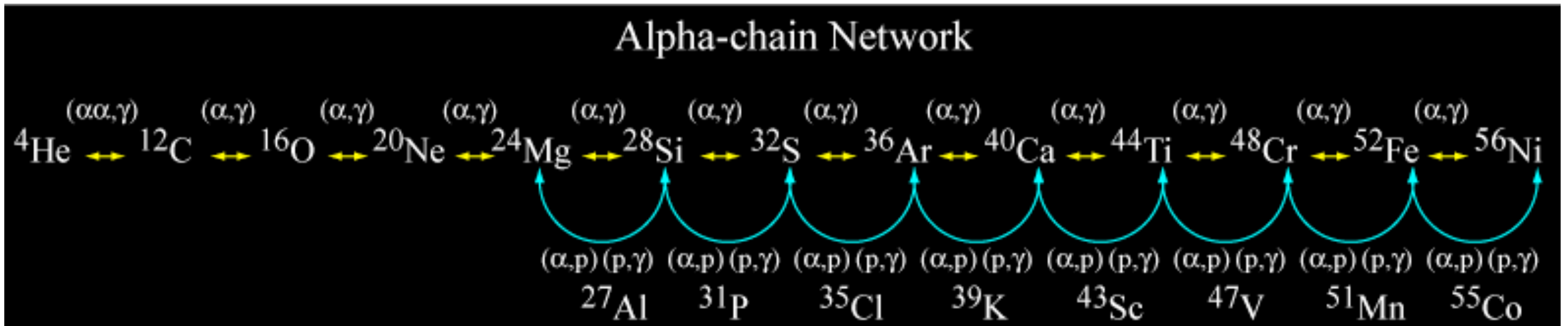
Massive stars ($M_x = 16 M_\odot$):



Lower mass stars ($M_x = 4 M_\odot$):



Silicon burning



cococubed.asu.edu

Equilibrium: Forward and reverse rates are (almost!) in balance and much faster than hydrodynamic/evolution timescale

Quasi-statistical equilibrium (QSE): Several groups
of nuclei in equilibrium

Nuclear-statistical equilibrium (NSE): All nuclei in
equilibrium

Silicon burning

Supernovae

Core becomes increasingly “neutronized”

$$M_{Ch} \sim Y_e^2$$

Part II

Stellar models

Outcome of stellar evolution as a function of initial mass

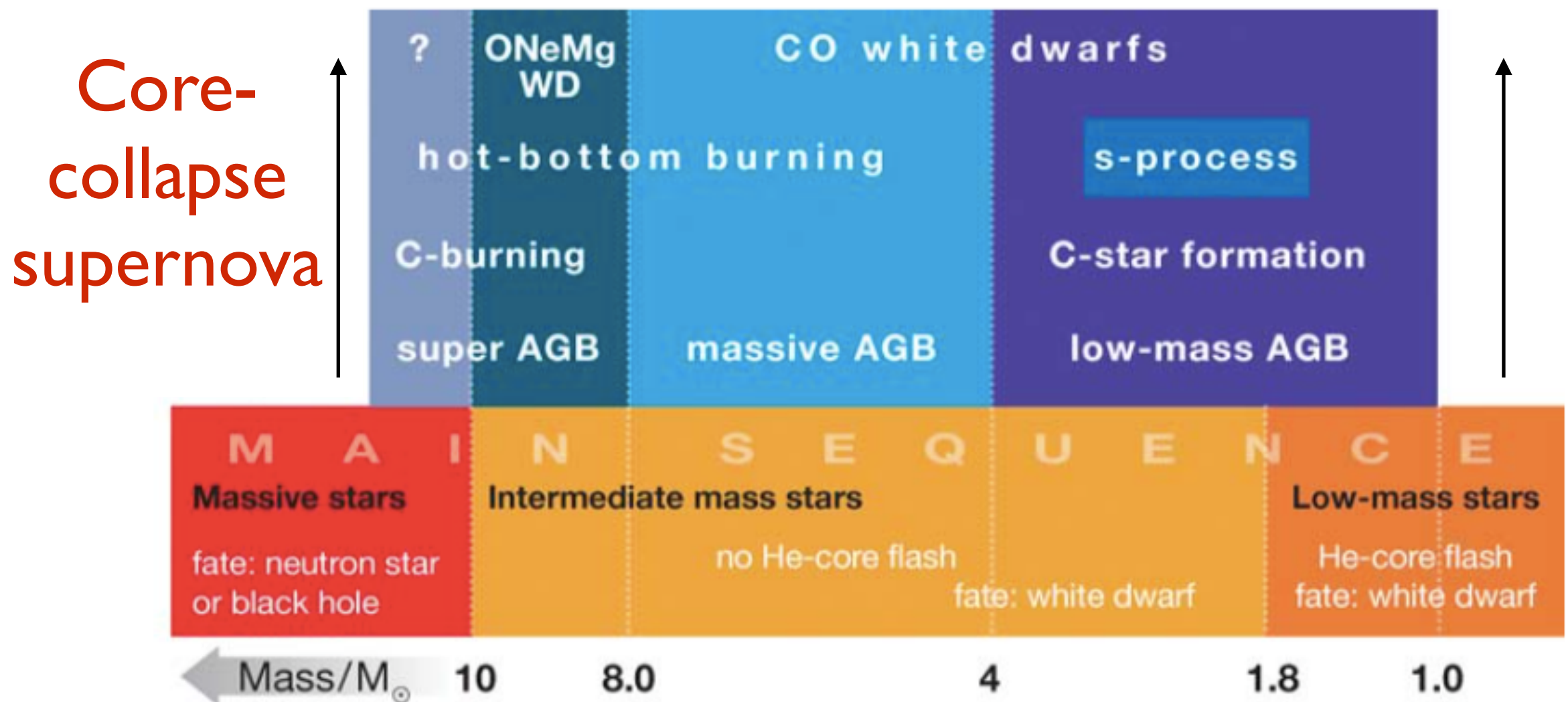
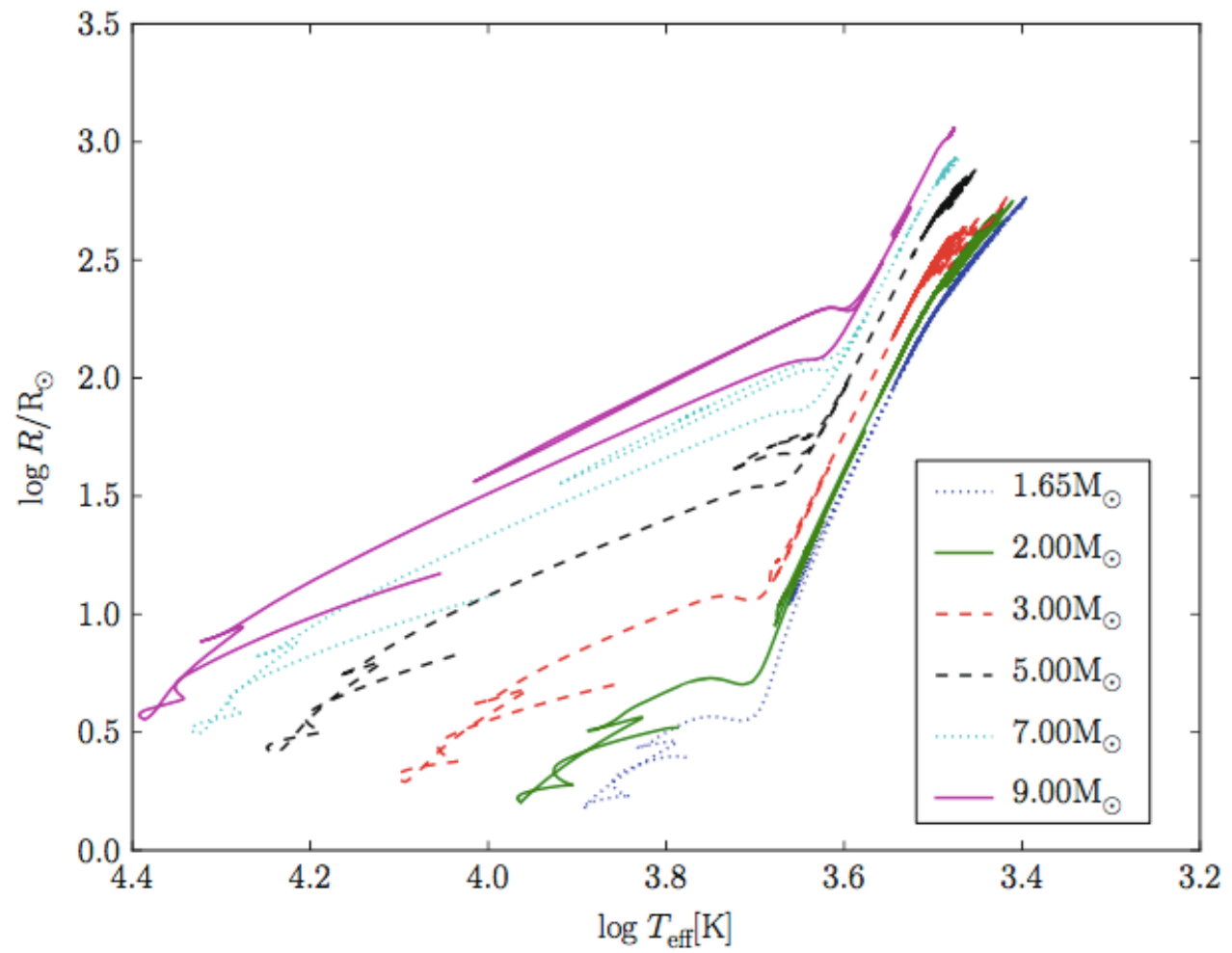


Figure 2 Classification of stars by mass on the main sequence (*lower part*) and on the AGB (*upper part*). The *lower part* shows mass designation according to initial mass. The *upper part* indicates the mass classification appropriate for AGB stars. Approximate limiting masses between different regimes are given at the bottom. These estimates are dependent on physics assumptions and input of models, as well as on metallicity. The different regimes have been labeled with some characterizing properties. The evolutionary fate of super-AGB stars is still uncertain (Section 5).

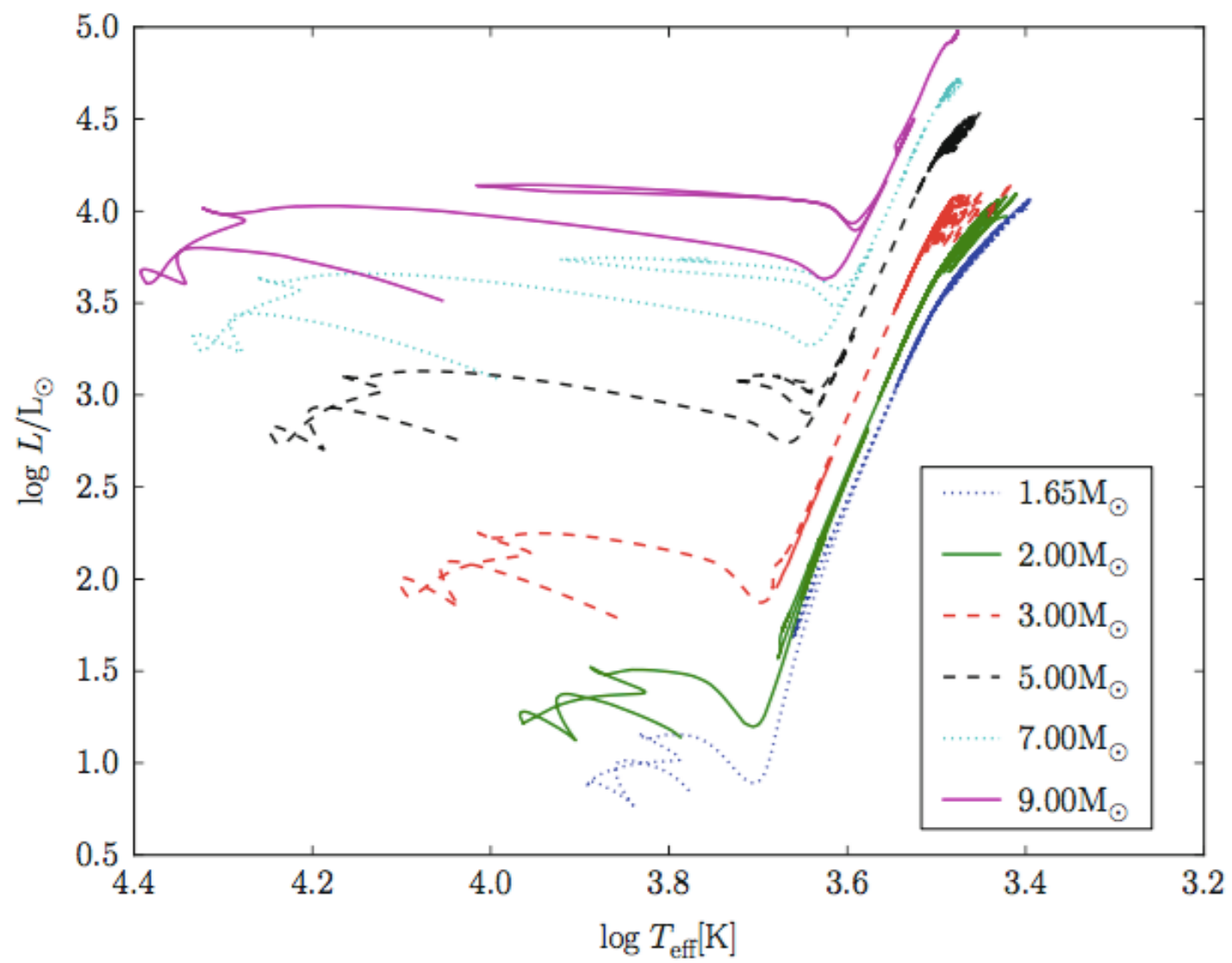
Evolution of low-mass stars [I]

► Hertzsprung-Russell diagram (HRD)



■ Fig. 8-2

Same as Fig. 8-1 but for the stellar radius. $\log T_{\text{eff}}$ – $\log R$ diagram for a range of masses with metallicity $Z = 0.02$



■ Fig. 8-1

Hertzsprung–Russell diagram (HRD) for a range of masses metallicity $Z = 0.02$. Most of the pre-main sequence has been omitted for clarity. One-dimensional models during the very advanced thermal-pulse AGB phase show erratic behavior of the surface parameters due to pulsations that is not shown here for clarity; see text for discussion

After today's afternoon session you will be able to make figures like this!

[I] F. Herwig, “Evolution of Solar and Intermediate-Mass Stars,” in Planets, Stars and Stellar Systems, vol 6, Dordrecht: Springer Netherlands, 2013, pp. 397–445.

Evolution of low-mass stars - abundance profiles to He-core burning

38

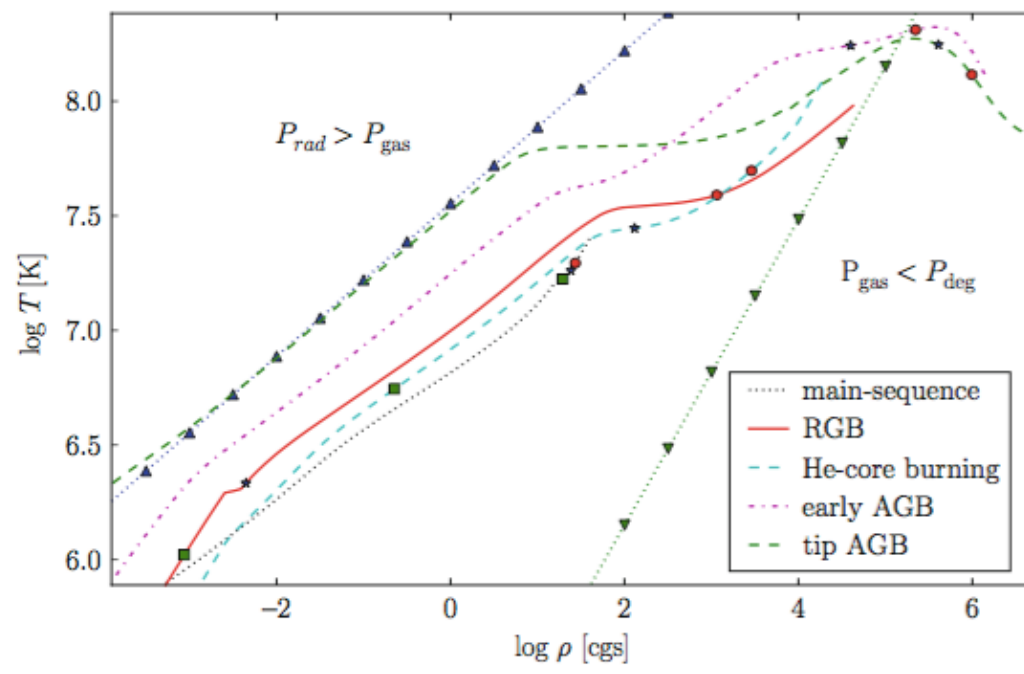


Fig. 8-6
Density-temperature profiles for the $3 M_{\odot}$ stellar evolution track for the evolutionary stages shown at times $\log t_{\text{final}} - t = 8.45, 8.04, 7.91, 6.23$, and 3.38 (in the order in which the lines appear in the legend) on the scale used in Fig. 8-7. The marks along each profile indicate the enclosed mass 0.35 (red circle), 0.5 (blue star), and $0.65 M_{\odot}$ (green square). Straight lines with triangle up and down marks divide areas dominated by radiation pressure, gas pressure, and the area dominated by the

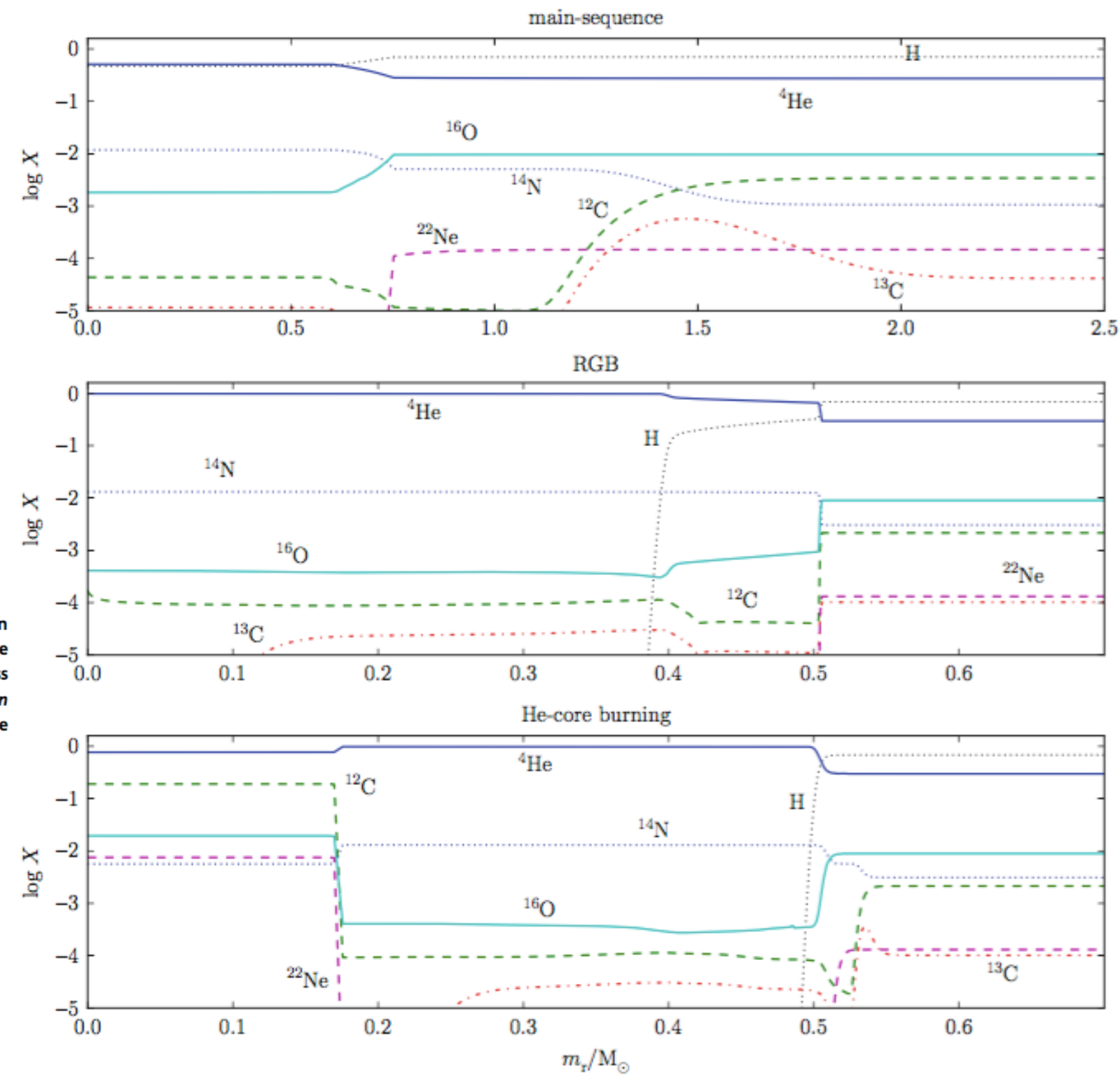
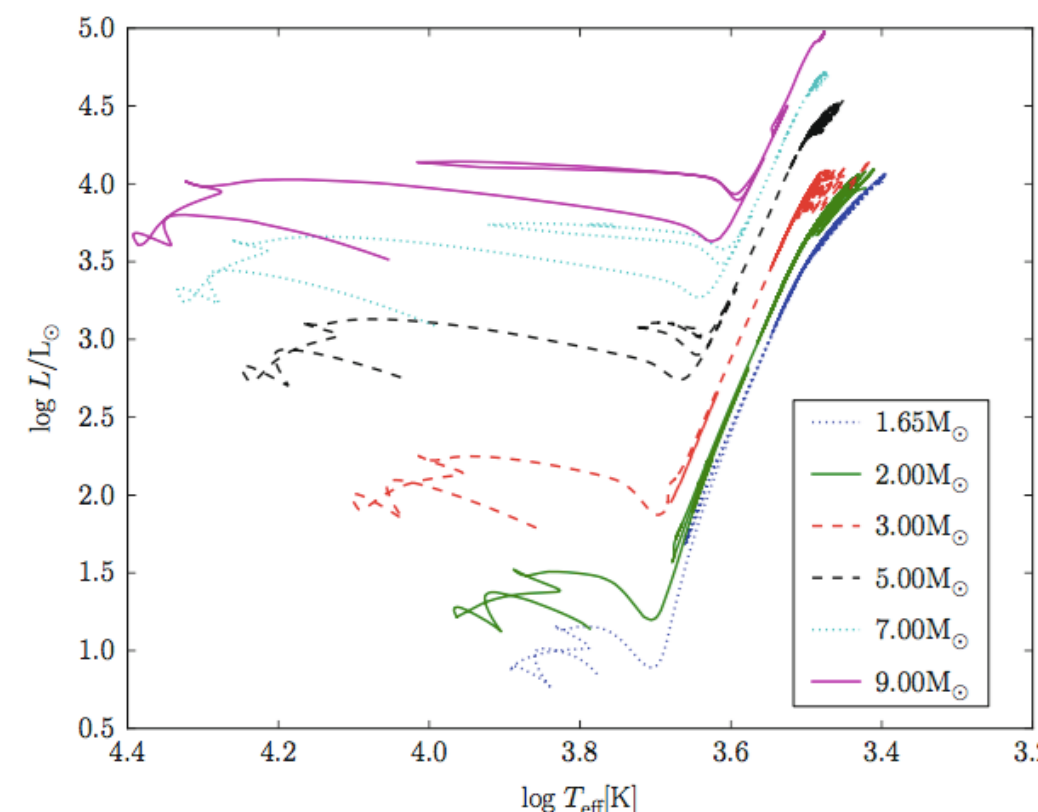


Fig. 8-5
Abundance profiles for the same evolutionary stages as shown in Fig. 8-6 (except the AGB profiles, which will be described in detail later, e.g., Fig. 8-14). The evolutionary stages shown at times $\log t_{\text{final}} - t = 8.45, 8.04, 7.91$ (top to bottom) on the scale used in Fig. 8-7

HRD of complete evolution of 3Msun star

39

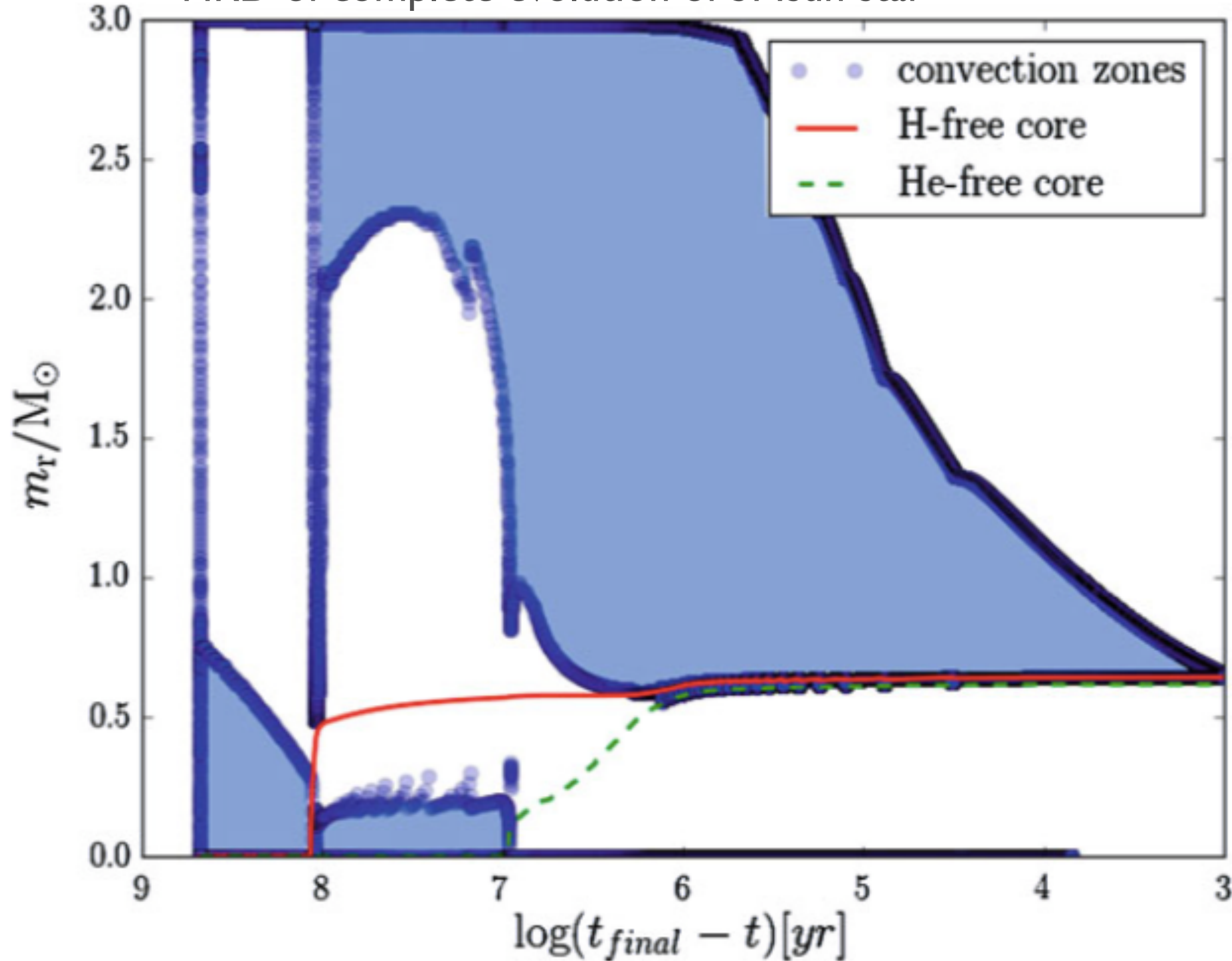
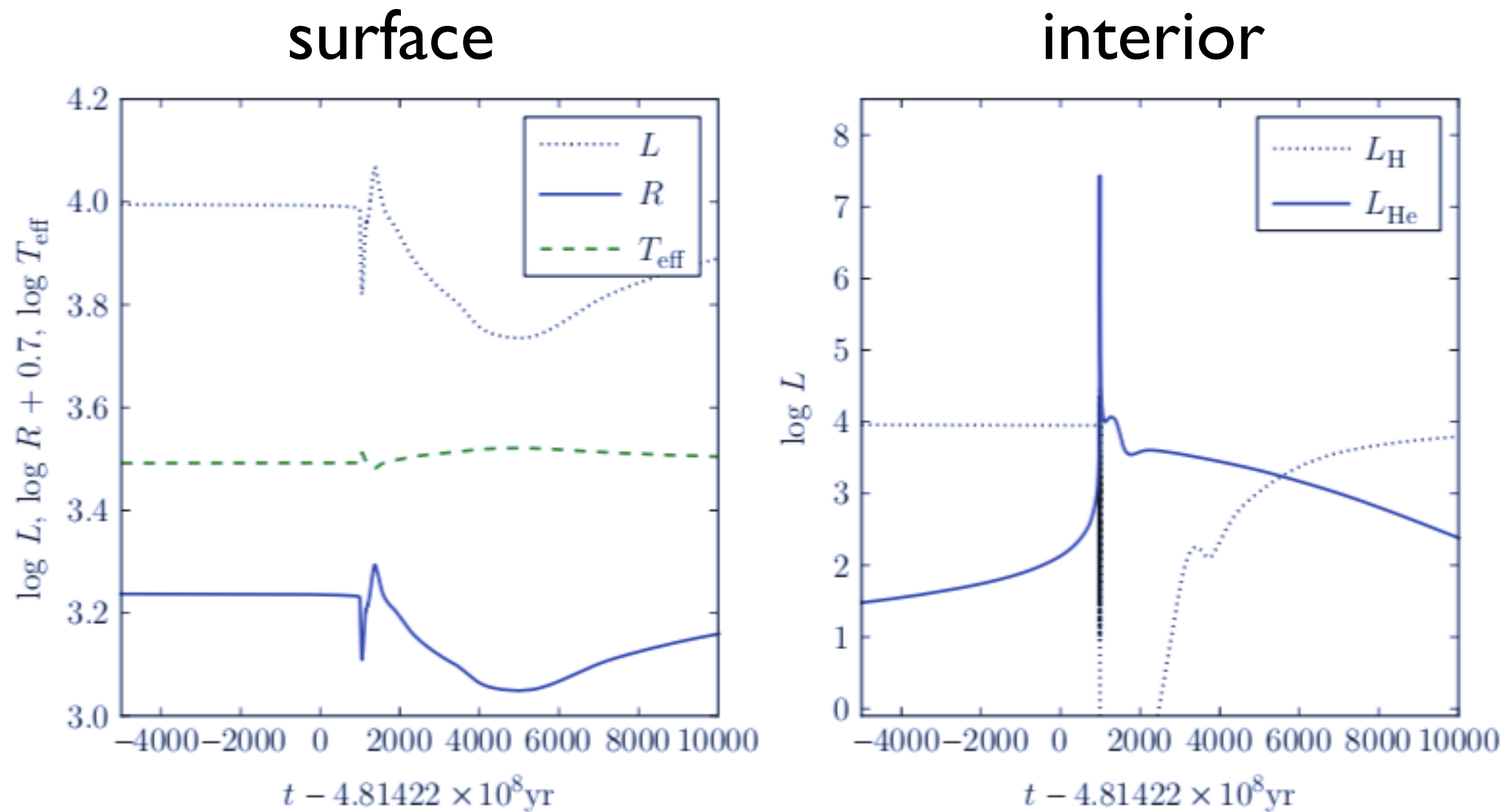


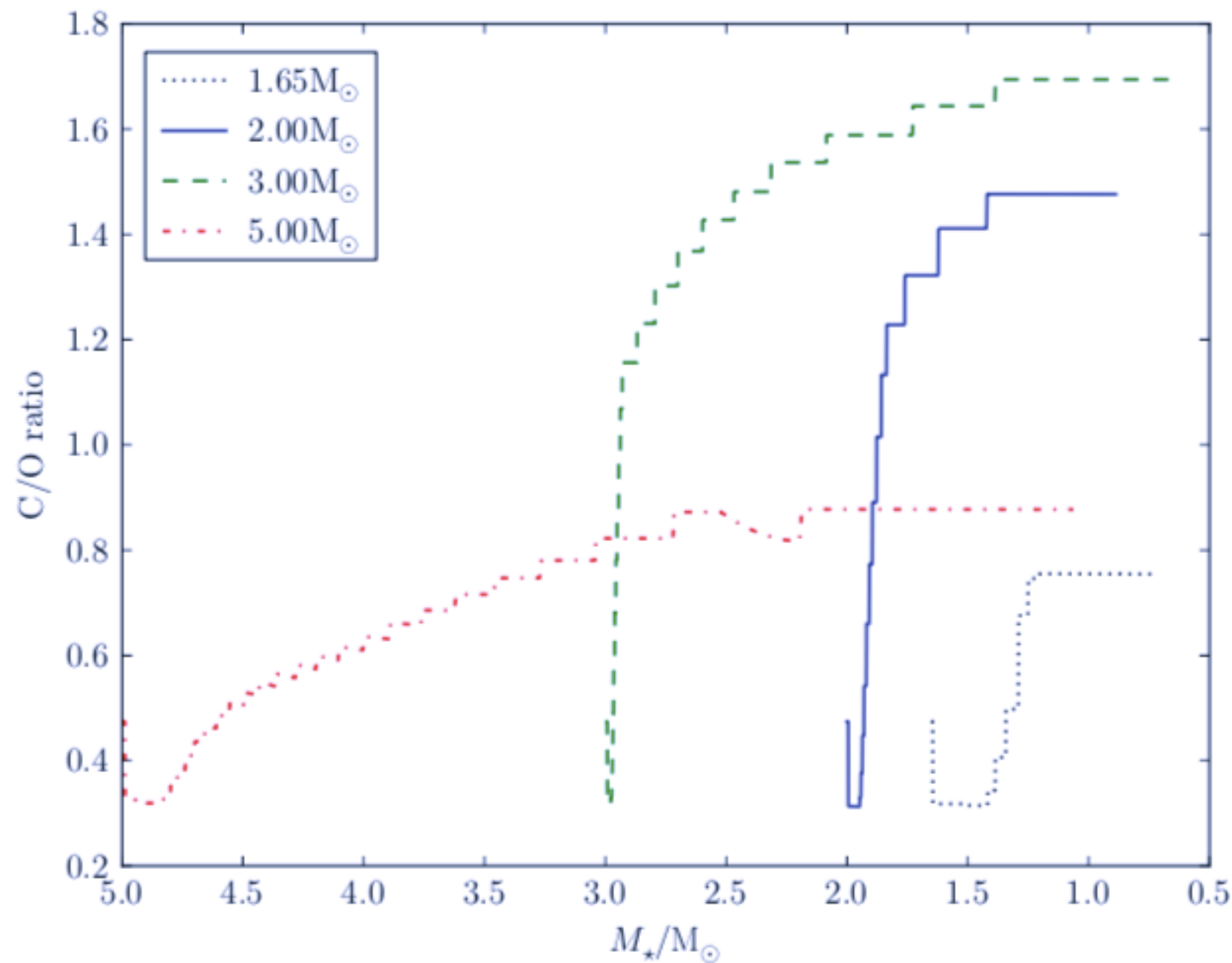
Fig. 8-7

Kippenhahn diagram of $M_{ZAMS} = 3 M_\odot$ stellar evolution calculation with $Z = 0.02$ from the pre-main sequence to the end of the TP-AGB evolution when all envelope mass is lost. The position

**Fig. 8-11**

Left panel: Surface parameters R , L , and T_{eff} before, during, and after the 12th He-shell flash of the $3 M_{\odot}$, $Z = 0.02$ stellar model track; *right panel:* luminosities of H burning and He burning. The time axis is the same as in [Fig. 8-10](#)

C/O ratio as
a function of
total mass
which
decreases
with time.



■ Fig. 8-12

Evolution of the C/O ratio (by number) as a function of stellar mass. Since the stellar mass decreases with time the C/O evolution corresponds to a time sequence from *left to right*

Thermal pulses in the Kippenhahn diagram

42

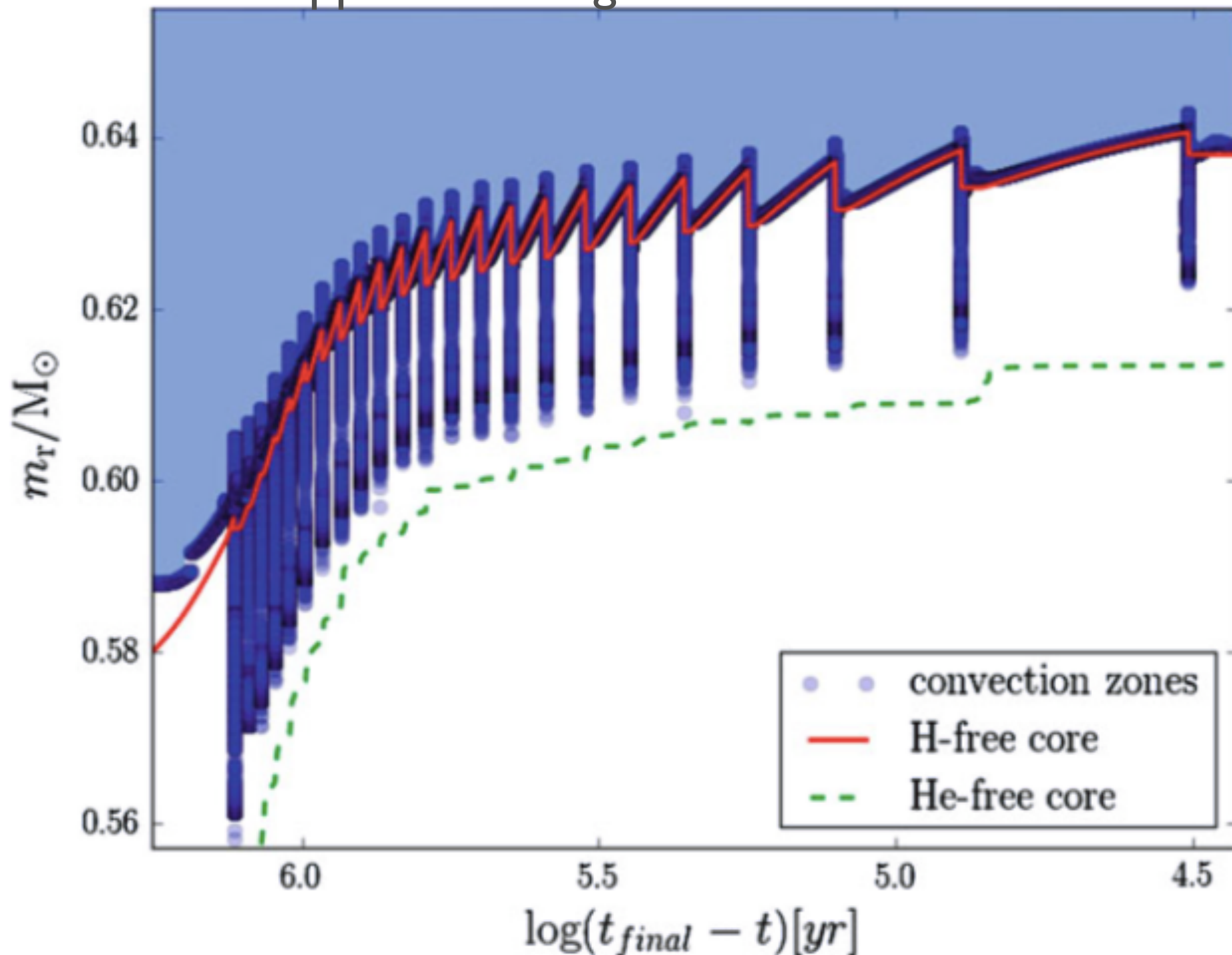


Fig. 8-9

Zoom-in of Kippenhahn diagram (Fig. 8-7), showing the sequence of thermal pulses. Sections where the mass coordinate of the H-free core increases correspond to H-shell burning phases, while a decrease of the H-free core indicates mixing of processed material from the intershell region (between the H- and He-free core) into the envelope via the third dredge-up

Kippenhahn diagram of two consecutive thermal pulses

43

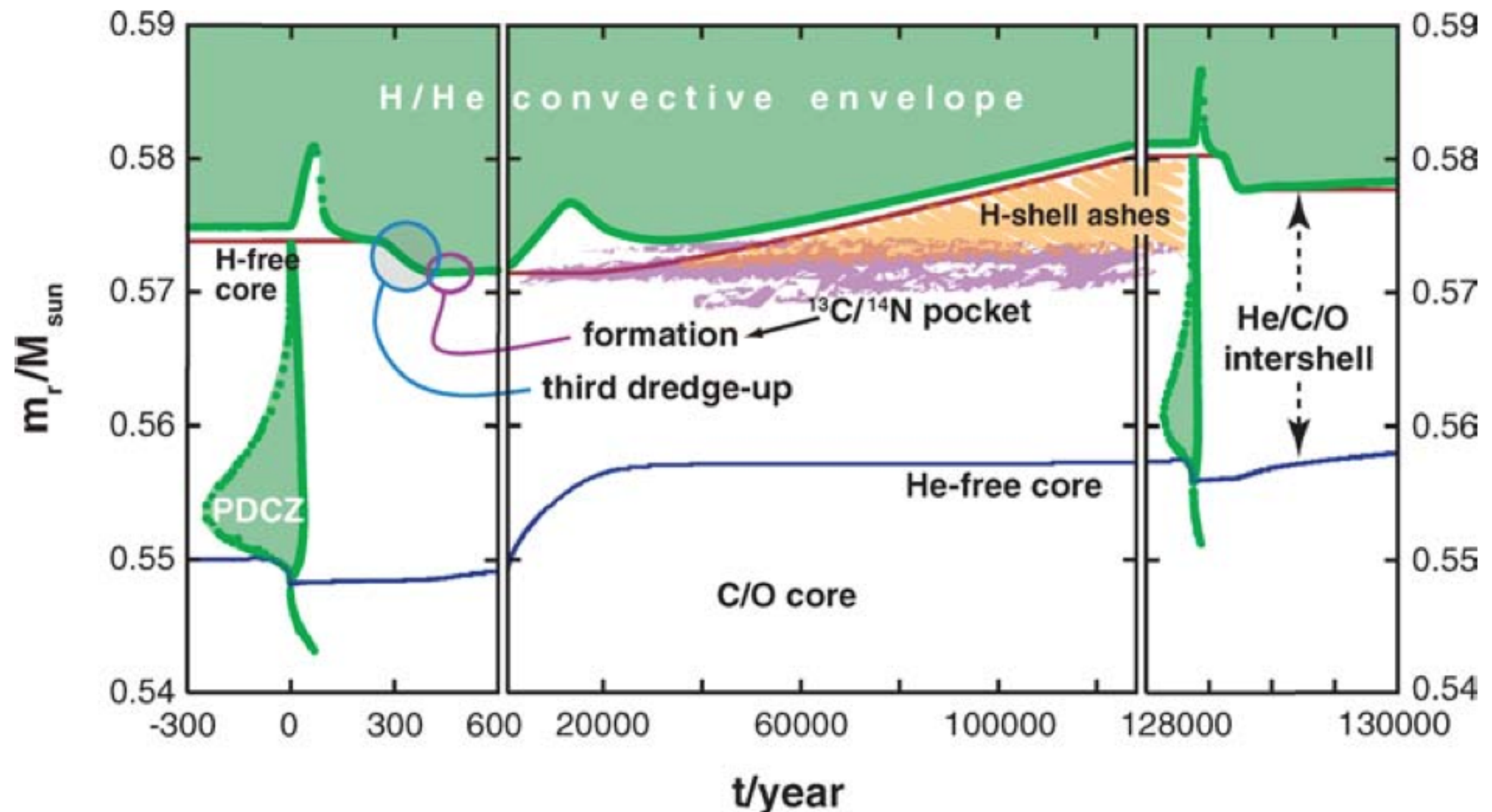
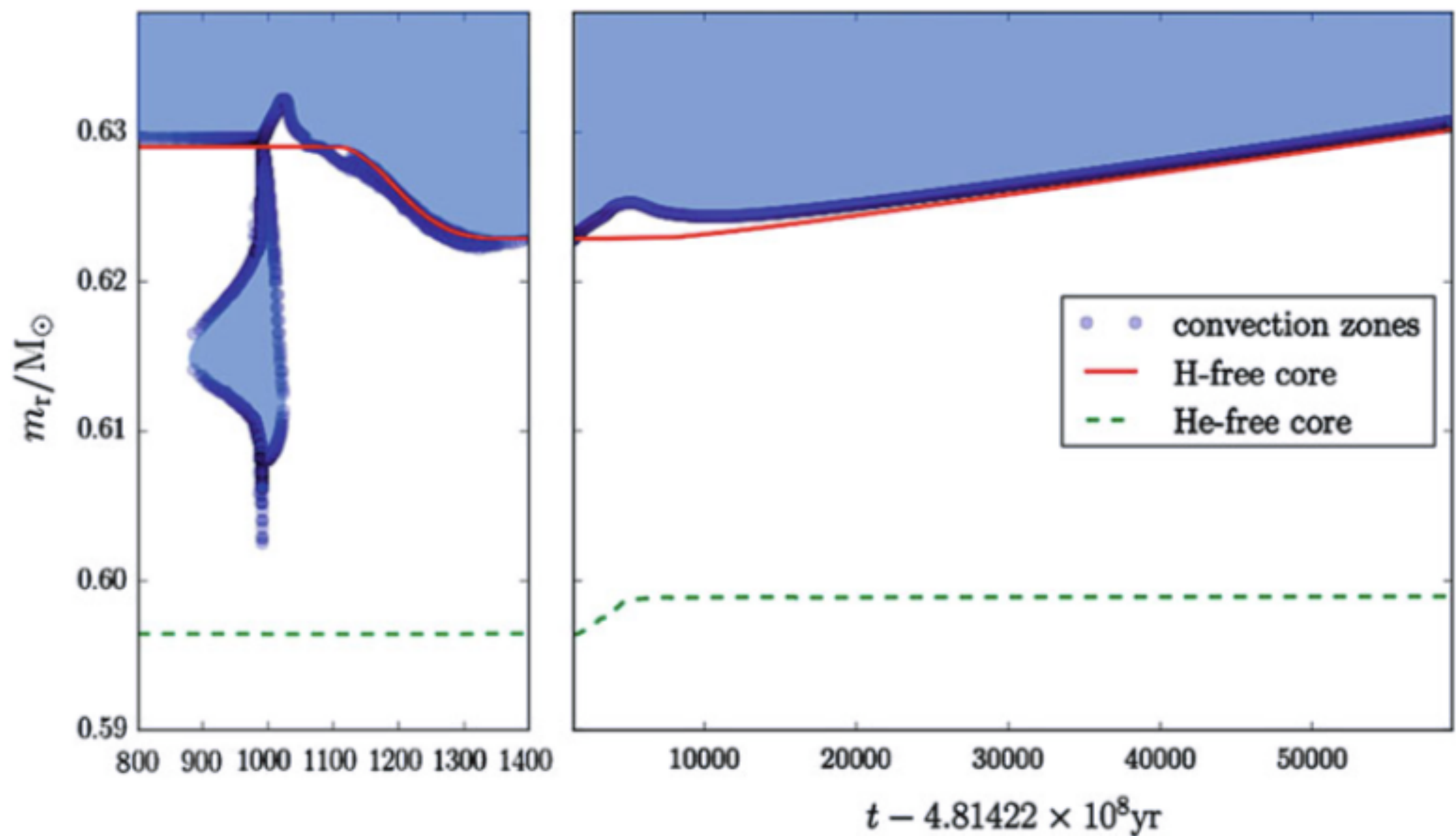


Figure 3 Thermal pulse 14, the subsequent interpulse phase and thermal pulse 15 of $2 M_{\odot}$, $Z = 0.01$ sequence ET2 of Herwig & Austin (2004). The timescale is different in each panel.

Almost the same again: one thermal pulse and following interpulse



■ Fig. 8-10

Kippenhahn diagram of the 12th thermal pulse (*left panel*) and the following interpulse phase (*right panel*). Note the different time scale for the two panels. The thermal pulses are very short compared to the interpulse phase

Abundance profiles - H-burning shell

45

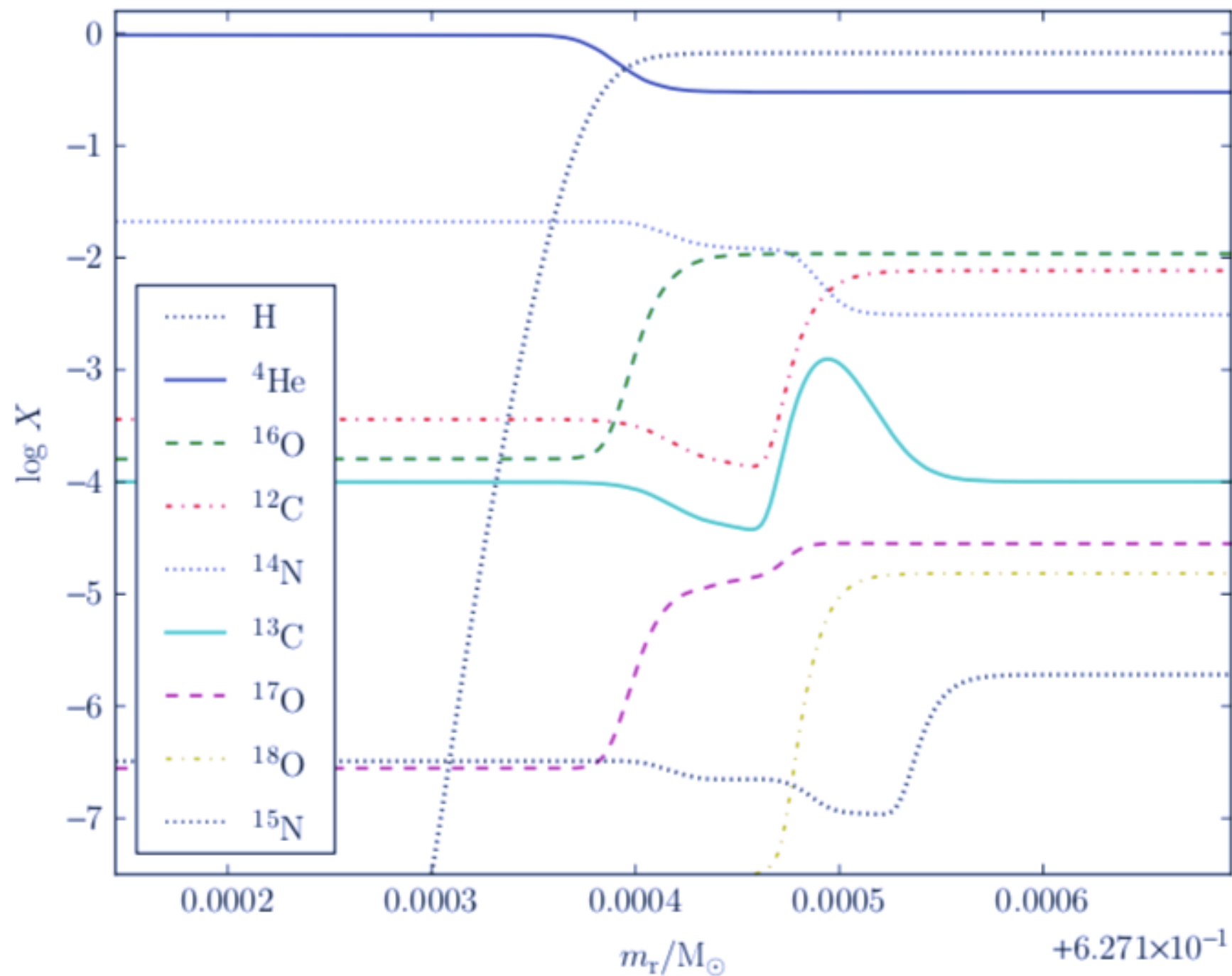


Fig. 8-13

Profiles of H, ${}^4\text{He}$ and the CNO isotopes in the H-burning shell during the interpulse period at time $t=41,011$ yr on the time scale of Fig. 8-10. The order of species in the legend corresponds to the abundance of the species at the right edge of the diagram, from top to bottom

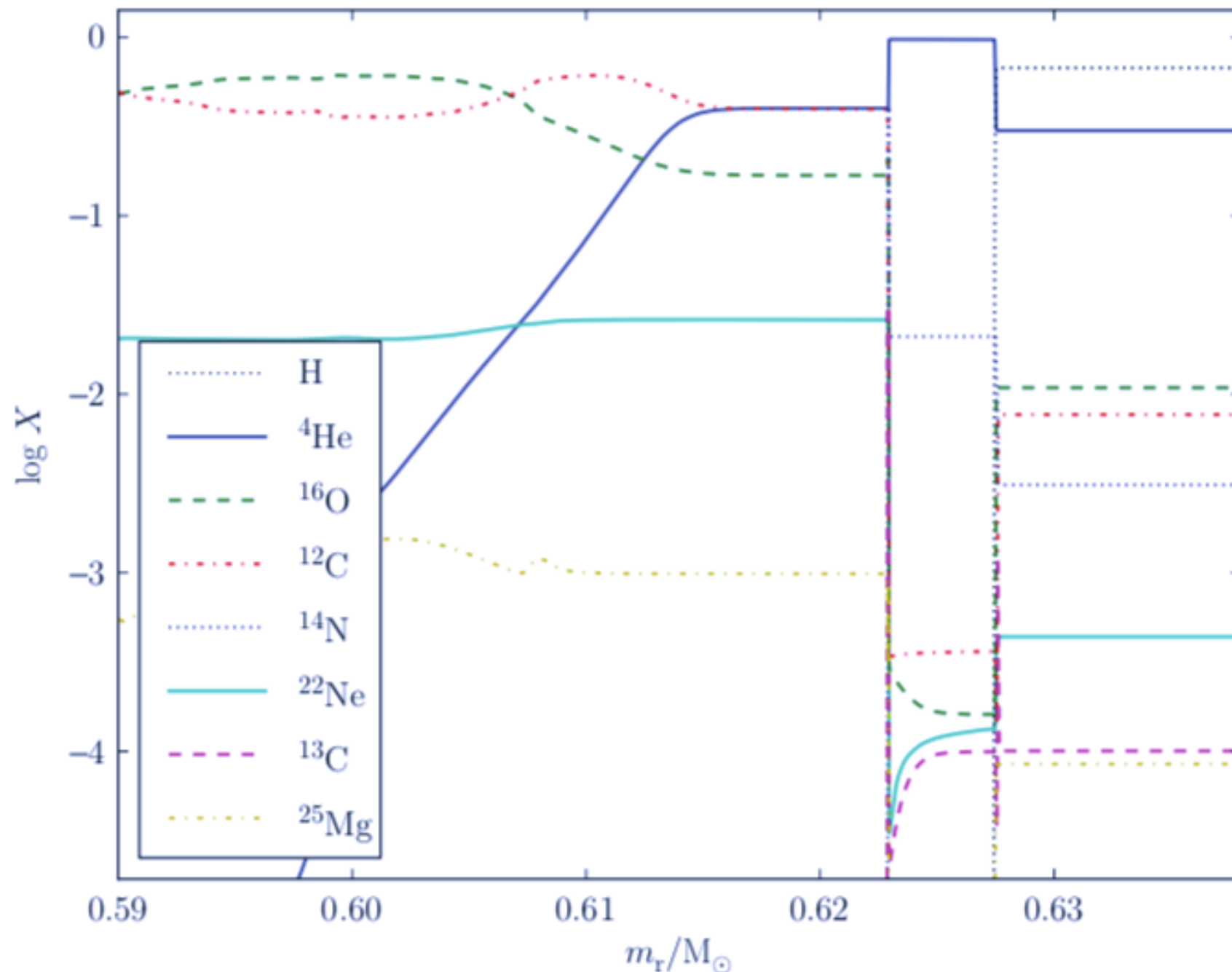
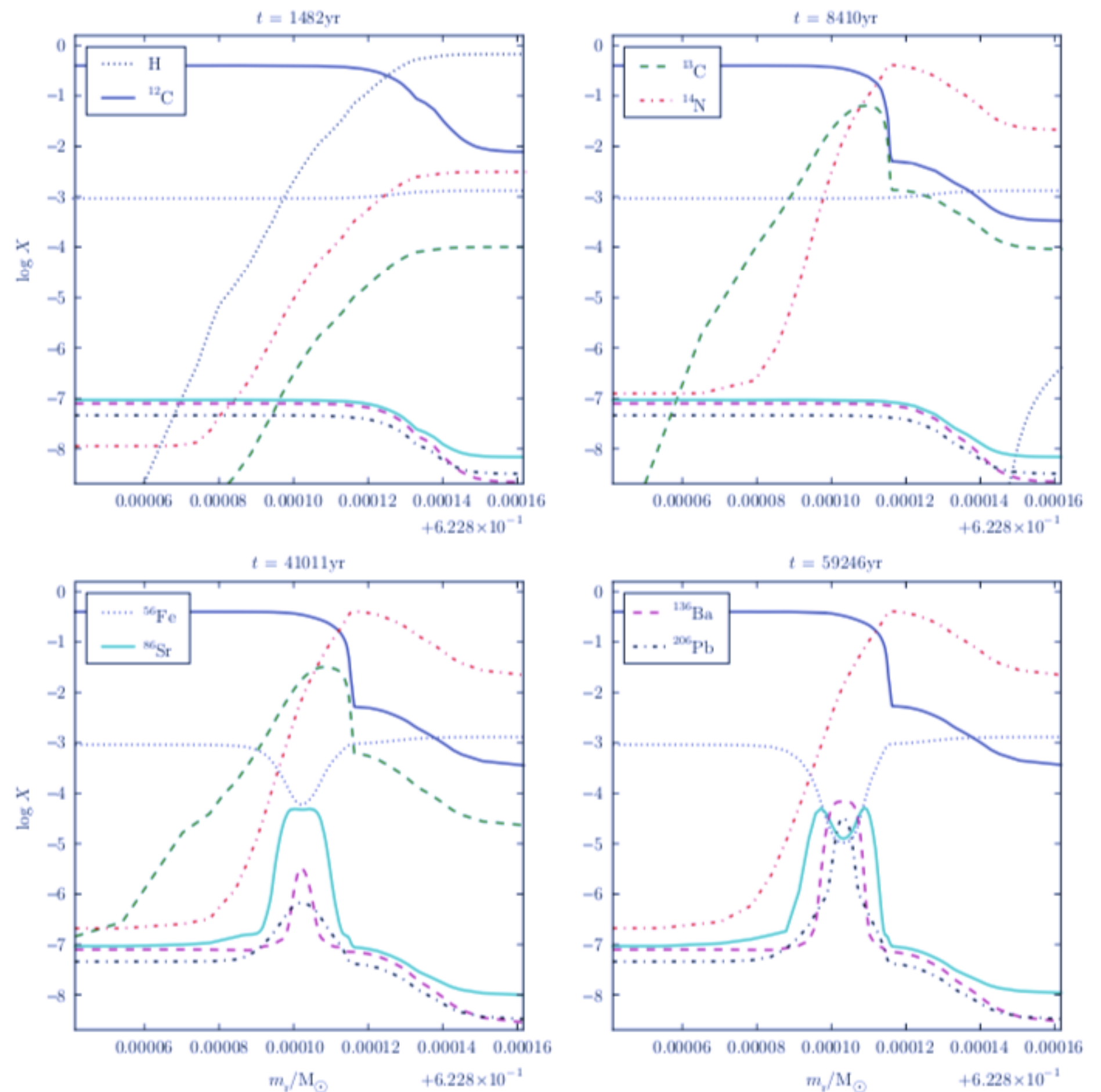


Fig. 8-14

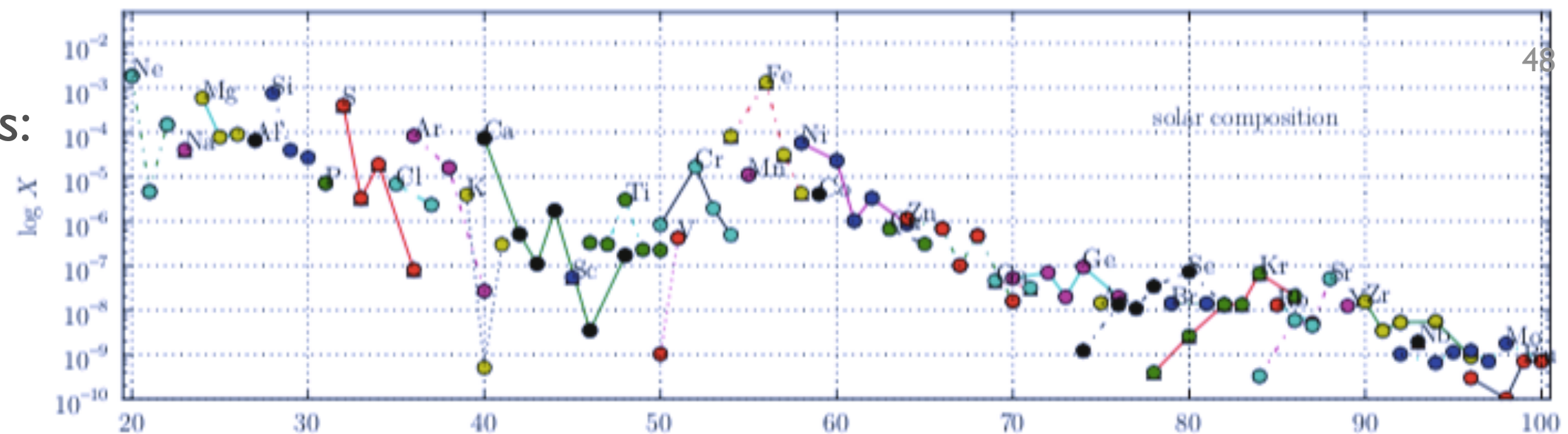
Profiles of key species from the CO core through the intershell region and the H-shell burning ashes and to the bottom of the convective envelope. As in Fig. 8-13, the point in time of this profile is $t = 41,011$ yr on the time scale of Fig. 8-10. The mass range is the same as in the Kippenhahn diagram Fig. 8-10. The order of species in the legend corresponds to the abundance of the species at the right edge of the diagram, from top to bottom

Abundance profile evolution in the C13 pocket

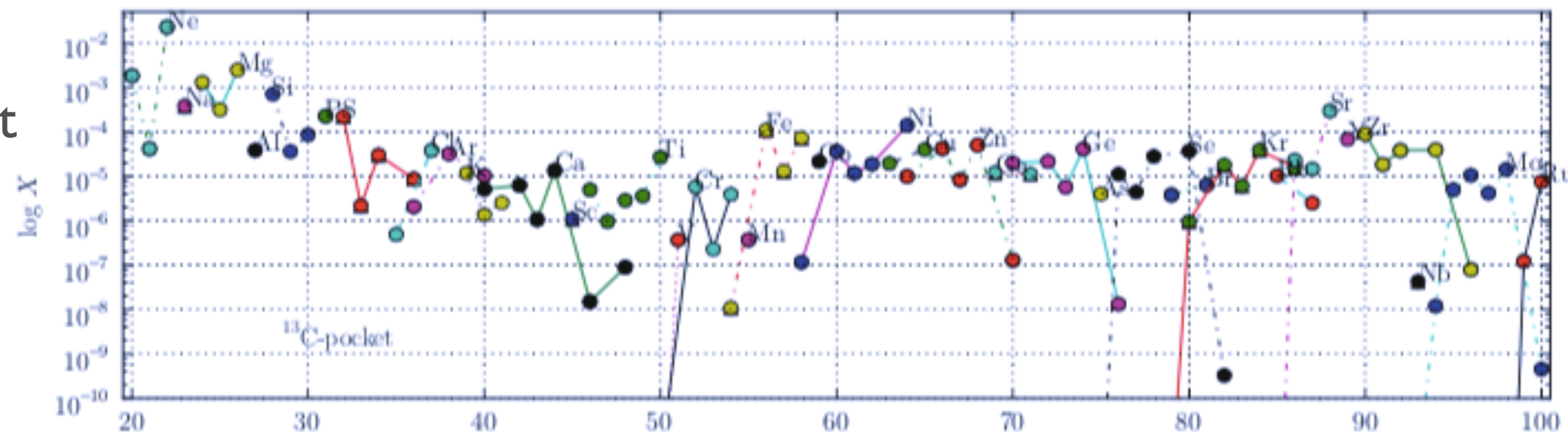


Abundance distributions:

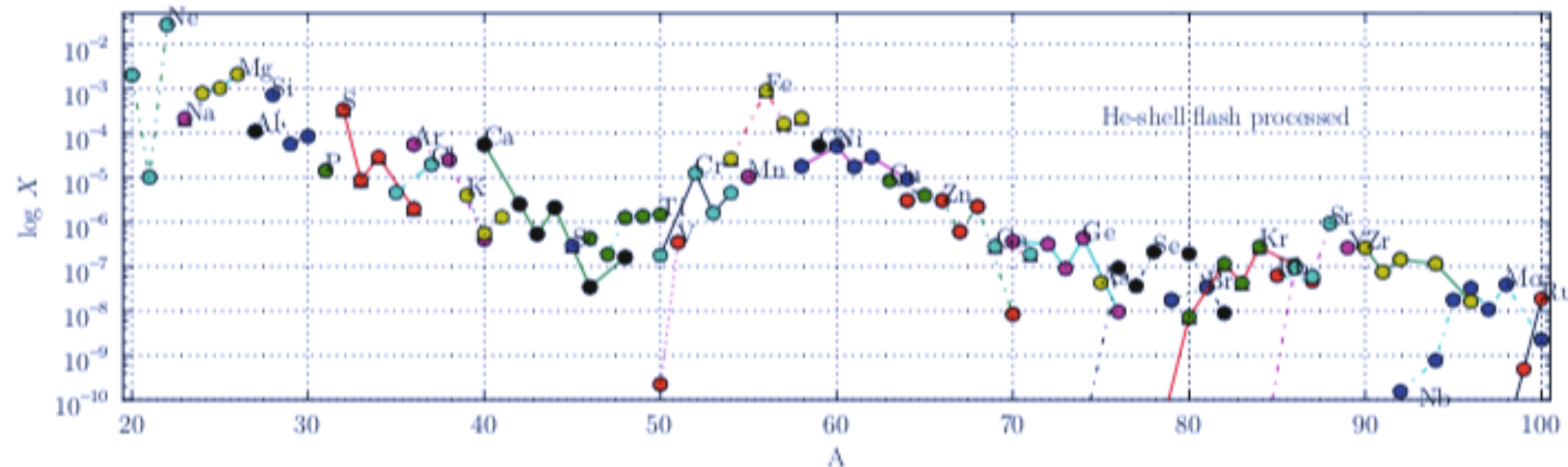
- solar



- ^{13}C pocket



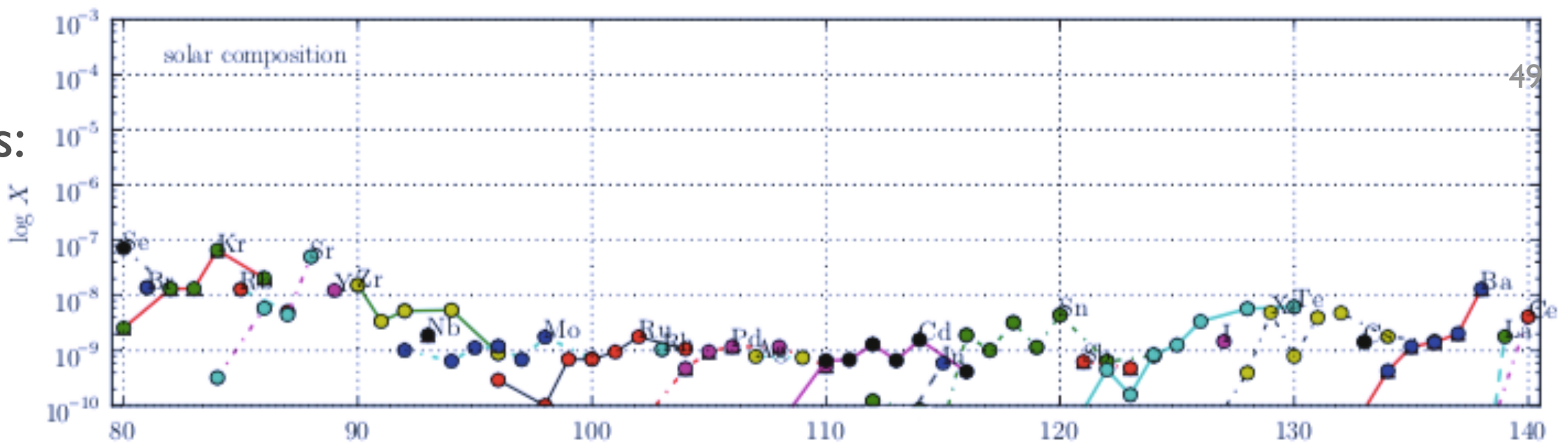
- He-flash intershell



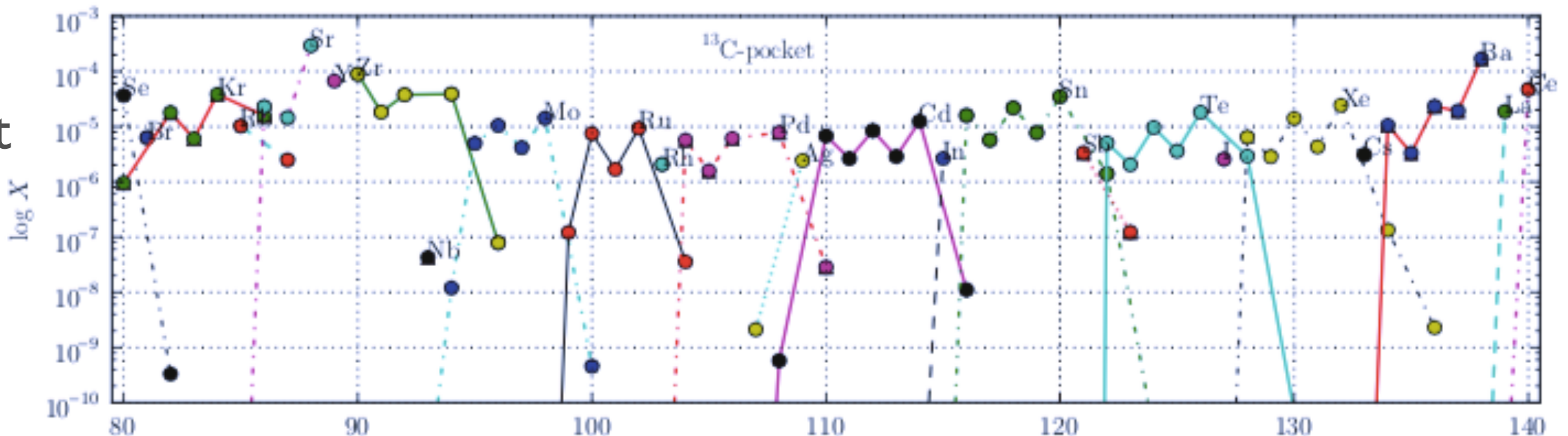
Abundance distributions:

49

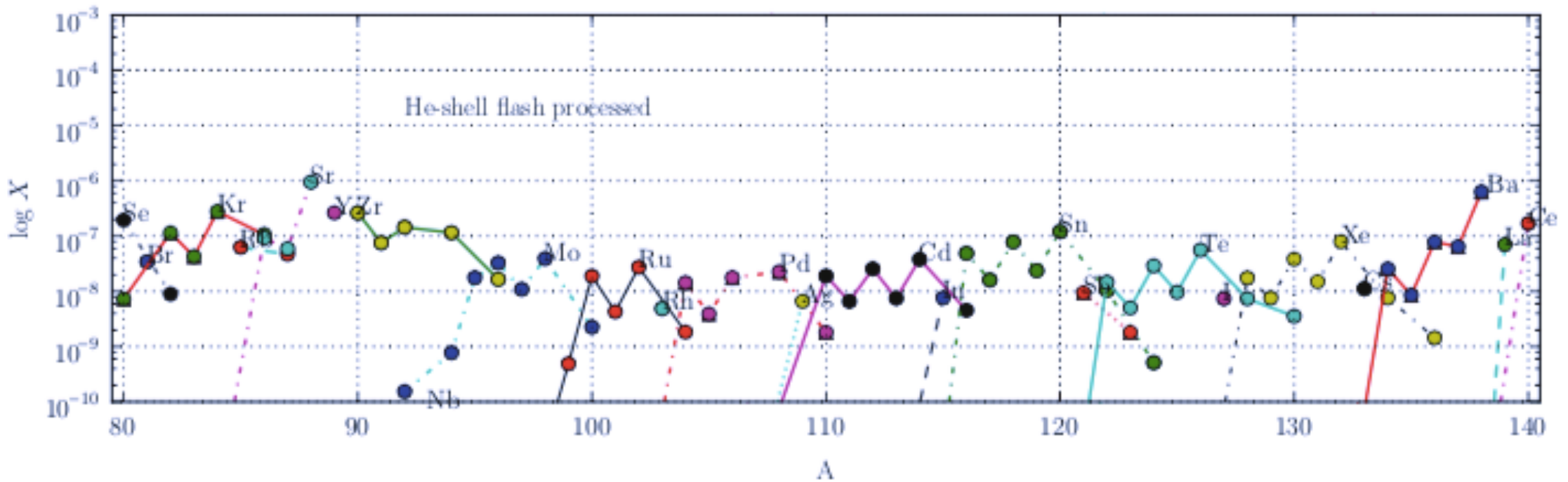
- solar



- ^{13}C pocket

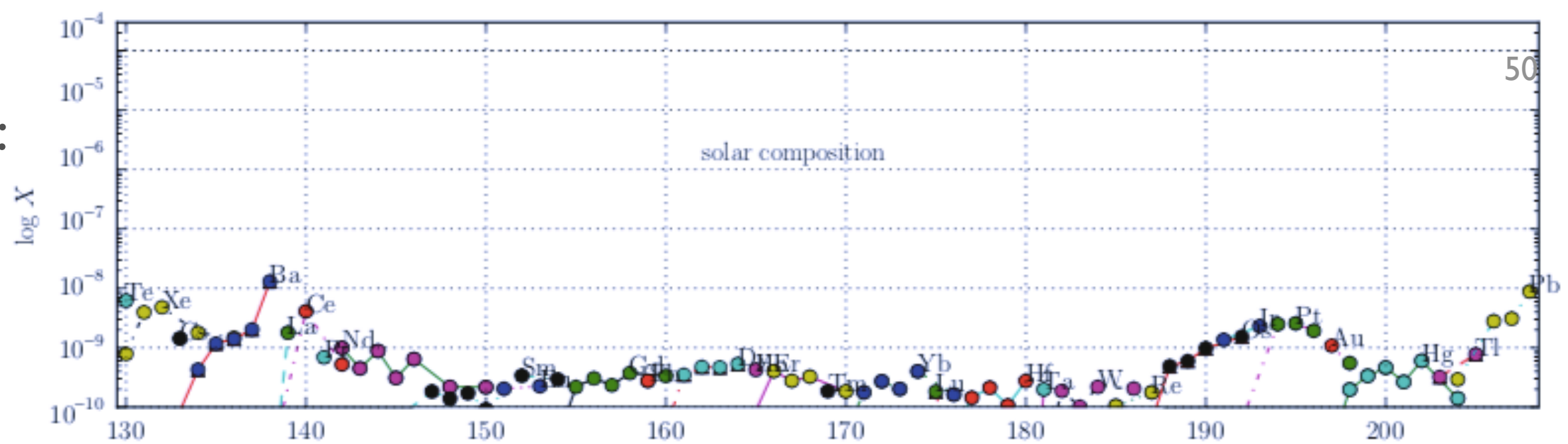


- He-flash intershell

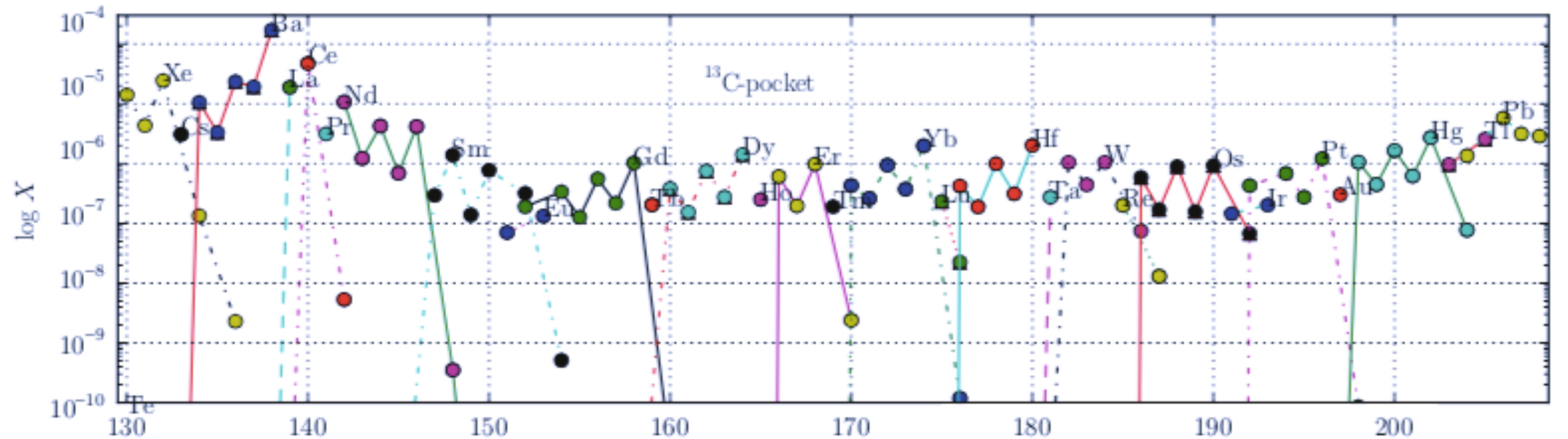


Abundance distributions:

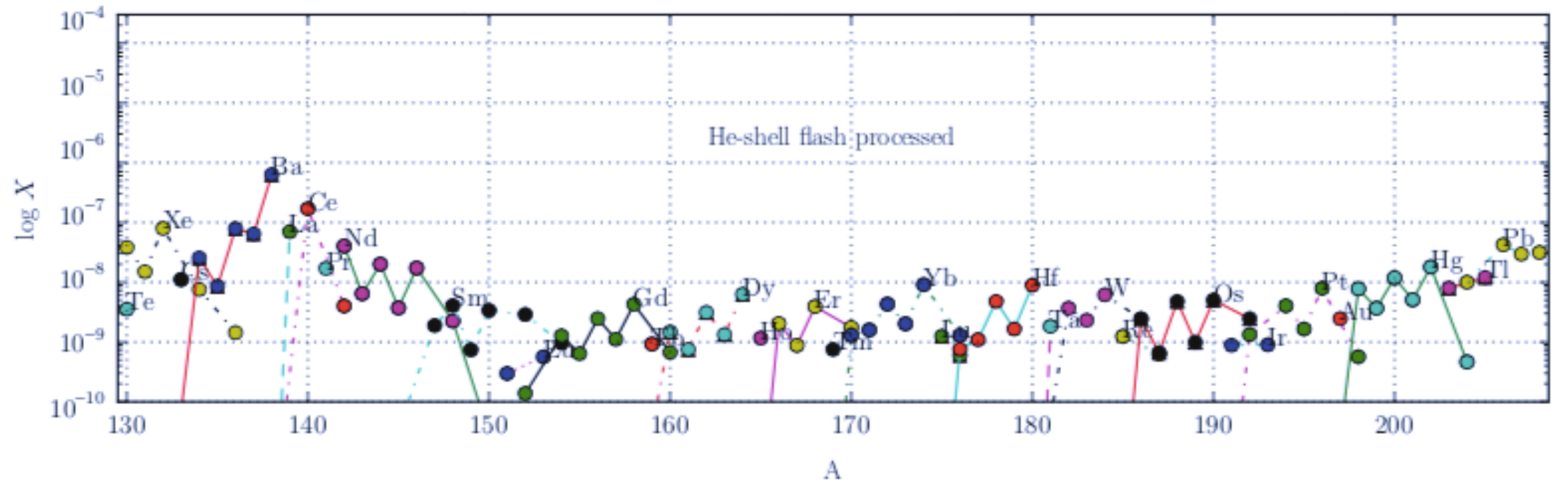
- solar



- ^{13}C pocket



- He-flash intershell



Properties as a function of mass

51

Fig. 8-20

Stellar age versus initial mass for $Z = 0.02$ (solid line with circles) and $Z = 6 \times 10^{-4}$ (dashed line with triangles)

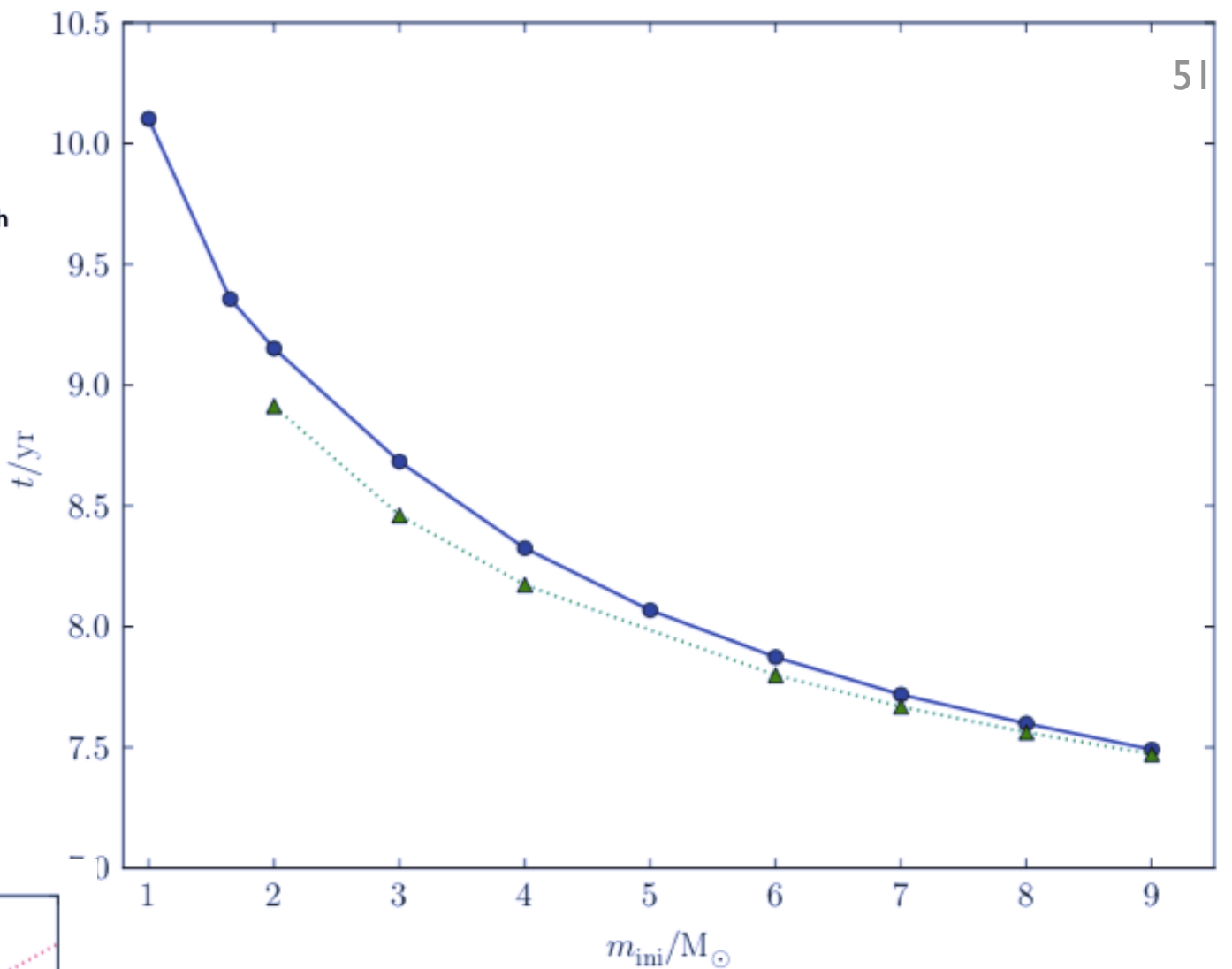
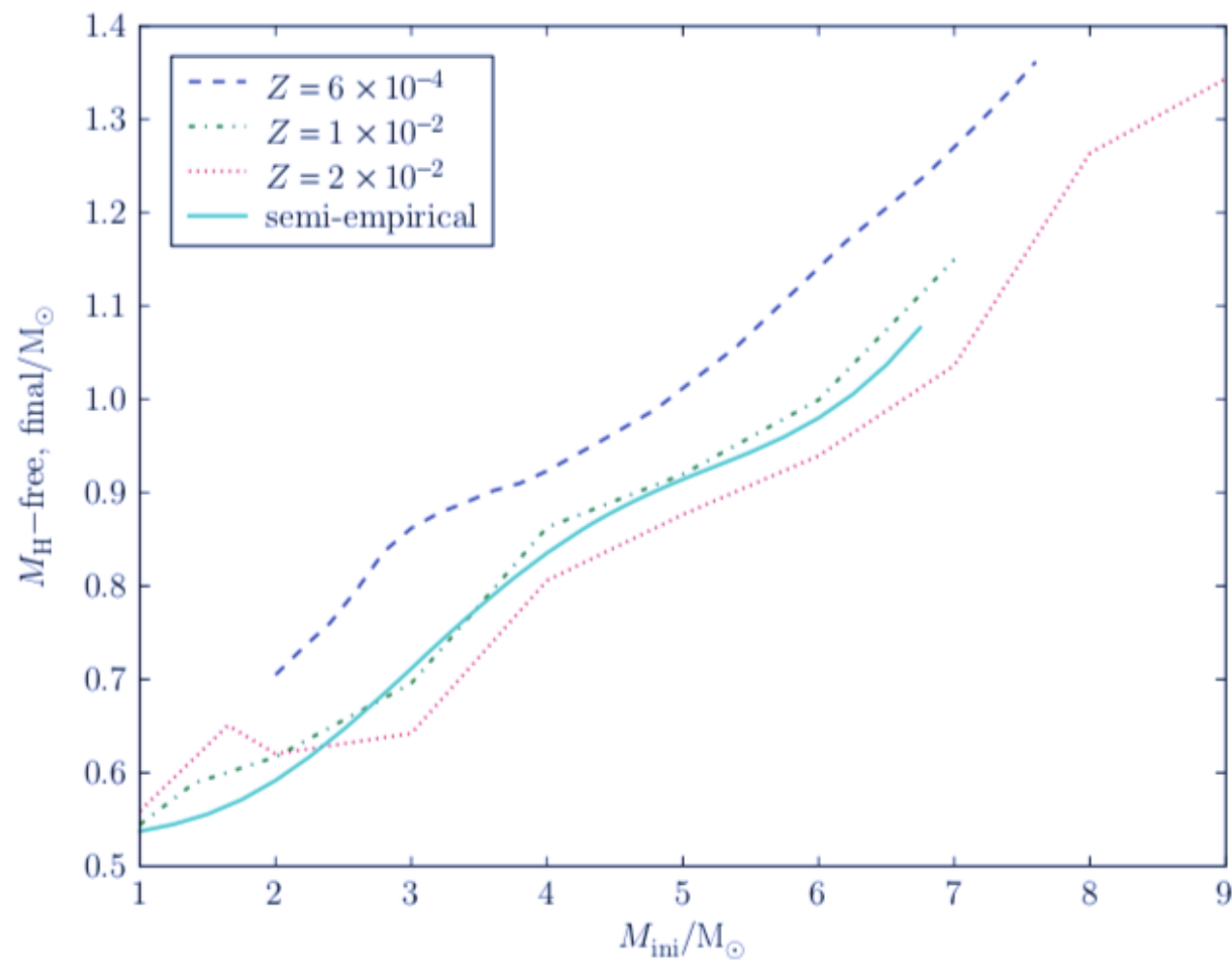


Fig. 8-21

H-free core mass at the last computed thermal pulse as a function of initial mass. Each relation is based on a grid of sequences that have been computed to the tip of the AGB when all mass is lost or close enough to the point that very little change of the core mass is expected before the model stars evolve to become white dwarfs. Therefore, the shown relations constitute theoretical initial to final mass relations for the given metallicities. The line with the label *semiempirical* represents the curvature MiMf that Ferrario et al. (2005) found to best reproduce the white dwarf mass distribution from the Palomar-Green survey

Massive stars

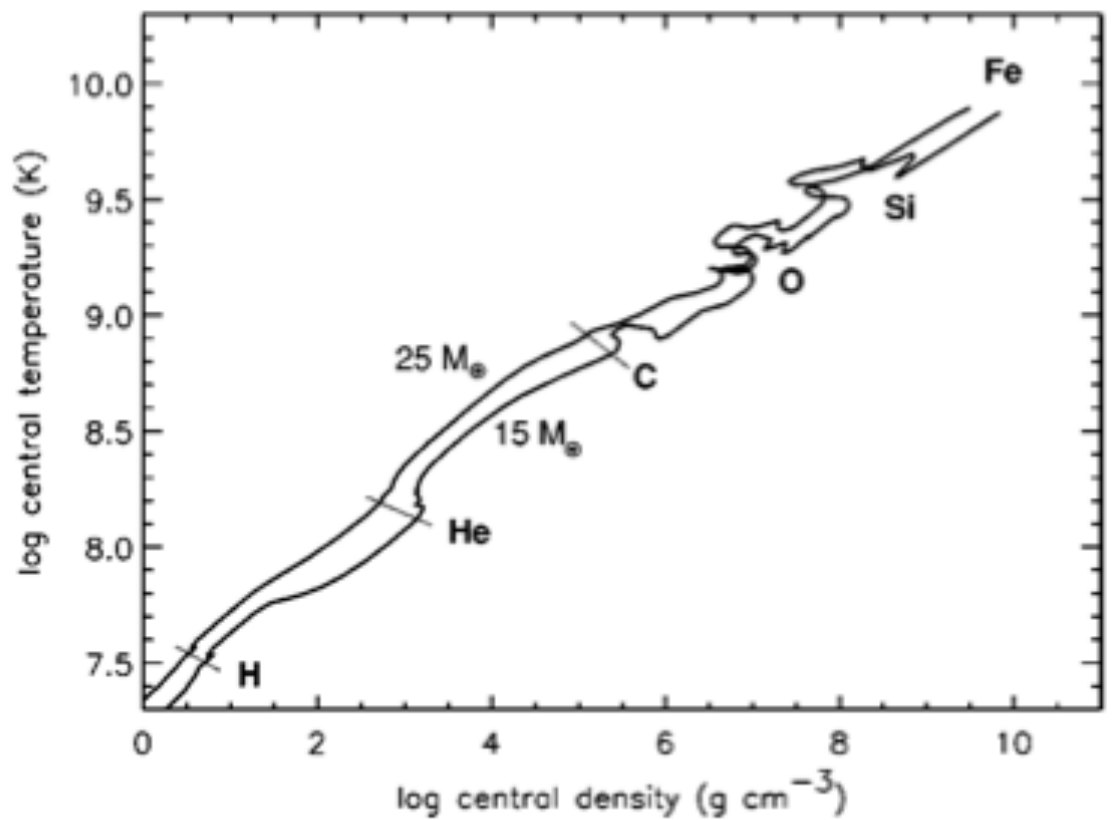


FIG. 1. Evolution of the central temperature and density in stars of $15 M_{\odot}$ and $25 M_{\odot}$ from birth as hydrogen-burning stars until iron-core collapse (Table I). In general, the trajectories follow a line of $\rho \propto T^3$, but with some deviation downwards (towards higher ρ at a given T) due to the decreasing entropy of the core. Nonmonotonic behavior is observed when nuclear fuels are ignited and this is exacerbated in the $15 M_{\odot}$ model by partial degeneracy of the gas.

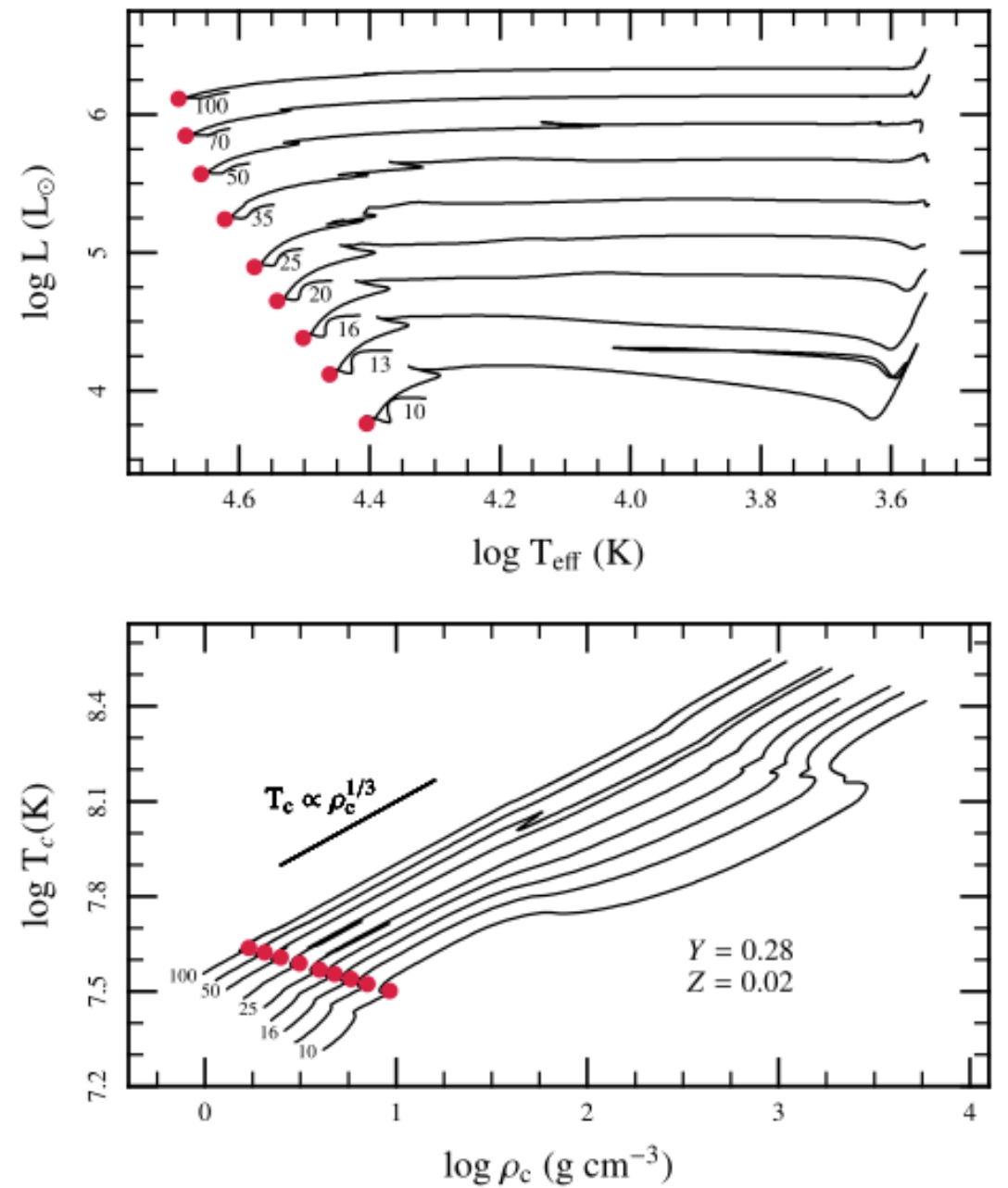


Figure 29. Top: H-R diagram for $10-100 M_{\odot}$ models from the PMS to the end of core Helium burning for $Z = 0.02$ but with zero mass loss. Bottom: trajectories of the central conditions in the $T-\rho$ plane over this same evolutionary period.

Evolution of a massive (15 solar mass) star

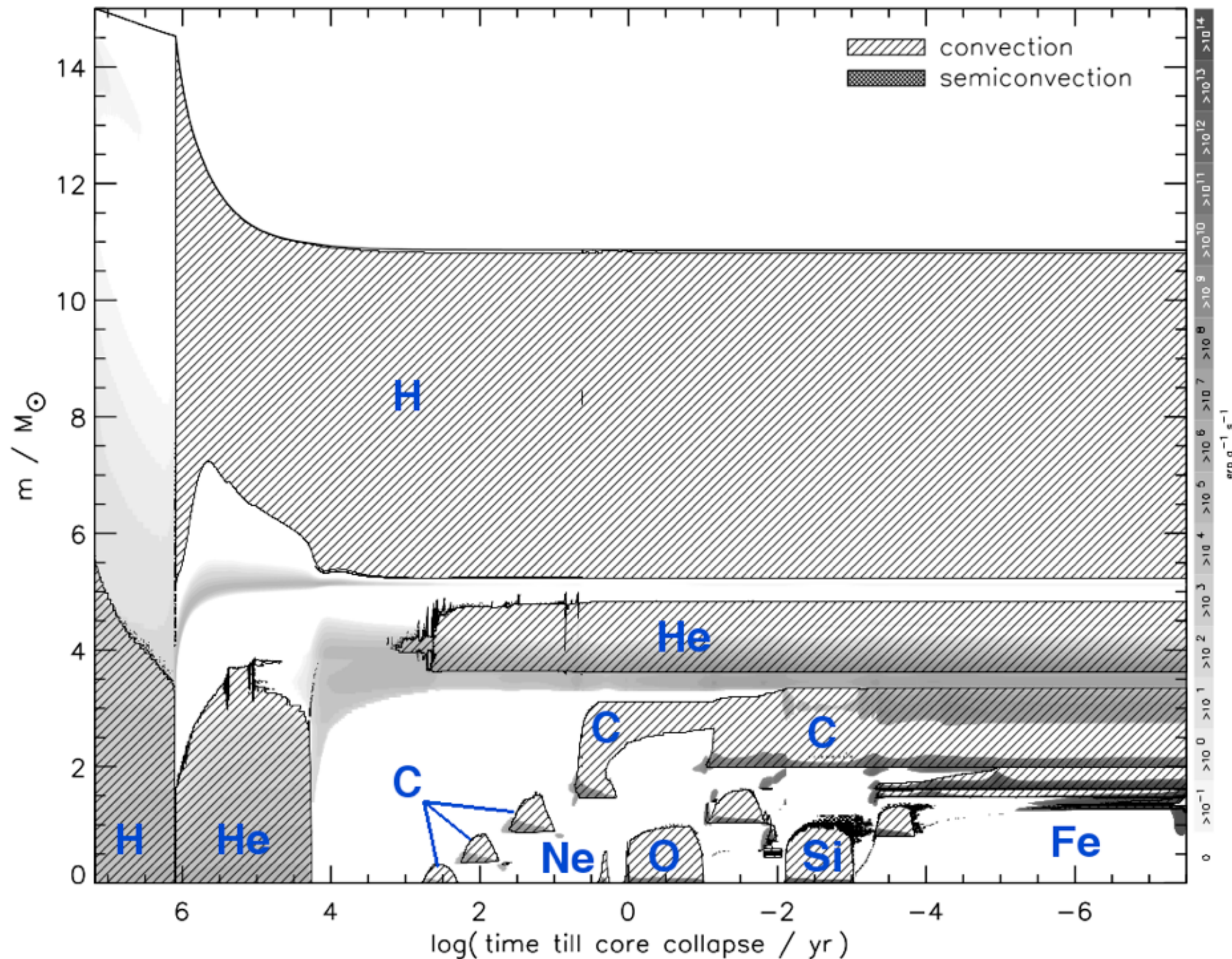


TABLE I. Burning stages of stars.

Hydrogen burning						
	T	ρ	M	L	R	τ
M_{\odot}	10^7 K	g cm^{-3}	M_{\odot}	$10^3 L_{\odot}$	R_{\odot}	Myr
1 ^{a,b}	1.57	153	1.00	0.001	1.00	~1100
13	3.44	6.66	12.9	18.3	6.24	13.5
15	3.53	5.81	14.9	28.0	6.75	11.1
20	3.69	4.53	19.7	62.6	8.03	8.13
25	3.81	3.81	24.5	110	9.17	6.70
75	4.26	1.99	67.3	916	21.3	3.16
75 ^c	7.60	10.6	75.0	1050	9.36	3.44

Helium burning						
	T	ρ	M	L	R	τ
M_{\odot}	10^8 K	10^3 g cm^{-3}	M_{\odot}	$10^3 L_{\odot}$	R_{\odot}	Myr
1 ^b	1.25	20	0.71	0.044	~10	110
13	1.72	1.73	12.4	26.0	359	2.67
15	1.78	1.39	14.3	41.3	461	1.97
20	1.88	0.968	18.6	102	649	1.17
25	1.96	0.762	19.6	182	1030	0.839
75	2.10	0.490	16.1	384	1.17	0.478
75 ^c	2.25	0.319	74.4	1540	702	0.332

Carbon burning

M_{initial} M_{\odot}	T 10^8 K	ρ 10^5 g cm^{-3}	M M_{\odot}	L $10^3 L_{\odot}$	R R_{\odot}	τ kyr
13	8.15	3.13	11.4	60.6	665	2.82
15	8.34	2.39	12.6	83.3	803	2.03
20	8.70	1.70	14.7	143	1070	0.976
25	8.41	1.29	12.5	245	1390	0.522
75	8.68	1.39	6.37	164	0.644	1.07
75 ^c	10.4	0.745	74.0	1550	714	0.027

Neon burning

M_{initial} M_{\odot}	T 10^9 K	ρ 10^6 g cm^{-3}	M M_{\odot}	L $10^3 L_{\odot}$	R R_{\odot}	τ yr
13	1.69	10.8	11.4	64.4	690	0.341
15	1.63	7.24	12.6	86.5	821	0.732
20	1.57	3.10	14.7	147	1090	0.599
25	1.57	3.95	12.5	246	1400	0.891
75	1.62	5.21	6.36	167	0.715	0.569
75 ^c	1.57	0.434	74.0	1560	716	0.026

Oxygen burning

M_{initial} M_{\odot}	T 10^9 K	ρ 10^6 g cm^{-3}	M M_{\odot}	L $10^3 L_{\odot}$	R R_{\odot}	τ yr
13	1.89	8.19	11.4	64.5	691	4.77
15	1.94	6.66	12.6	86.6	821	2.58
20	1.98	5.55	14.7	147	1090	1.25
25	2.09	3.60	12.5	246	1400	0.402
75	2.04	4.70	6.36	172	0.756	0.908
75 ^c	2.39	1.07	74.0	1550	716	0.010

Rev. Mod. Phys., Vol. 74, No. 4, October 2002

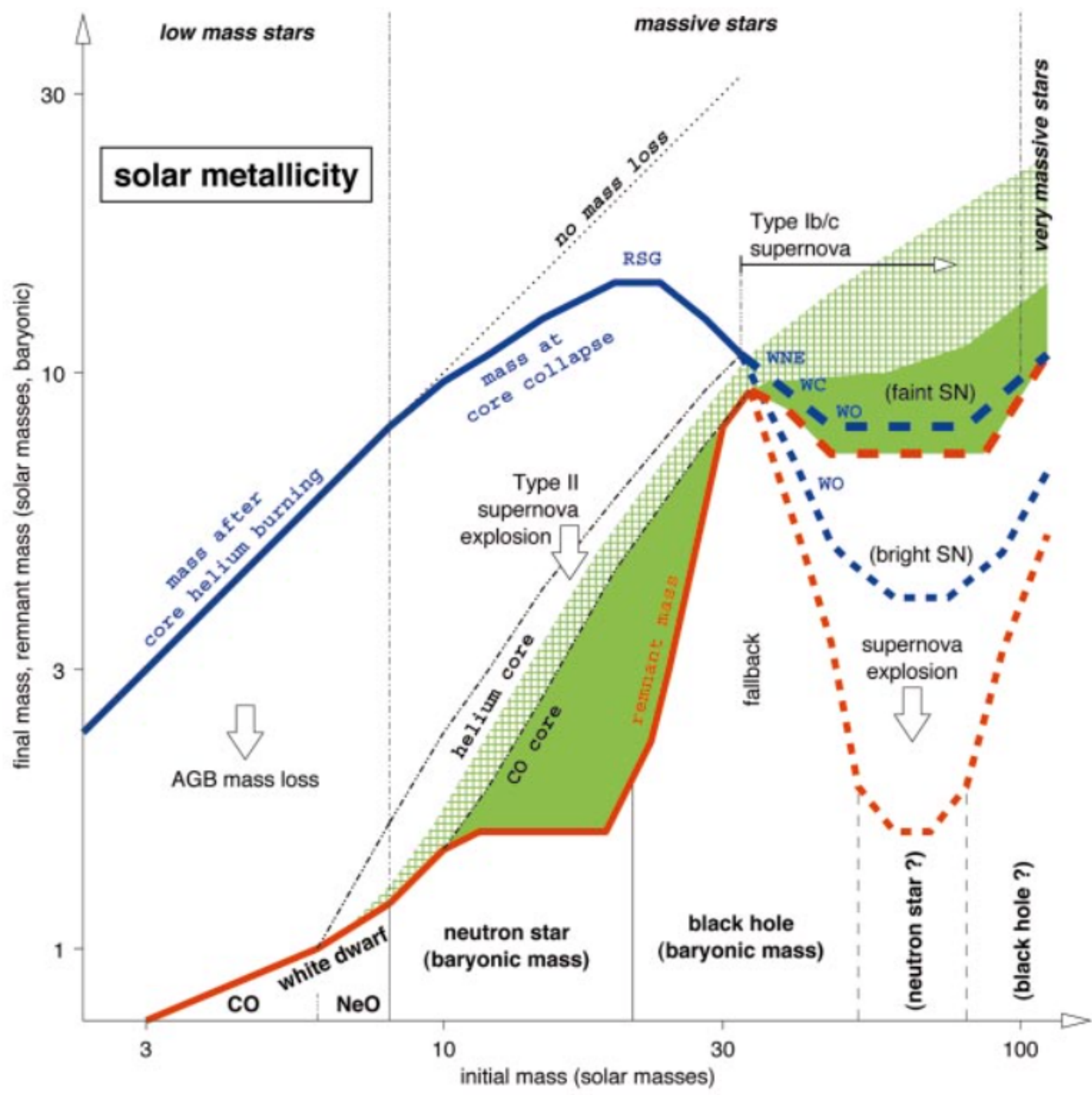
1020

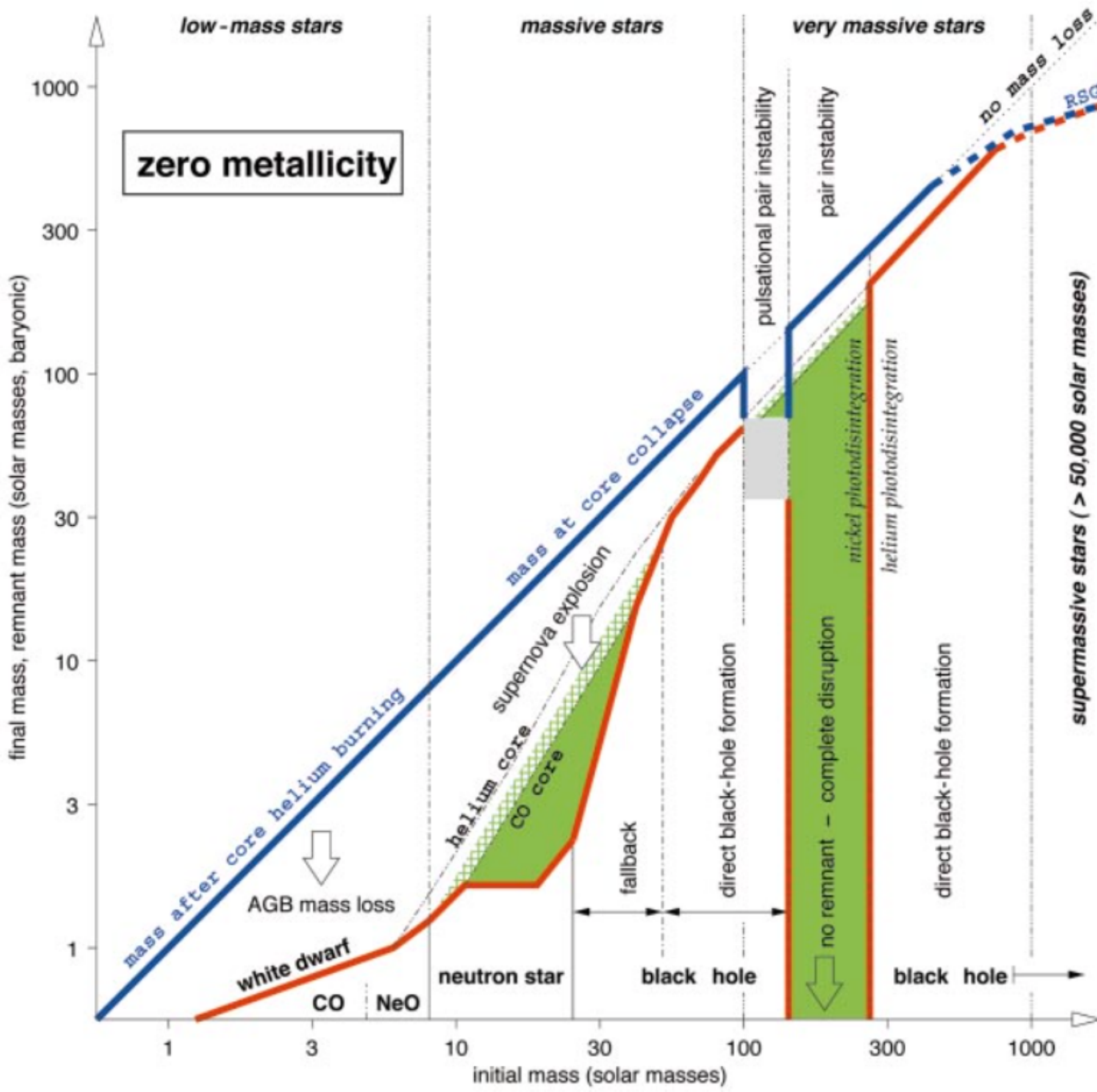
Woosley, Heger, and Weaver: Evolution and explosion of massive stars

TABLE I. (*Continued*).

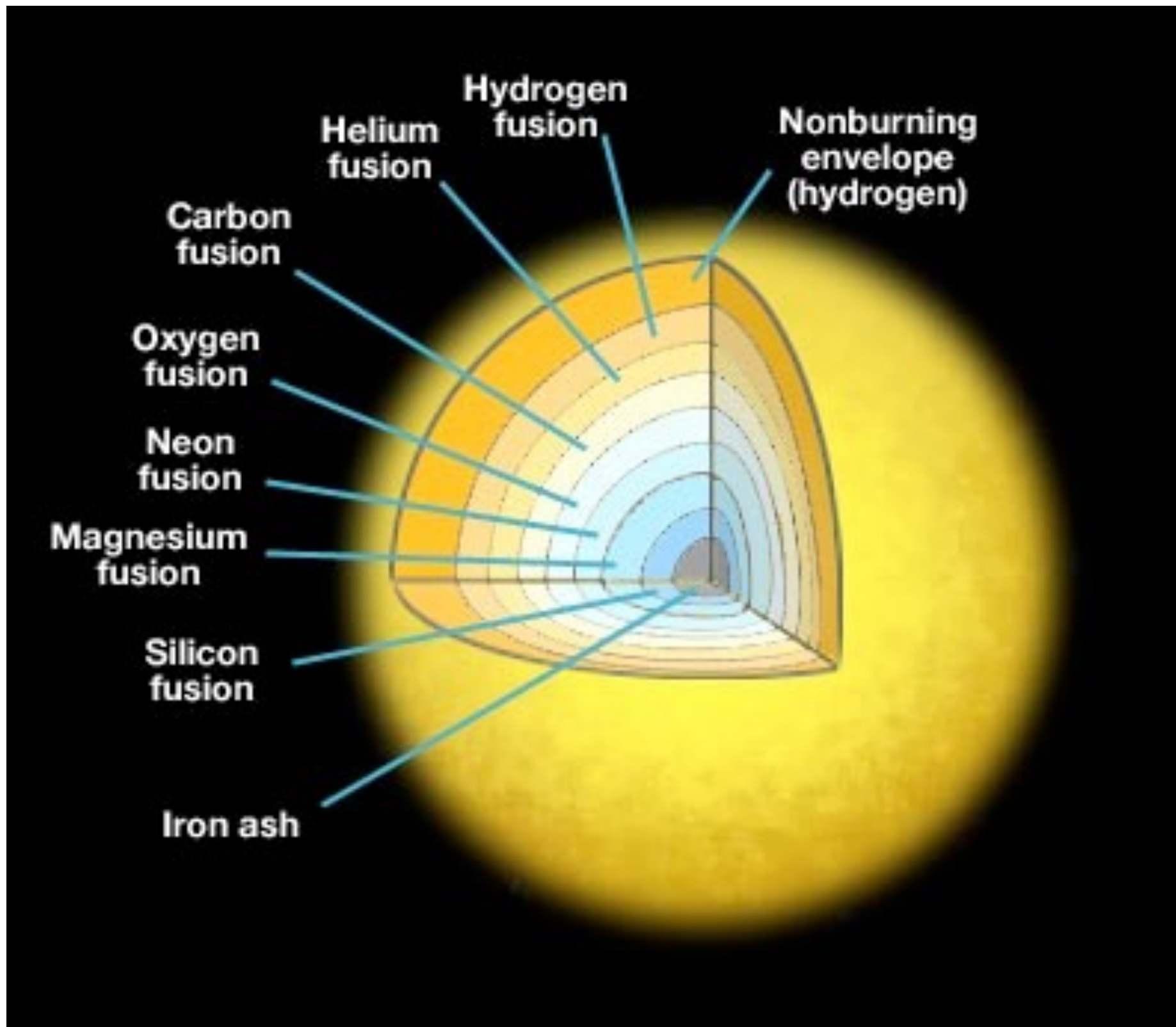
Silicon burning

M_{initial} M_{\odot}	T 10^9 K	ρ 10^7 g cm^{-3}	M M_{\odot}	L $10^3 L_{\odot}$	R R_{\odot}	τ d
13	3.28	4.83	11.4	64.5	692	17.8
15	3.34	4.26	12.6	86.5	821	18.3
20	3.34	4.26	14.7	147	1090	11.5
25	3.65	3.01	12.5	246	1400	0.733
75	3.55	3.73	6.36	173	0.755	2.09
75 ^c	3.82	1.18	74.0	1540	716	0.209





Pre-supernova structure of a massive star



Part III

3D hydro simulations of convection to improve understanding of convection

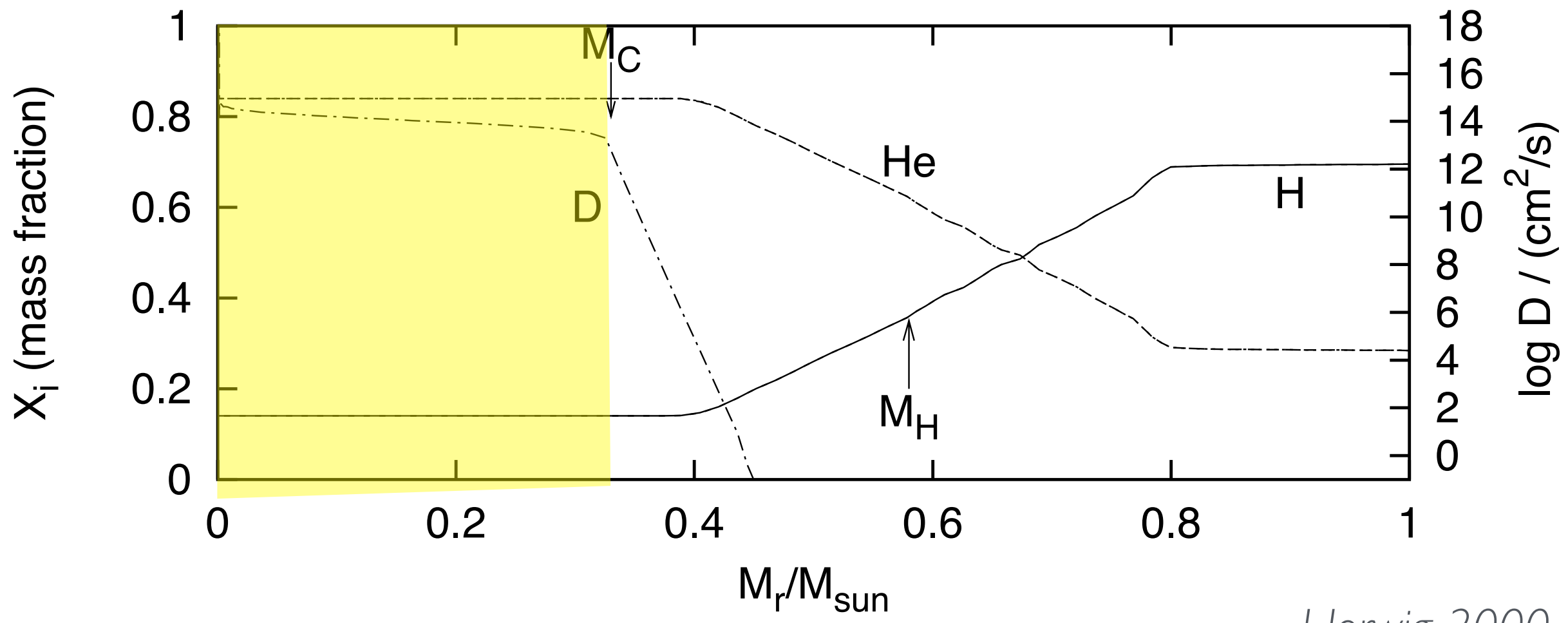
- ▶ Schwarzschild condition for instability against convection

$$\left| \frac{\partial T}{\partial r} \right|_{\text{rad}} > \left| \frac{\partial T}{\partial r} \right|_{\text{conv}}$$

[The gradient are often written in terms of $\nabla \equiv \frac{\partial \ln T}{\partial \ln P}$. Rewrite the above as ∇_{ad} and ∇_{rad} .] That way you deal with the negative sign of dT/dr .

- ▶ 2Msun, main sequence
- ▶ clear observational evidence that convective cores have to be larger than predicted by Schwarzschild condition
- ▶ different types of instabilities
 - buoyancy driven (RT)
 - shear flows (KH)
 - and something else?

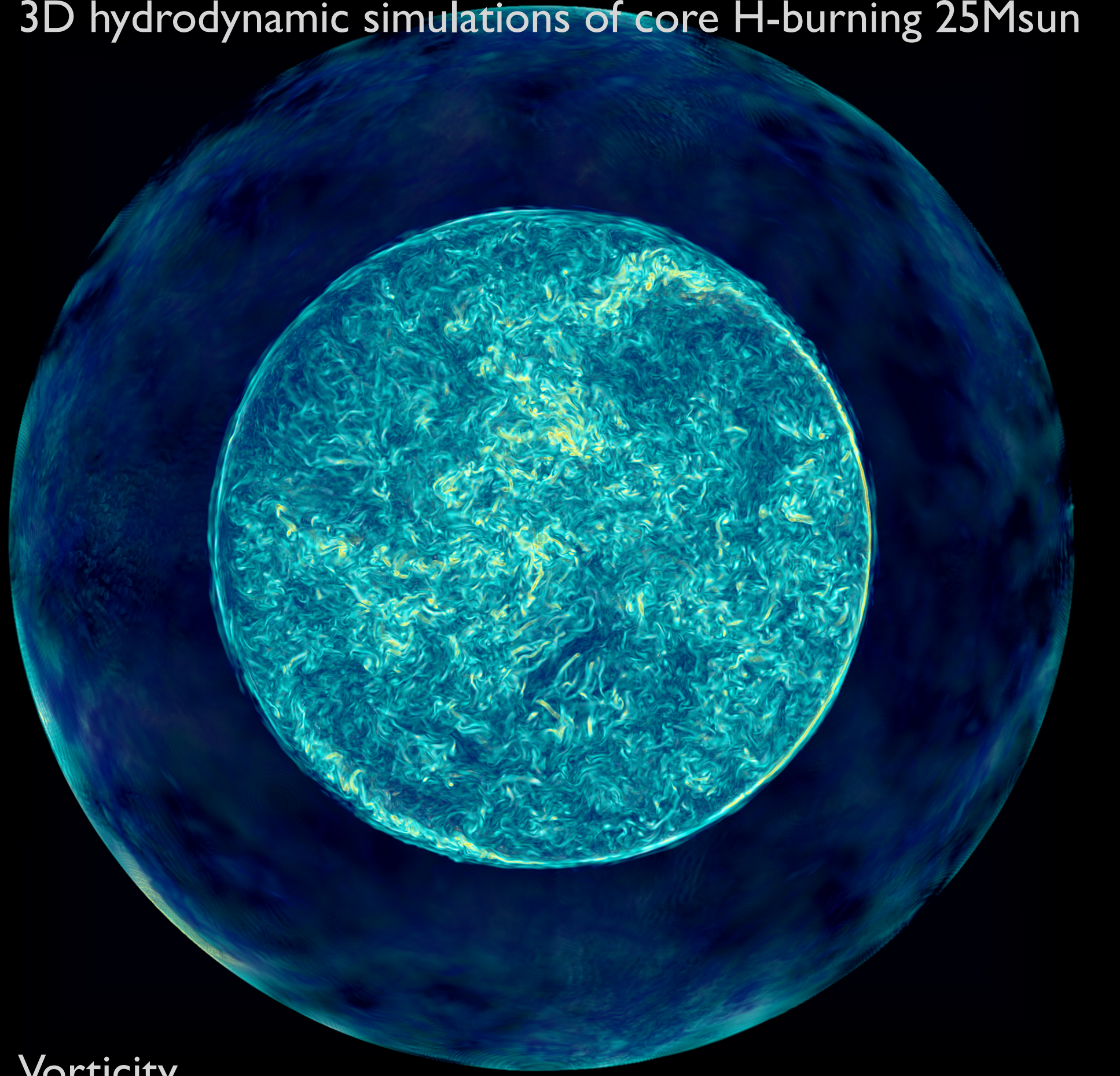
$$D_{\text{OV}} = D_0 \exp\left(\frac{-2z}{H_v}\right), \quad H_v = f \cdot H_p, \quad (2)$$



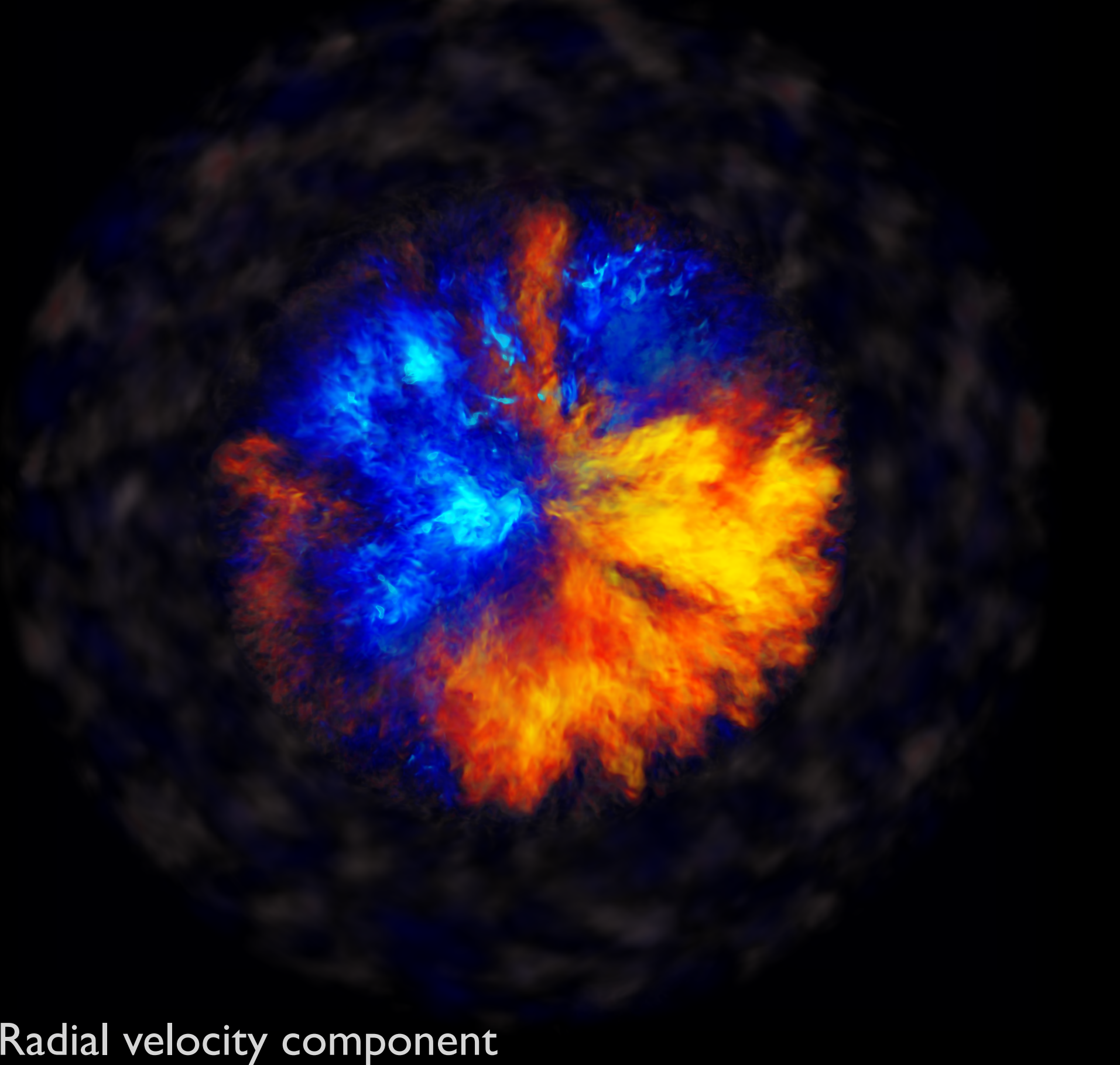
Herwig 2000

3D hydrodynamic simulations of core H-burning 25Msun

63

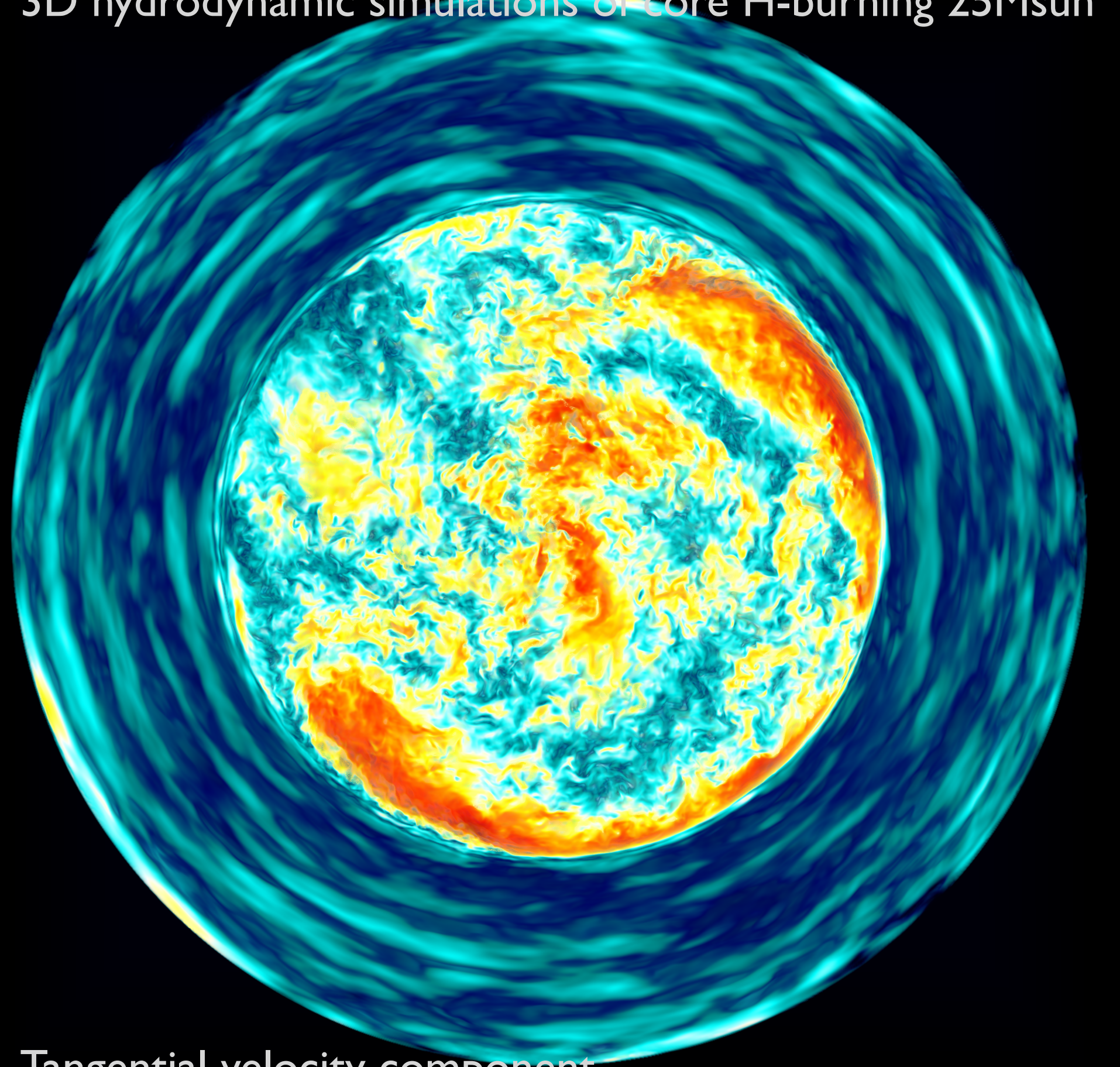


Vorticity

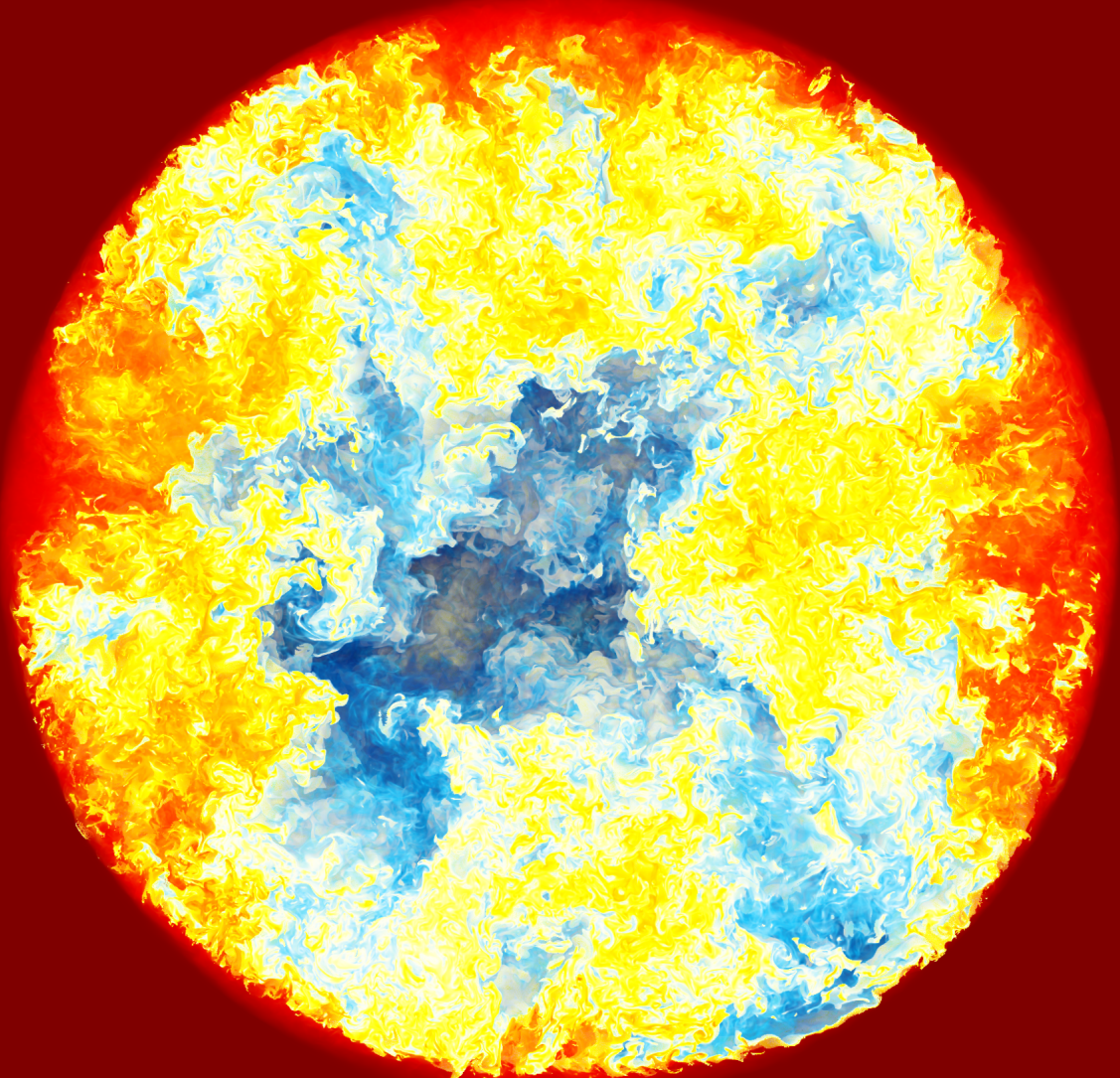


3D hydrodynamic simulations of core H-burning 25Msun

65



Tangential velocity component



Fractional volume (abundance) of material initially outside convection zone

Determine convective boundary parameter f_{CBM}

67

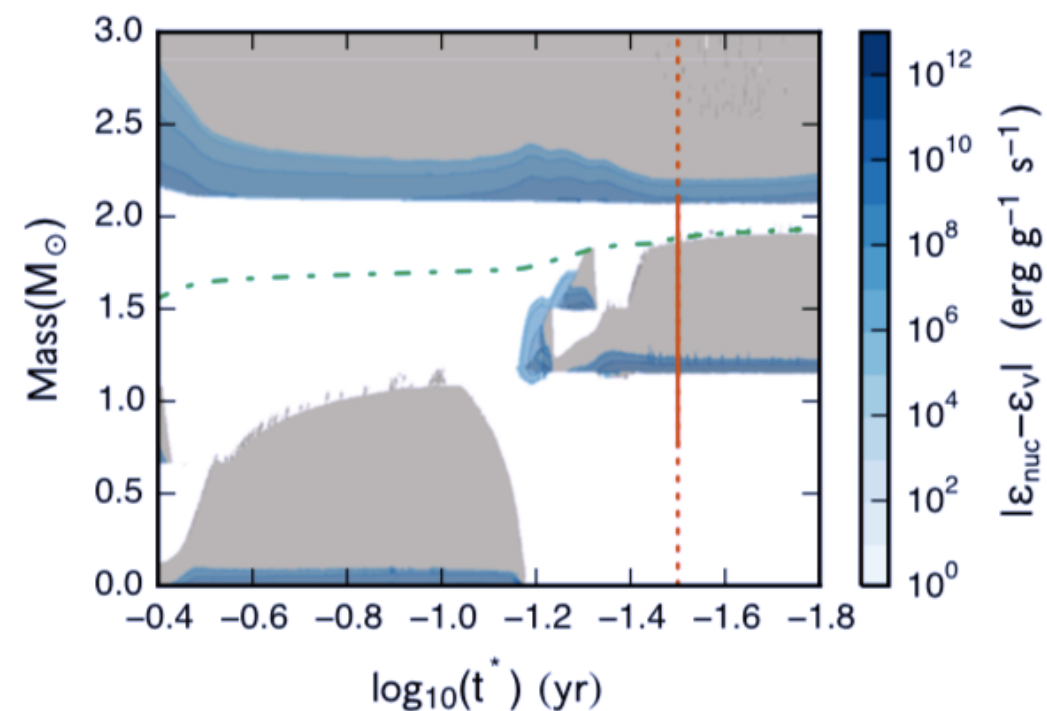
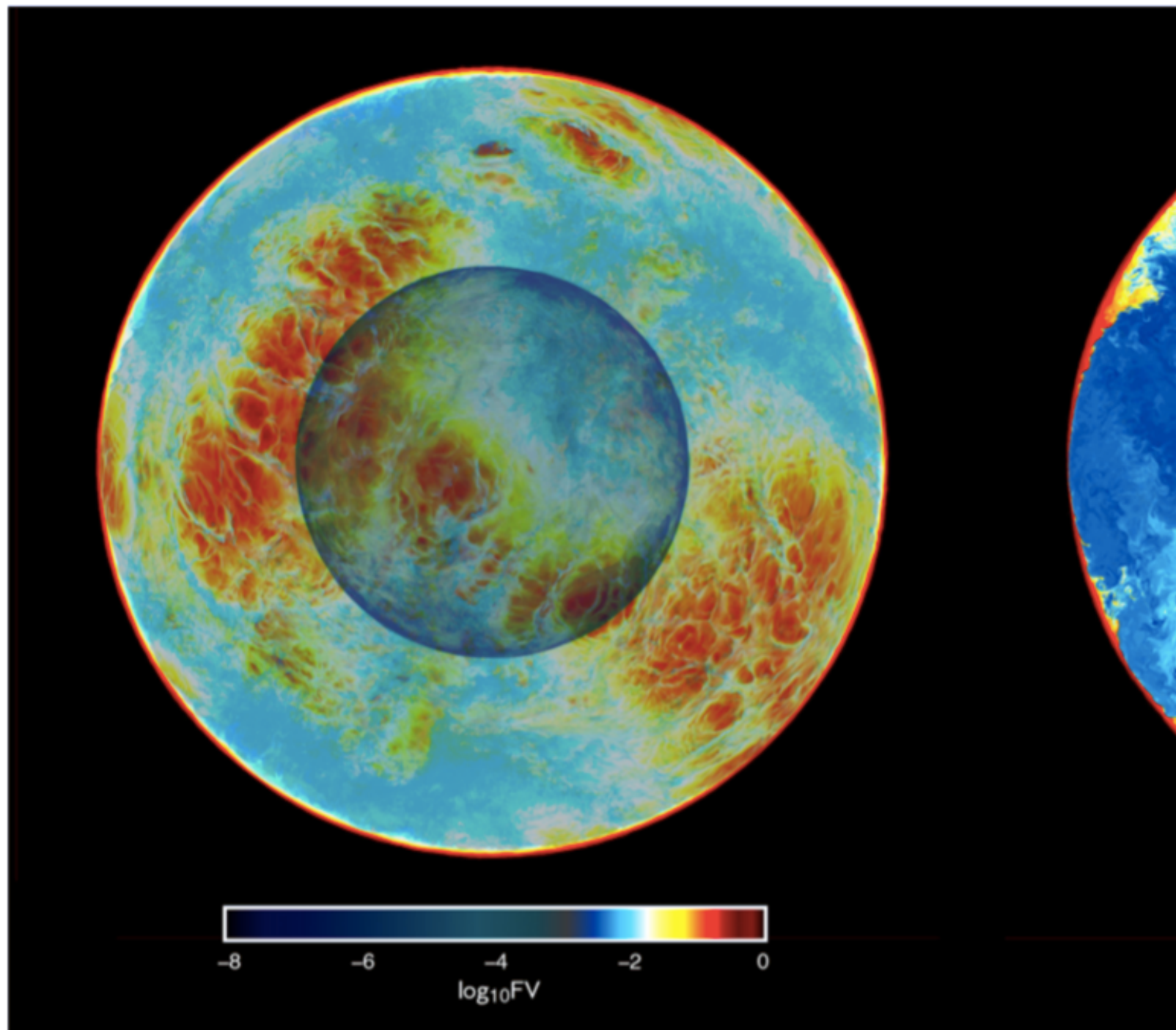
... in progress for core convection ...

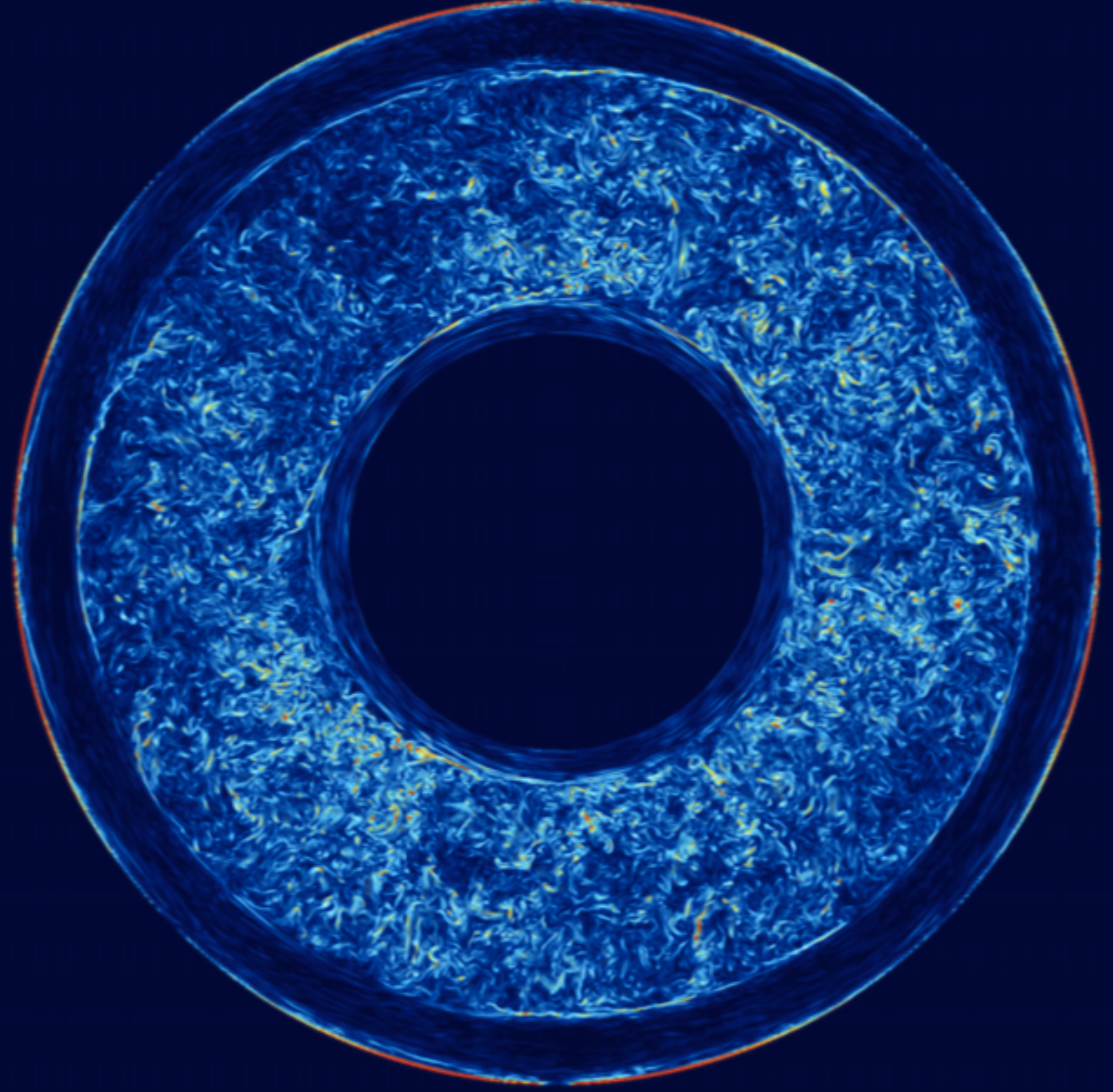
Determine convective boundary parameter

f_{CBM} O-shell burning convection zone in $25M_{\odot}$,

$Z=0.02$ stellar model

Jones+ / 7

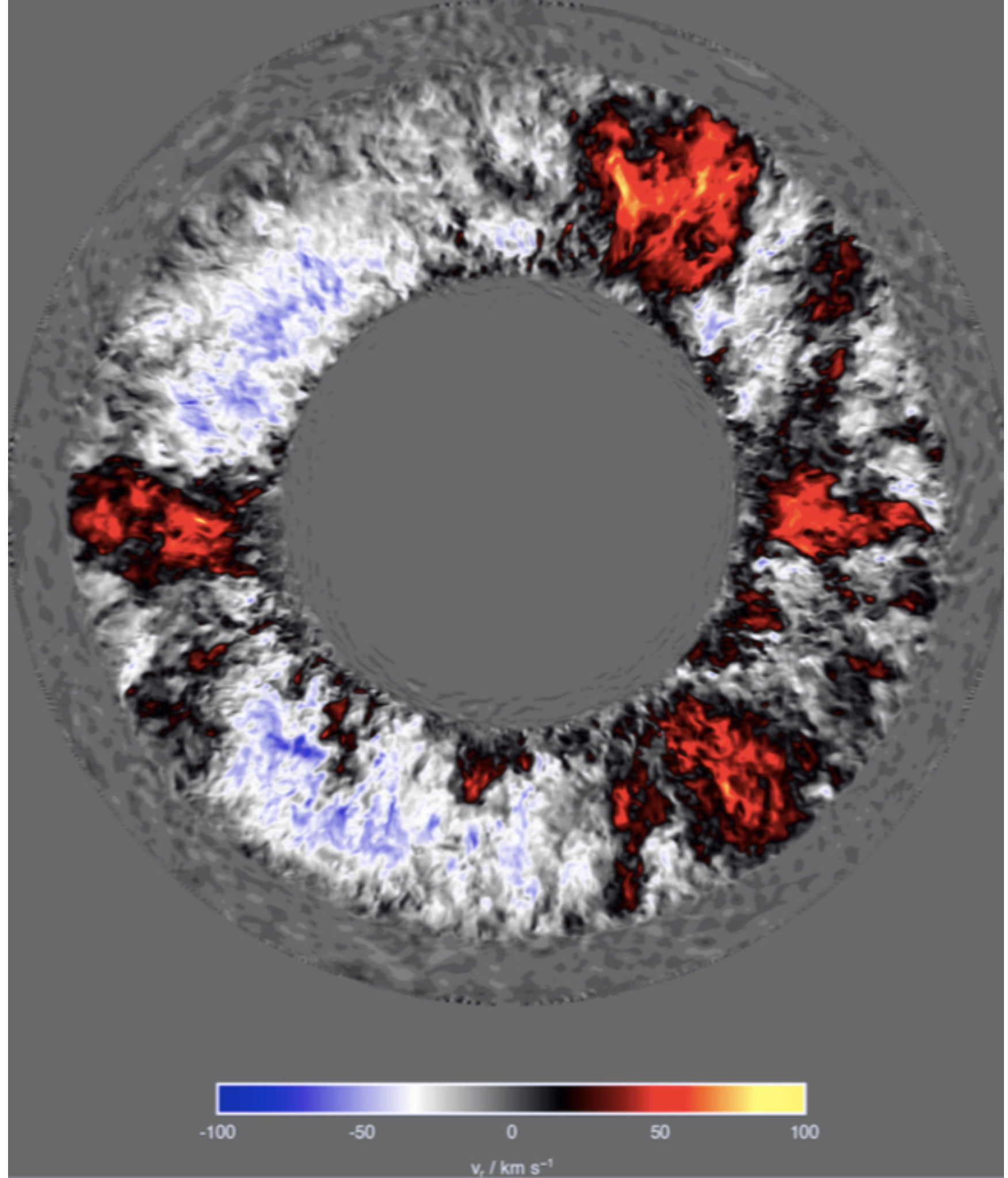




Vorticity



Radial velocity



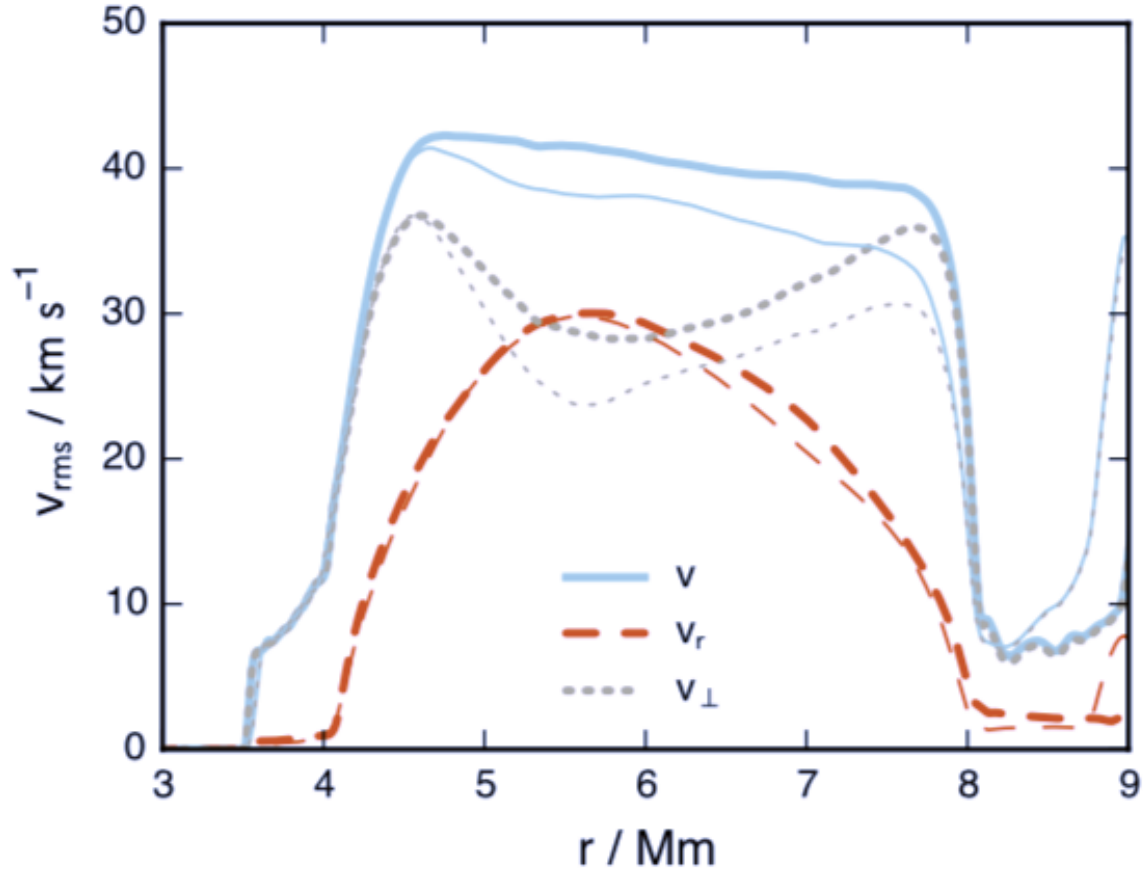


Figure 11. Spherically averaged total, radial and tangential fluid velocity components after 22 min of simulated time (dump number 132) in the d2 (thick lines) and d1 (thin lines) simulations (see Table 1).

Velocity profiles

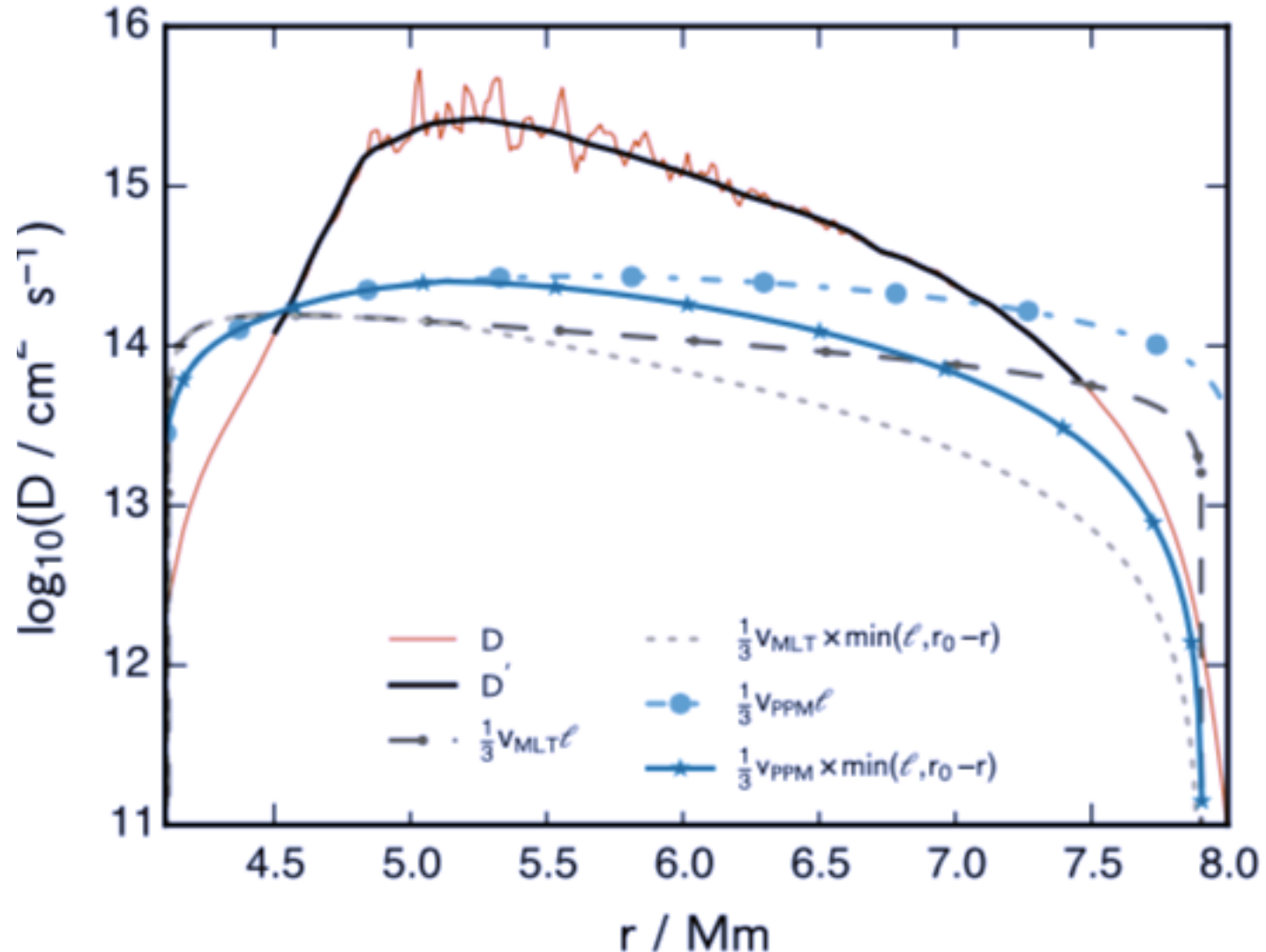


Figure 21. Time-averaged radial diffusion coefficient profile calculated from the spherically averaged abundance profiles by the method described in Section 3.5 (brown solid line; black solid line is a fit to the noisy region). The convective velocities computing using MLT agree with the spherically averaged 3D velocities to within about a factor of 2 inside the convection zone but are too large in the vicinity of the CB, resulting in an overestimation of the diffusion coefficient there. Limiting the mixing length to the distance from the CB reproduces the fall-off of the diffusion coefficient inside the convection zone approaching the boundary which is seen in the spherically averaged 3D simulation results.

D profiles

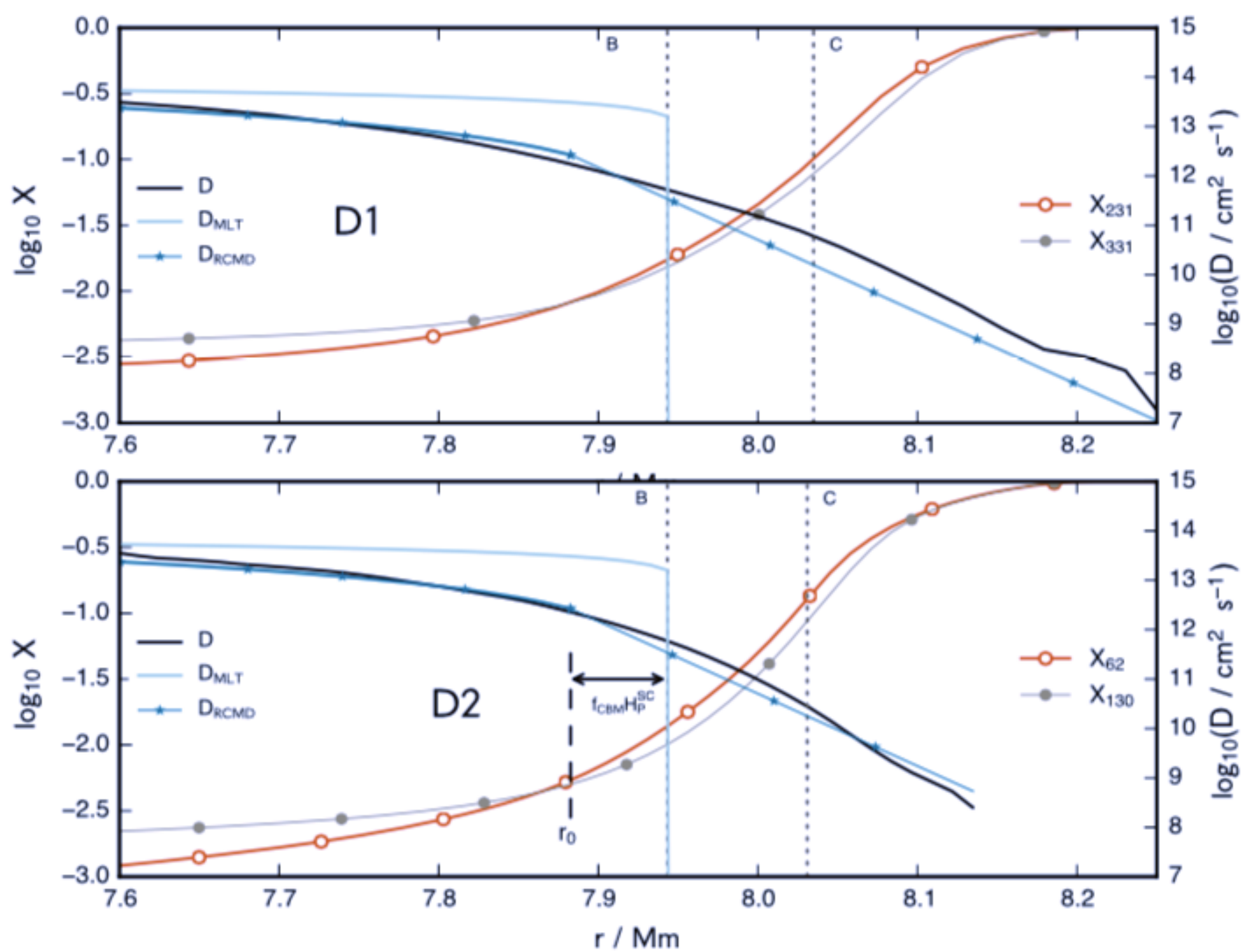


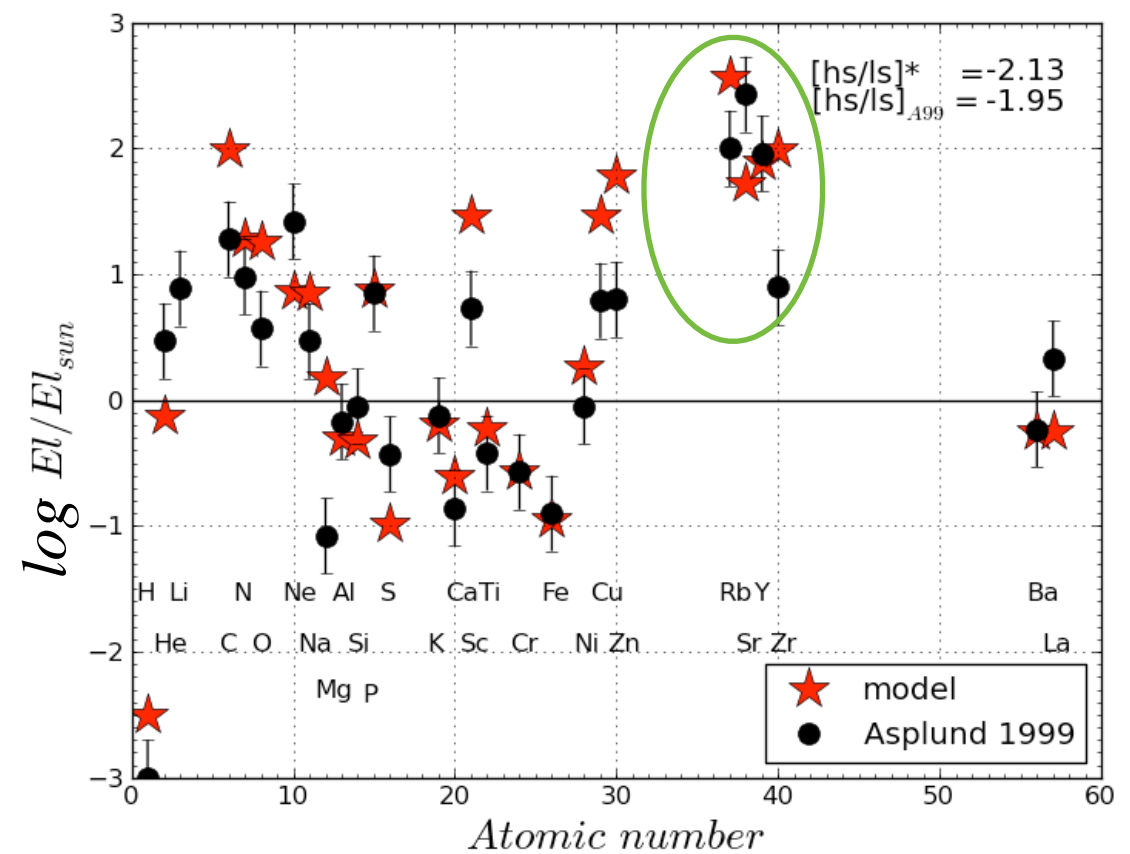
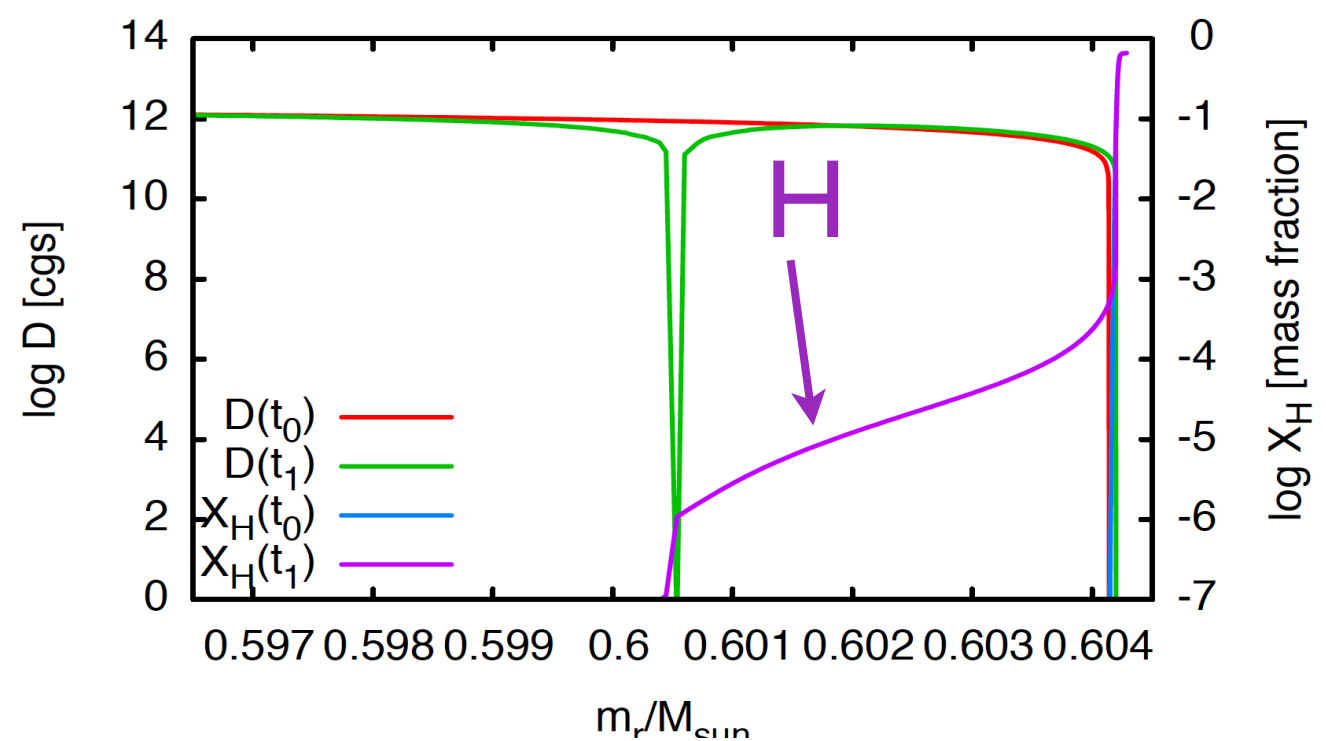
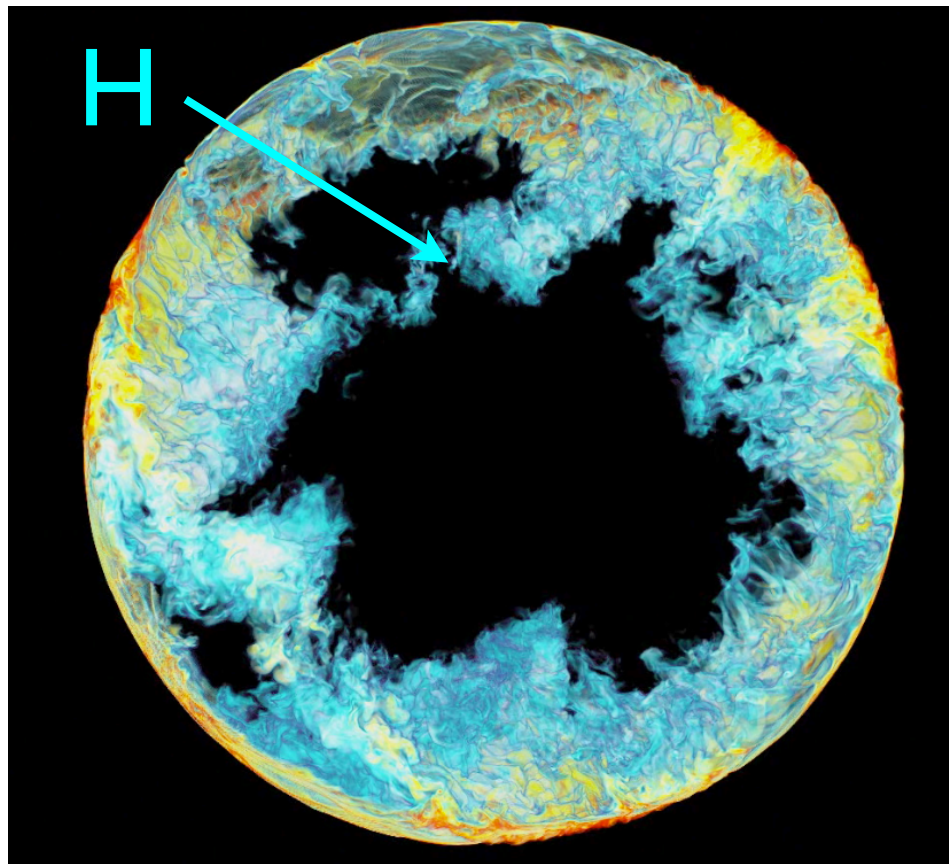
Figure 22. Results of the 3D–1D diffusion analysis at the upper CB of the d1 (768^3 grid) and d2 (1536^3 grid) simulations (see Table 1). The vertical dotted lines represent the upper boundary of the convection zone. B is where the entropy gradient becomes positive in our PPMSTAR setup (equivalent to the Schwarzschild criterion); C is where the radial gradient of the tangential component of the fluid velocity is steepest after 46.7 (16.0) min of simulated time for simulation d1 (d2). We also give the MESA model upon which these simulations were based; it has been aligned so that the CB according to the Schwarzschild criterion is located at B. X is the spherically averaged mass fraction of the overlying fluid and is plotted at a simulated time indicated by the subscript in tens of seconds. $D_{\text{MLT}} = \frac{1}{3} v_{\text{MLT}} \alpha H_P$ is the diffusion coefficient computed in the framework of MLT with $\alpha = 1.6$. D (solid black line) is the derived diffusion coefficient which gives the same net mixing as the 3D hydrodynamic simulation when its output is spherically averaged. D_{RCMD} is the recommended diffusion coefficient to use in a 1D code given by $D_{\text{RCMD}} = v_{\text{MLT}} \times \min(\alpha H_P, |r - r_{\text{SC}}|)$, where r_{SC} is the radial coordinate of the Schwarzschild boundary at B, as described in Section 3.6 of the text, with an exponentially decaying CB mixing from radius $r_0 = r_{\text{SC}} - f_{\text{CBM}} H_P$ with $f_{\text{CBM}} = 0.03$, as formulated by Freytag et al. (1996, see Section 3.6).

Part IV

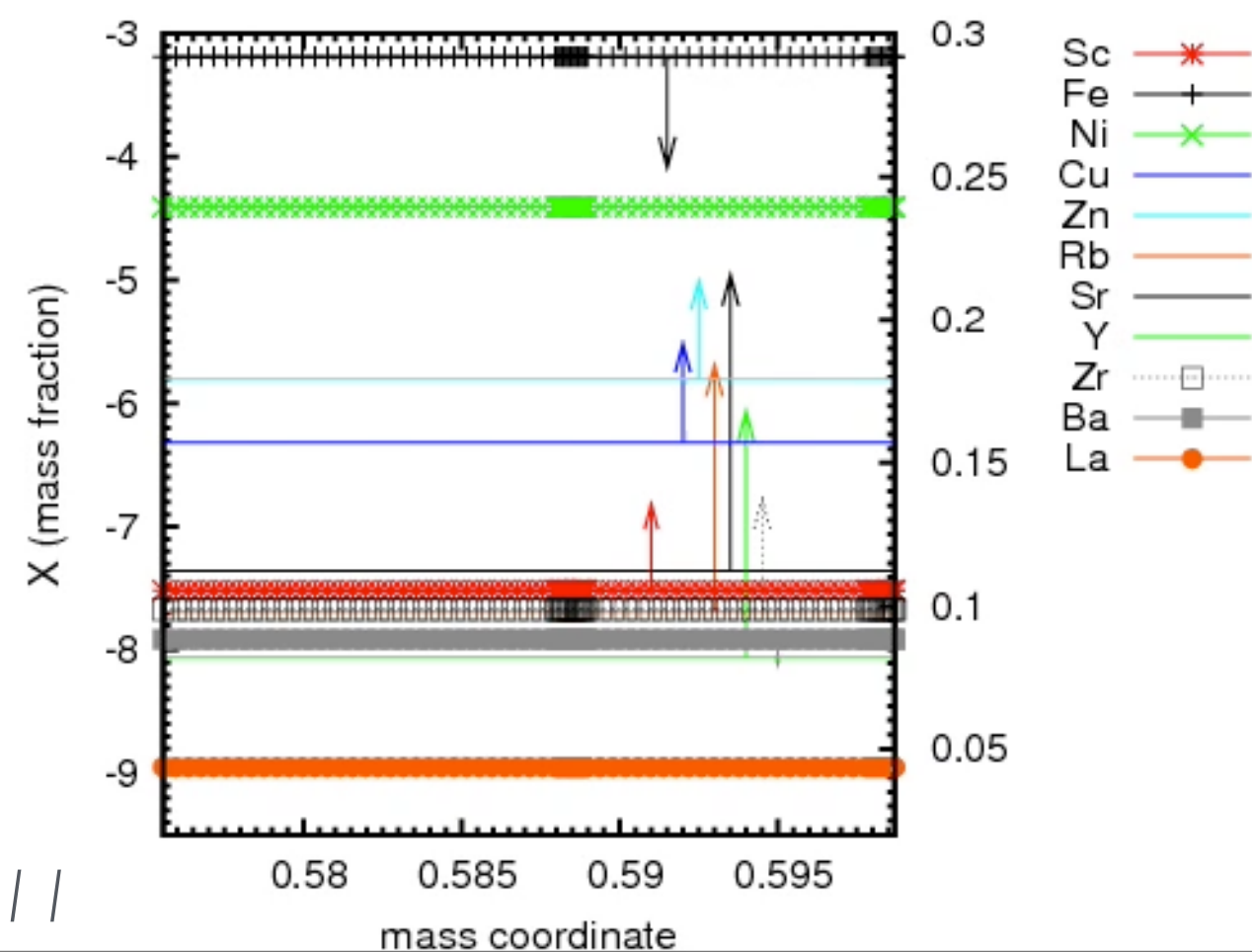
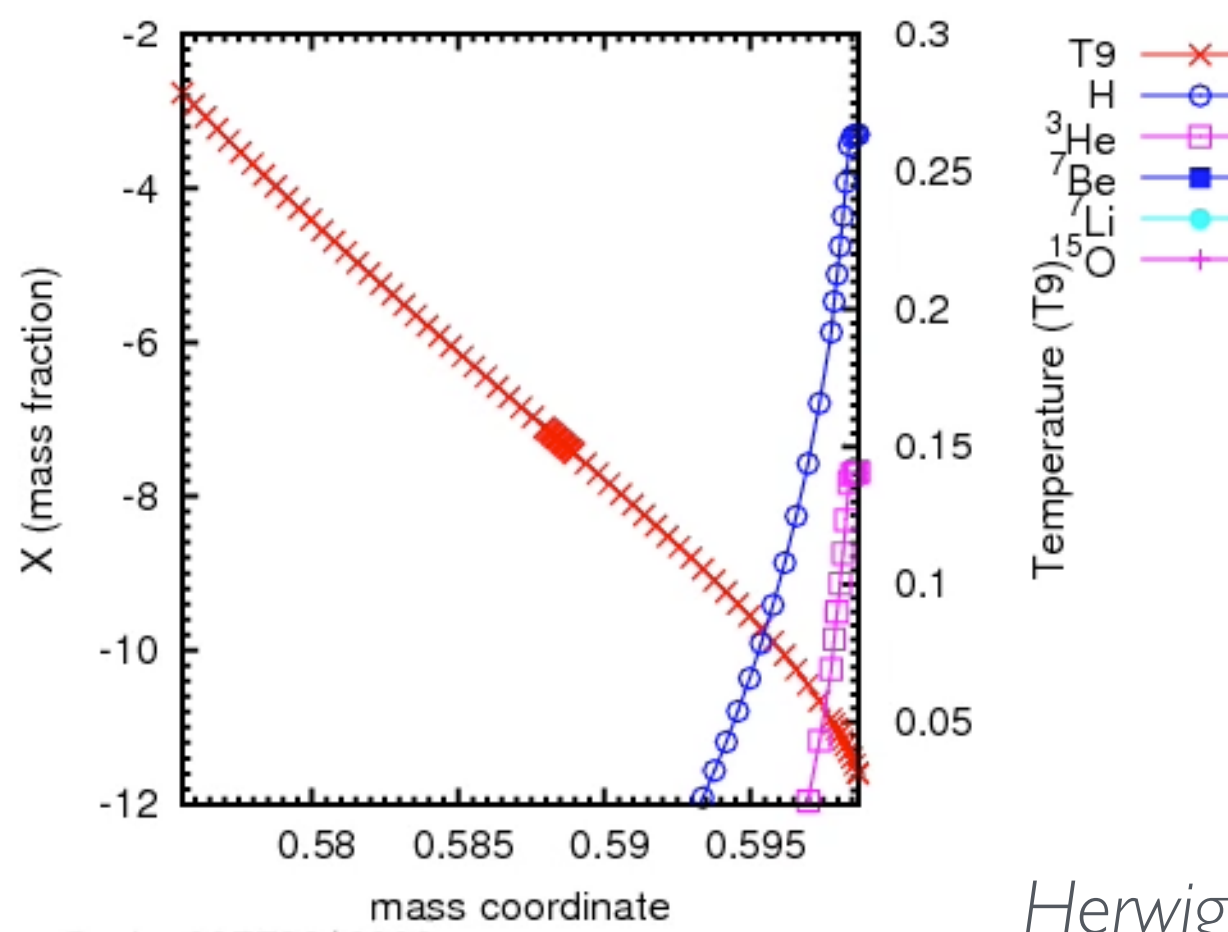
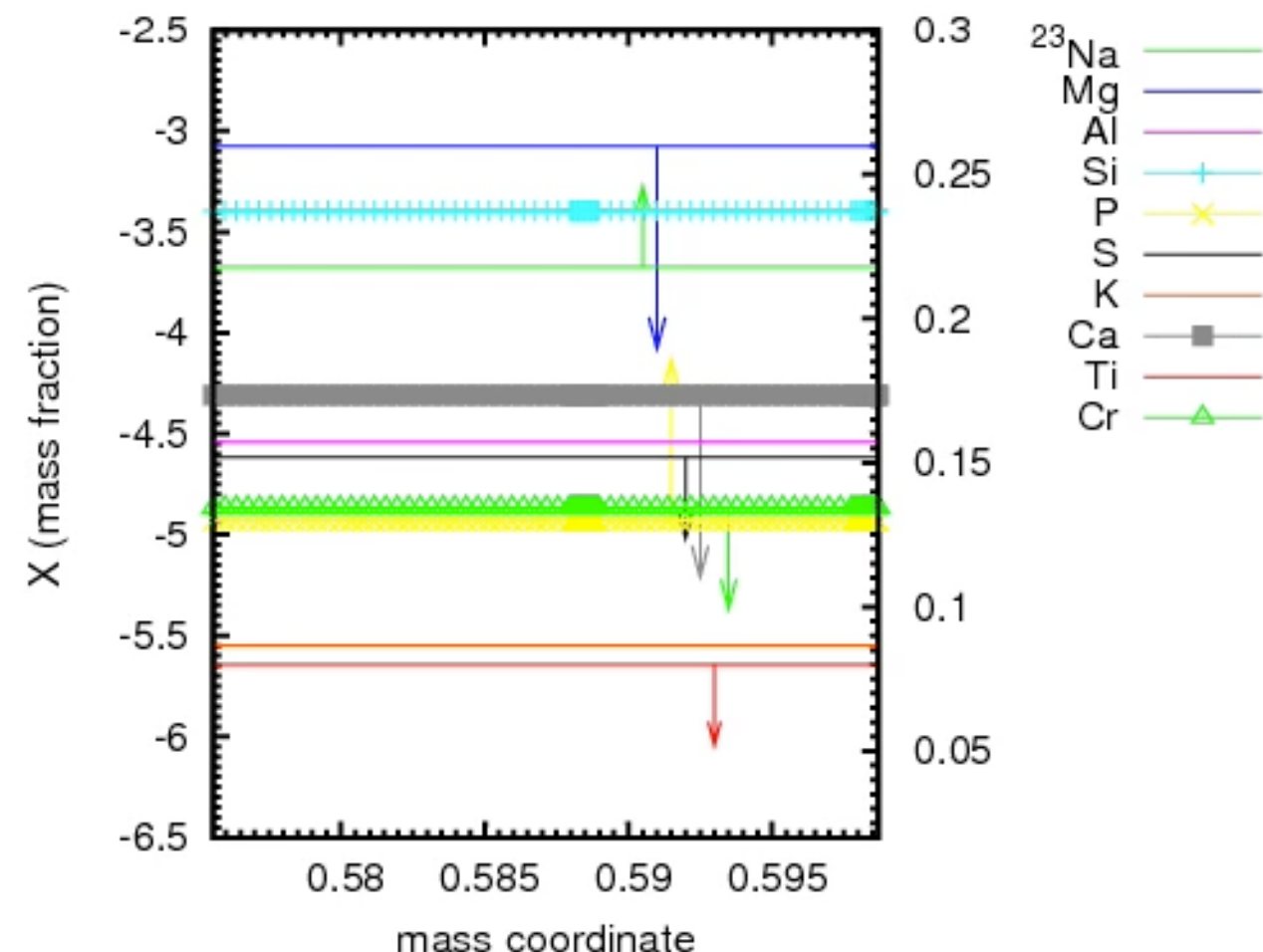
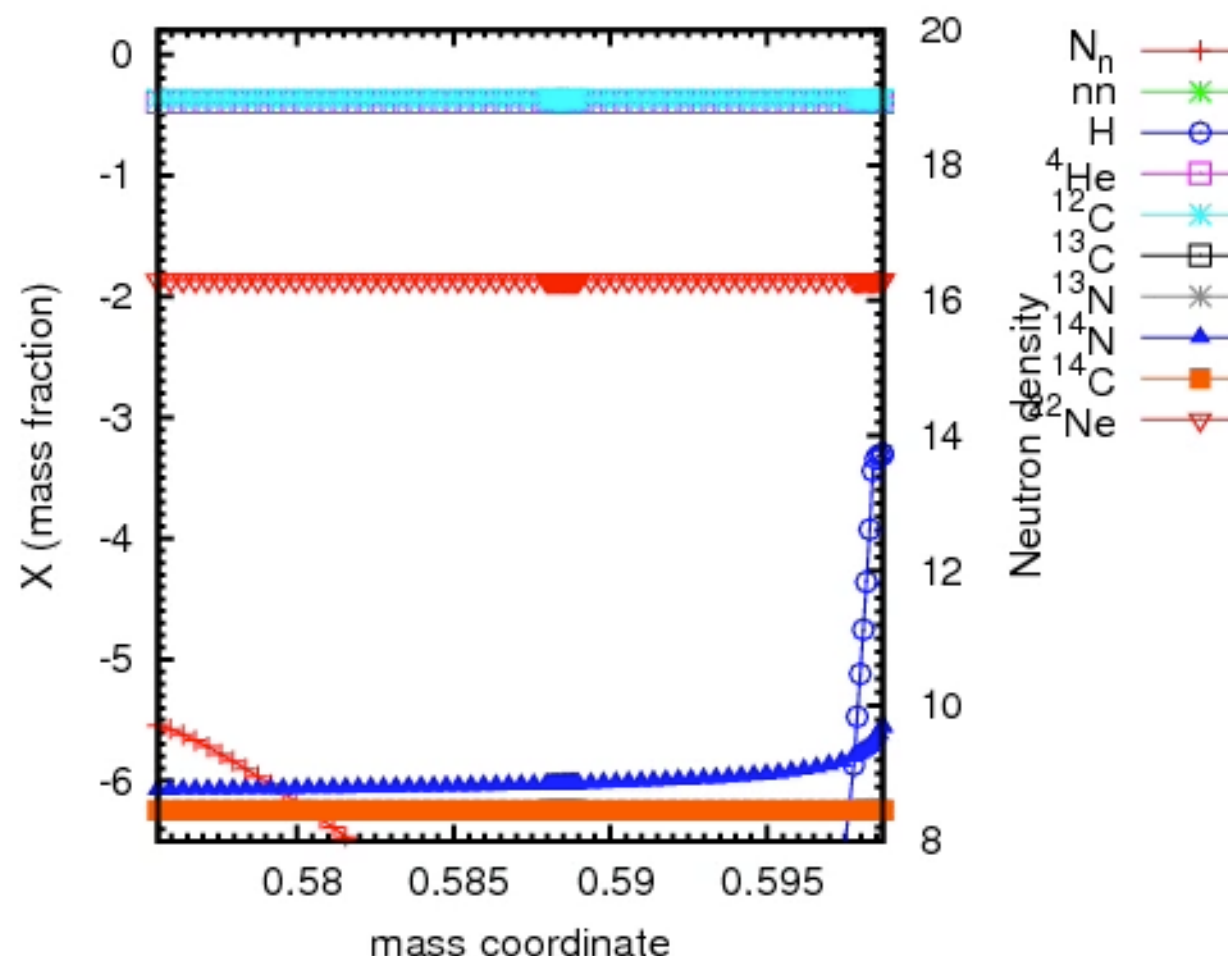
Convective reactive nucleosynthesis

Simultaneous mixing and nucleosynthesis is required to explain the observed abundances

- highly anomalous heavy-element signature, not known from “normal” s process in post-AGB star Sakurai’s object
- unmodified stellar evolution models fail to account for this fingerprint of H-ingestion flash

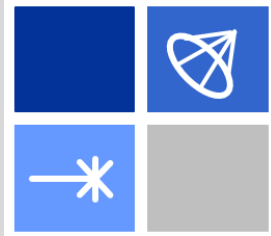


Herwig+ '11



Cycle=00779910000.

Herwig+ //

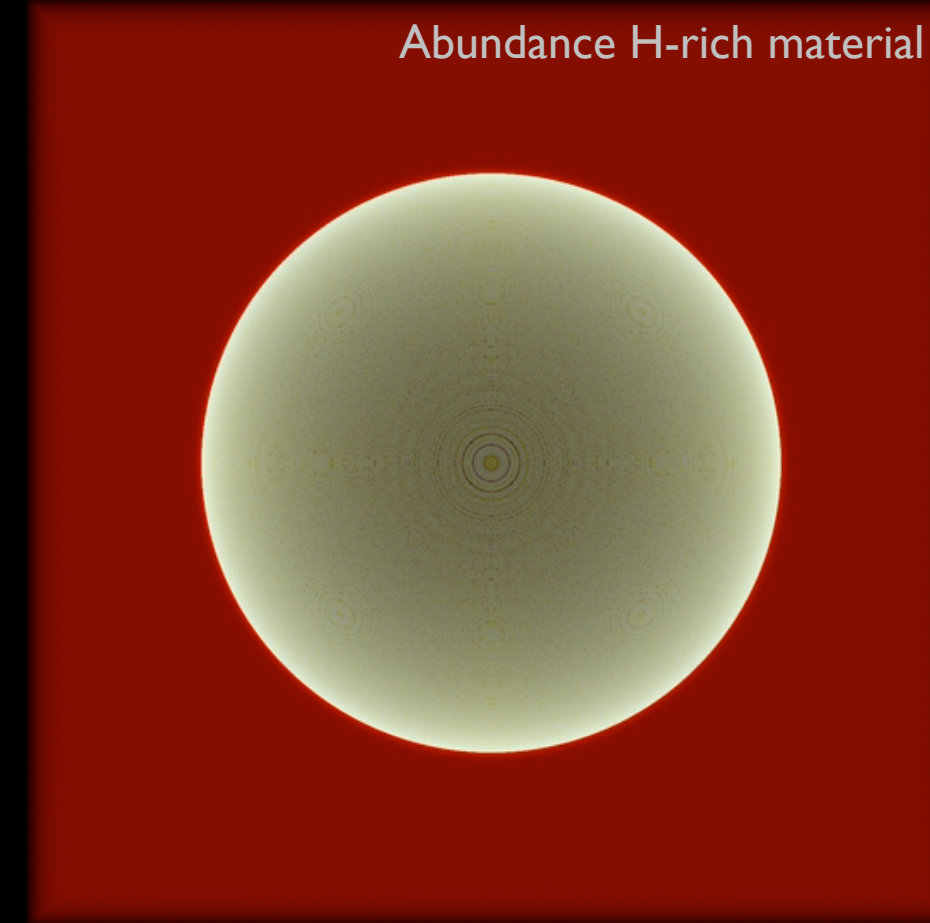


3DID hydro-nucleosynthesis simulations of iRAWD

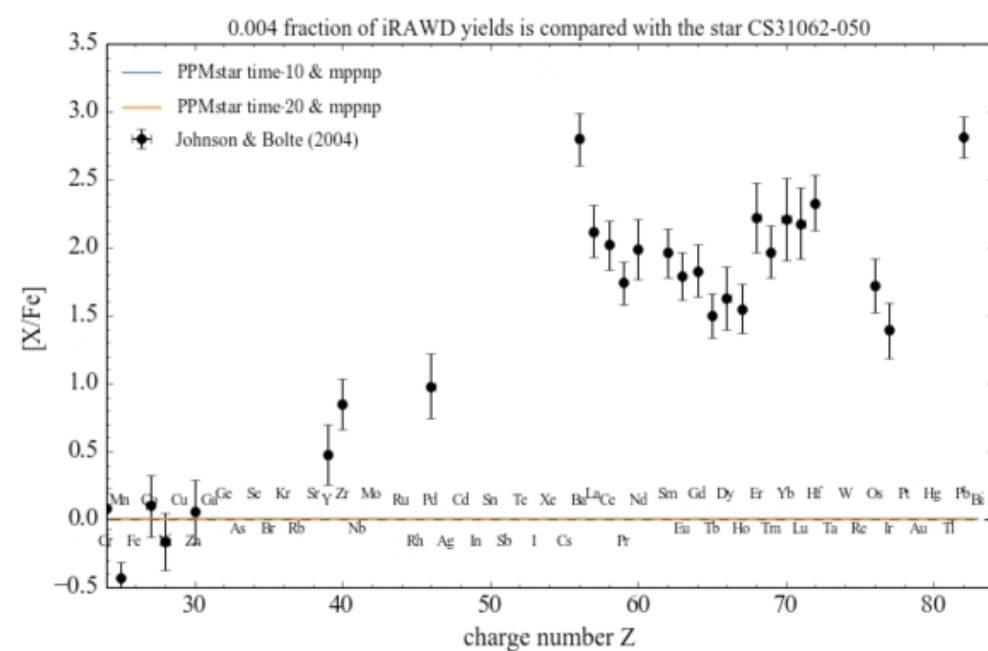
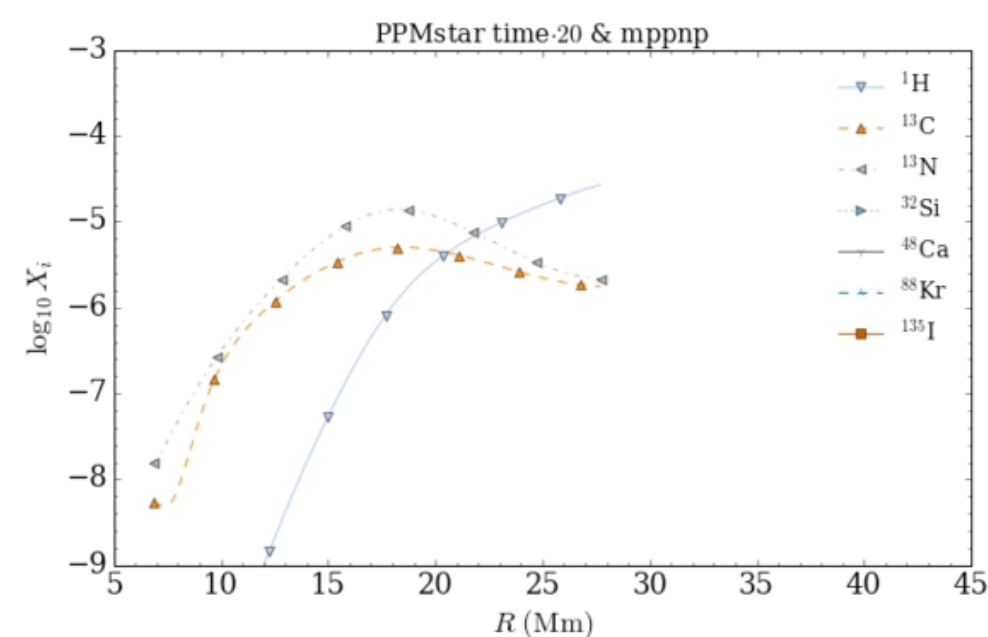
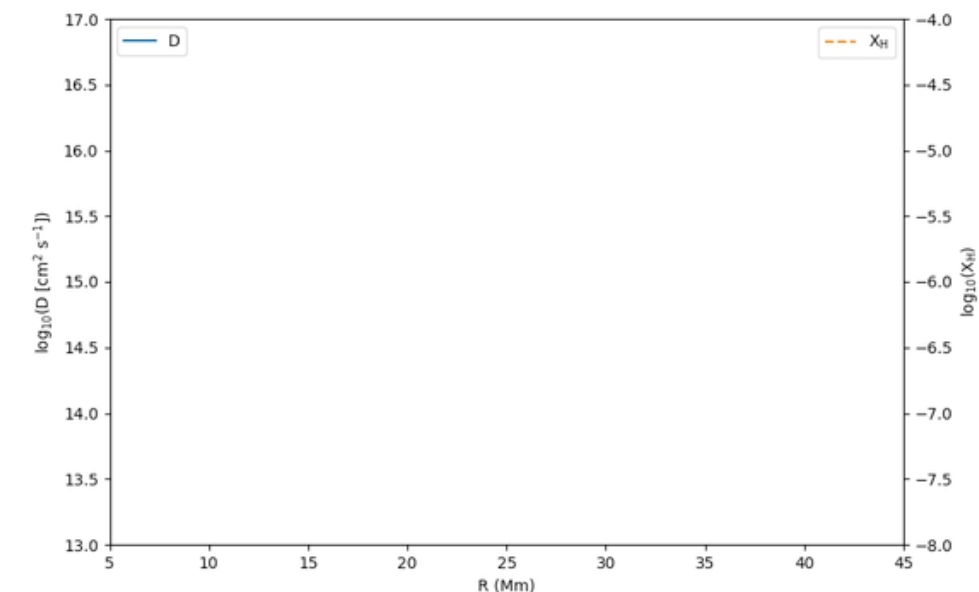
Left panels: 768^3 -grid simulation of H-ingestion in RAWD

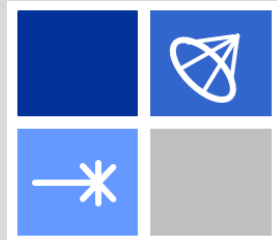
Right (top to bottom):

- 1D diffusion coefficient determined from spherical averaged abundance profile from 3D simulations
- abundance profiles of H, ^{13}C and unstable i-process isotopes from multi-zone 1D post-processing of evolving hydro stratification
- abundance distribution compared to CEMP-i star observation
- [time stretched in post-process to compensate for shorter hydro simulation]



Radial velocity

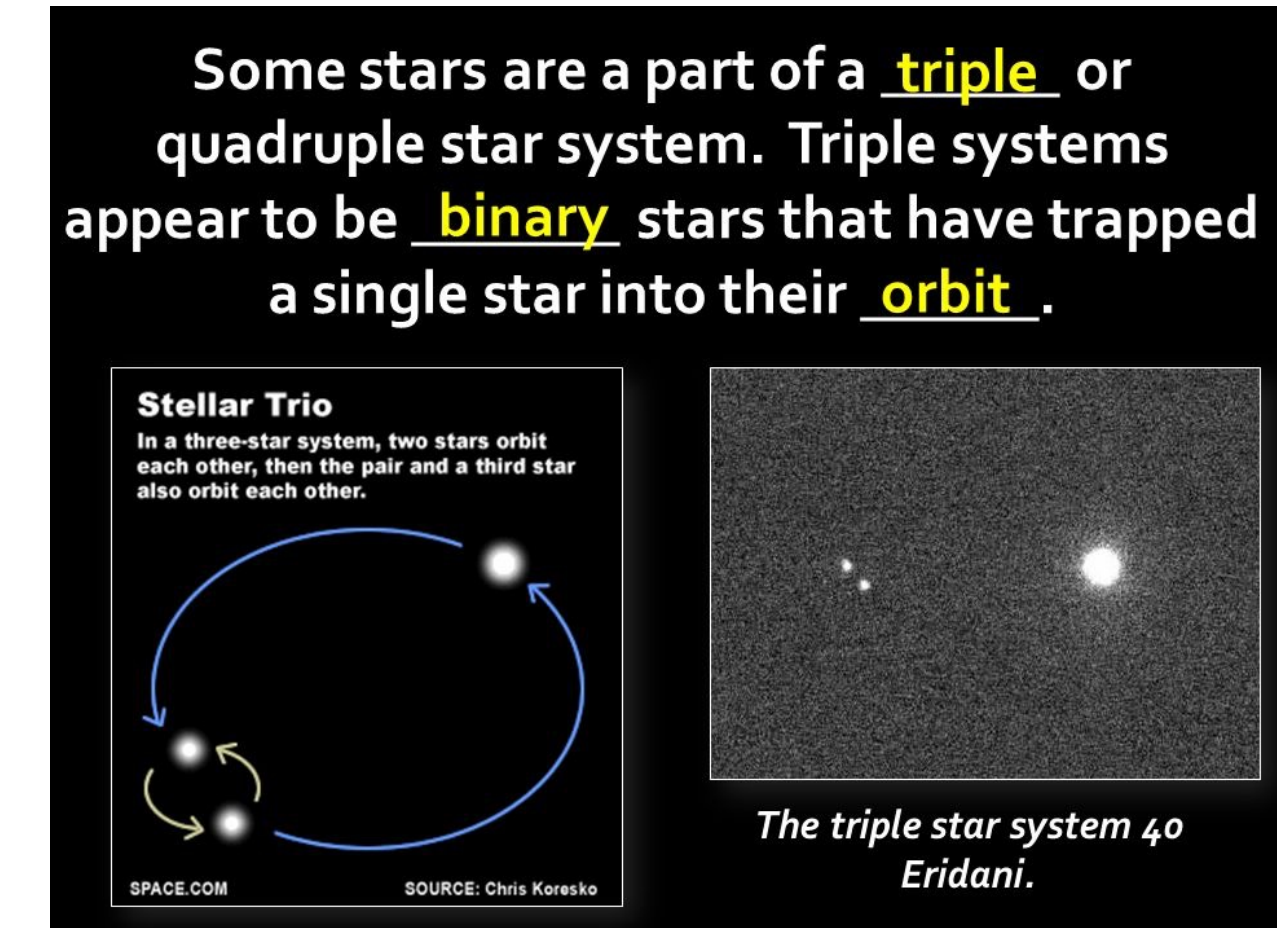
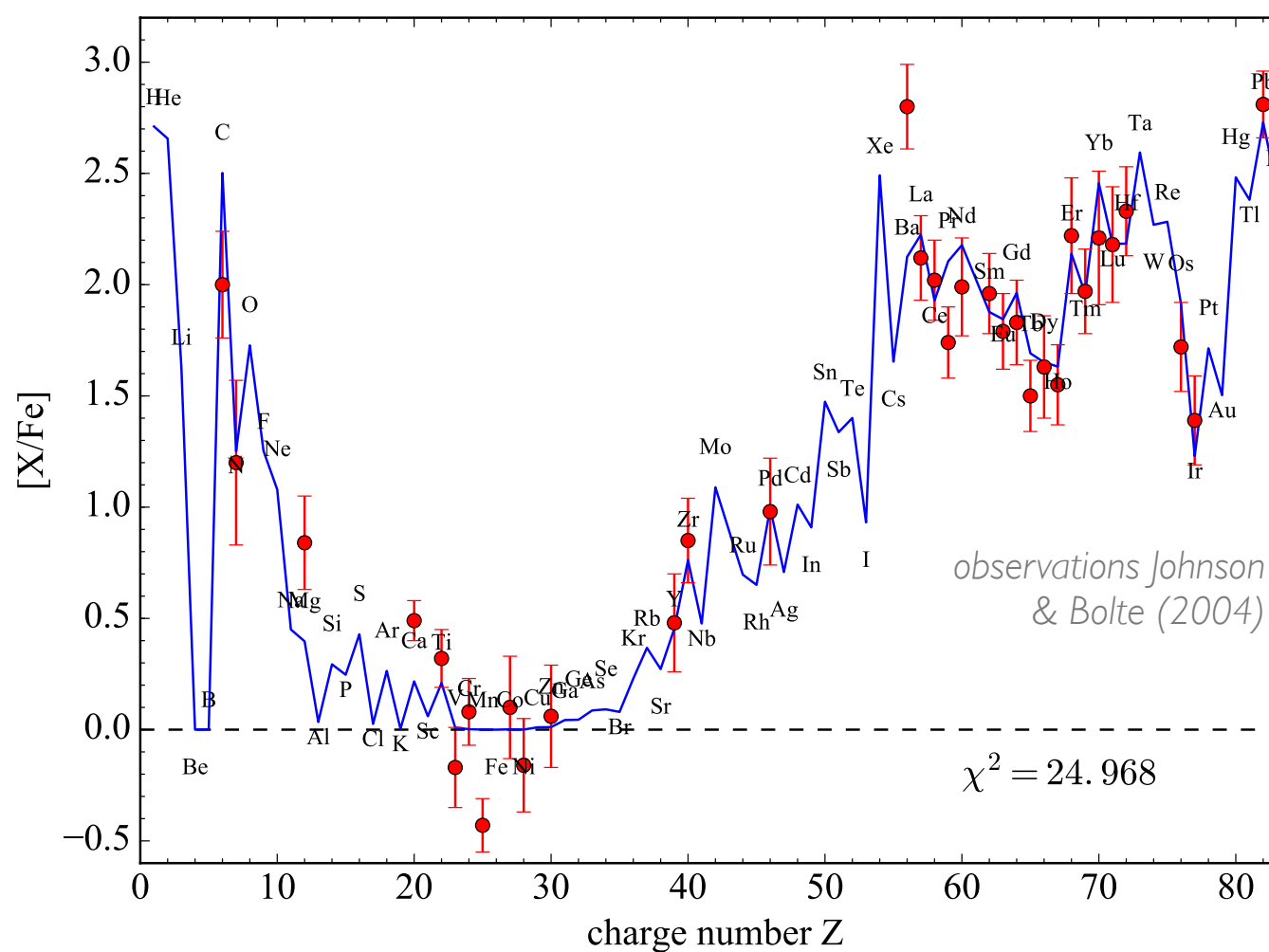




i process in low-Z RAWD - origin of CEMP-i stars?

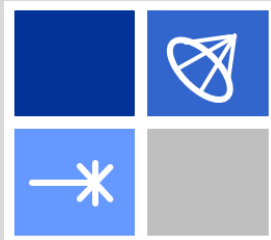
We propose the first simulation based formation scenario for CEMP-i stars. The i-process nucleosynthesis can explain the abundances of heavy elements observed in the CEMP-i star CS31062-050 if in the past it had been a distant companion of a close binary system with a RAWD that exploded as a SN Ia, and, as a result, the star CS31062-050 left the triple system.

Low-Z iRAWD multi-zone simulation

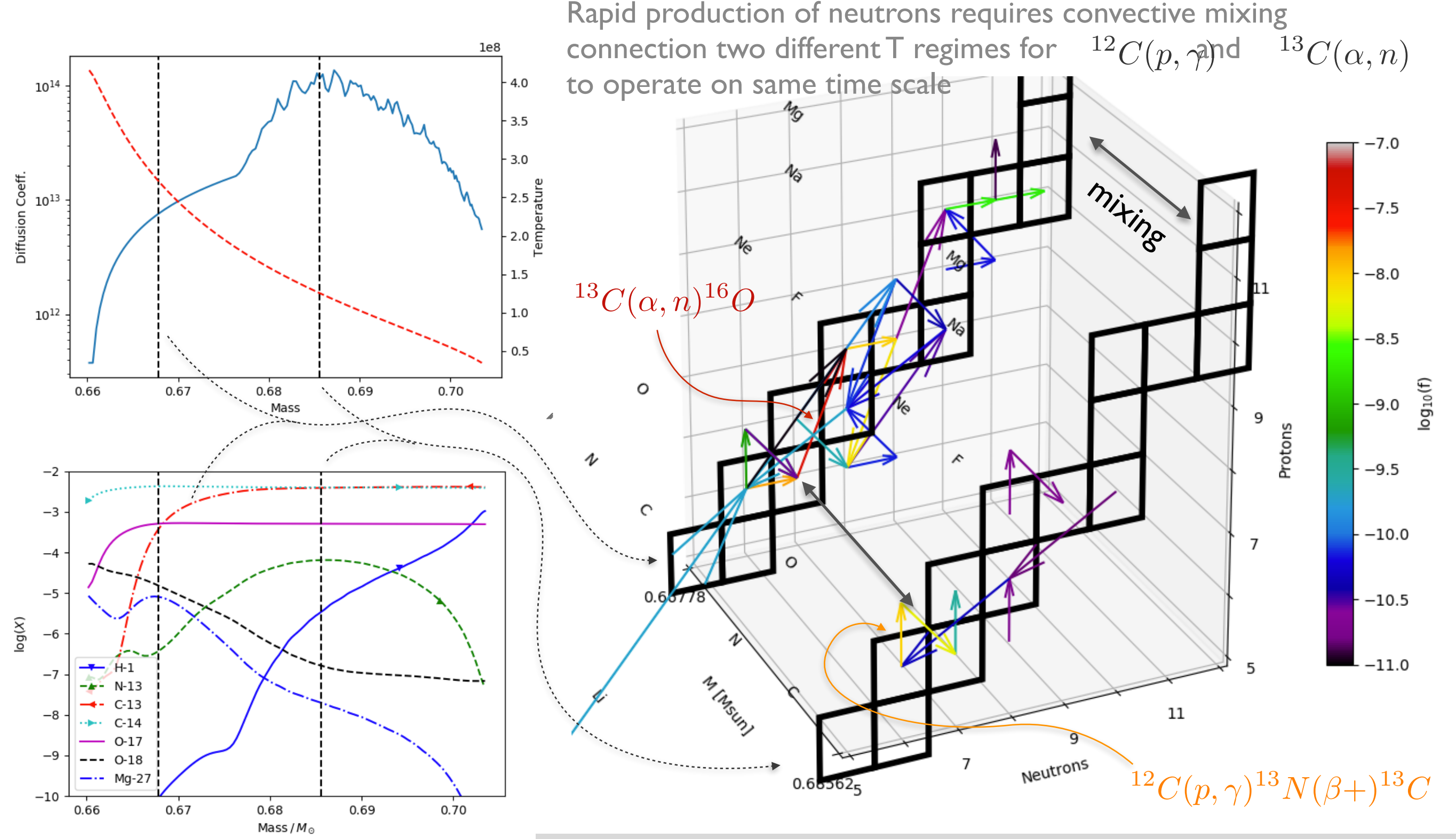


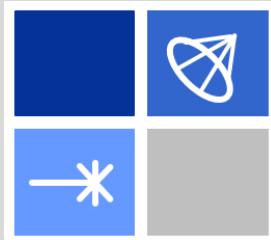
JINA-CEE

NSF Physics Frontiers Center

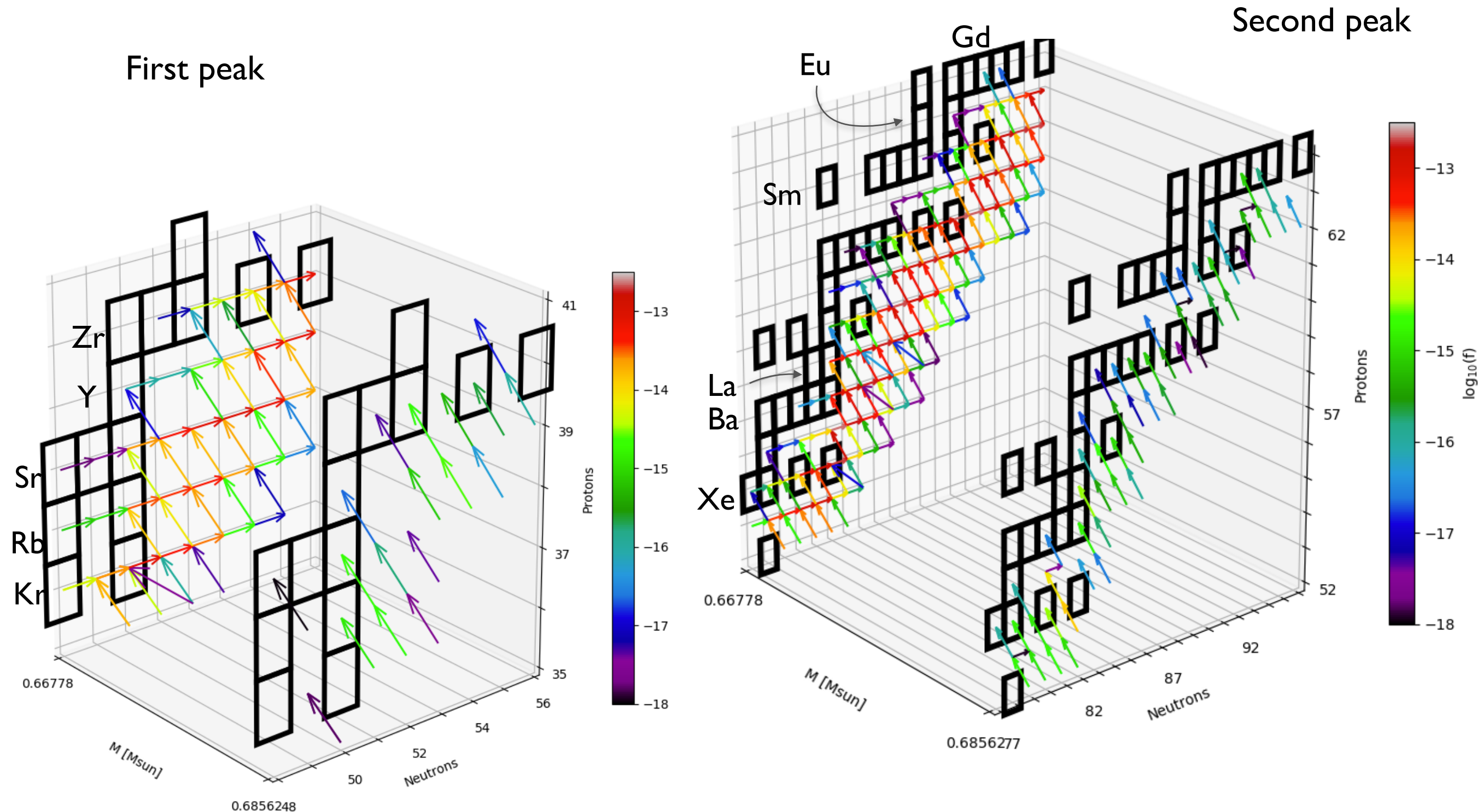


Network flux of convective-reactive i-process nucleosynthesis

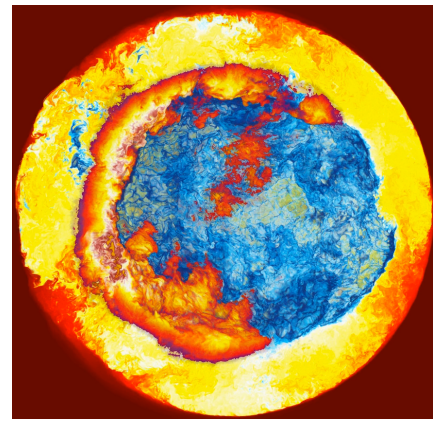




Flux plots of convective-reactive nucleosynthesis



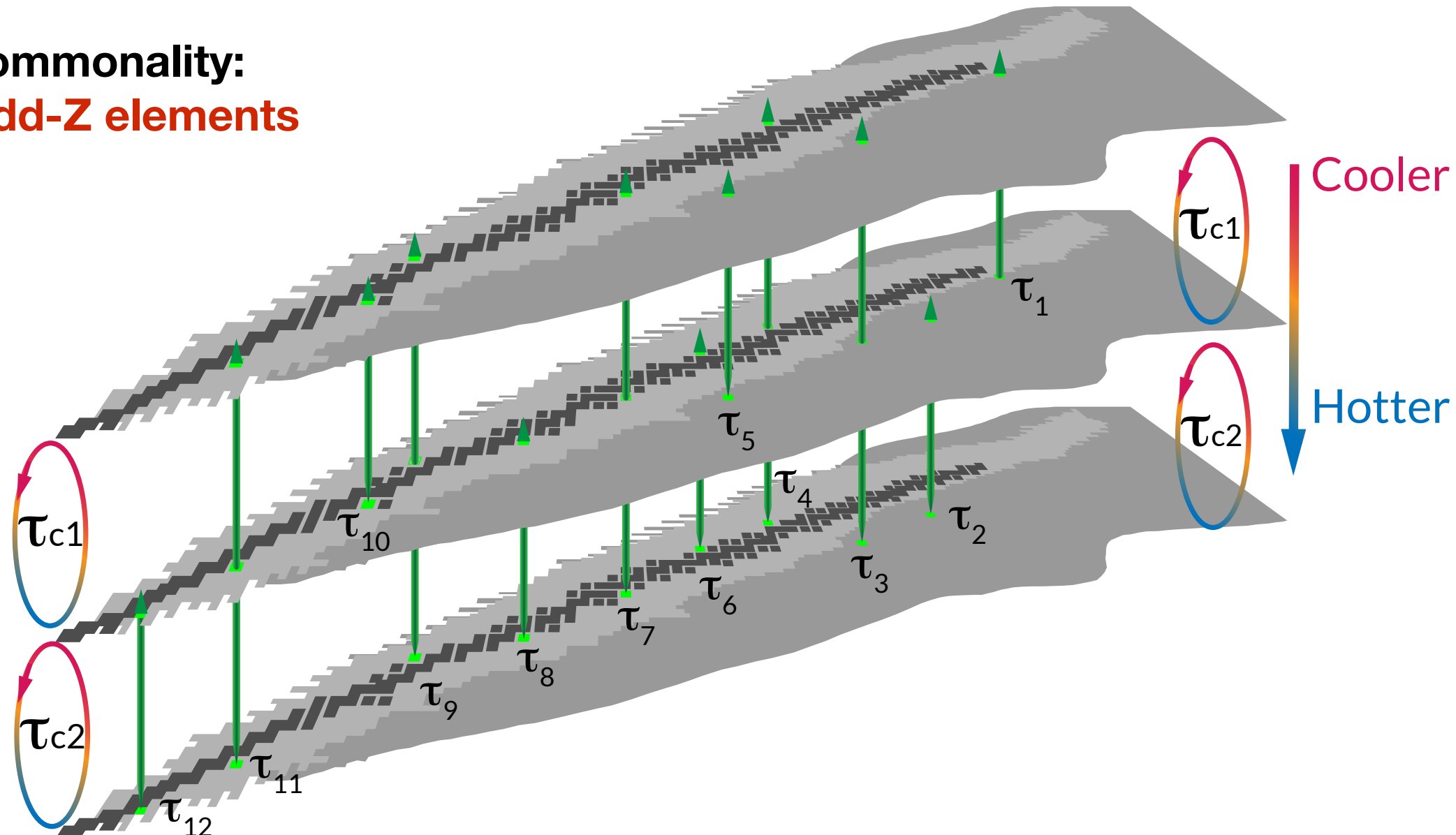
Convective-reactive nucleosynthesis



Family of nucleosynthetic sites in which nucleosynthesis is coupled with mixing.

- hot-bottom burning in massive AGB stars: **N, Li**
- H-ingestion in He-shell flashes RWDs, Sakurai's object, low-Z AGB: **Li, i process**
- O-C shell mergers in massive stars: **P, Cl, K, Sc (Ritter+ 17)**
- H-He shell mergers in Pop III massive stars: **Na, Al**
- slow mixing and burning in post-He+CO WD merger pre-RCB: **F, s-process**

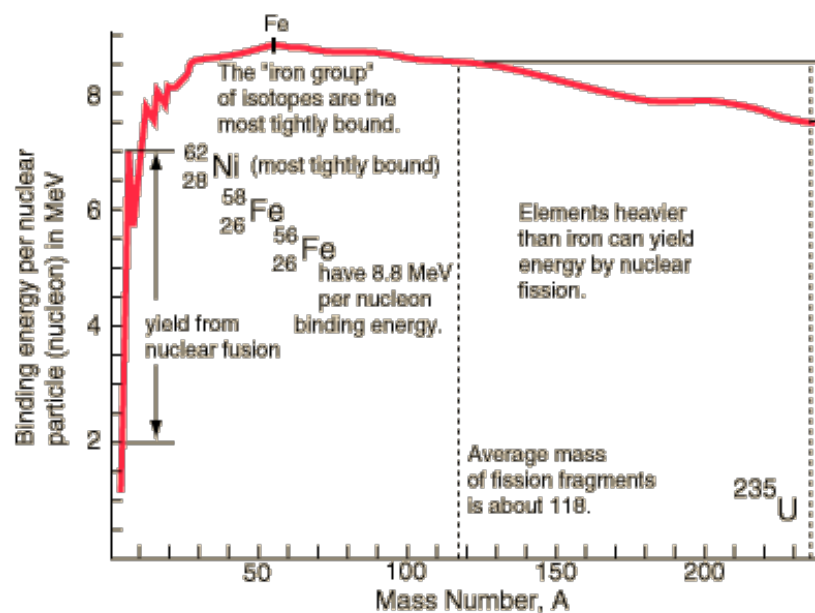
**interesting commonality:
production of odd-Z elements**



The End

Neutron capture nucleosynthesis

82



Binding Energy
per nucleon
peaks at Fe

Trans-iron elements are made by neutron capture nucleosynthesis

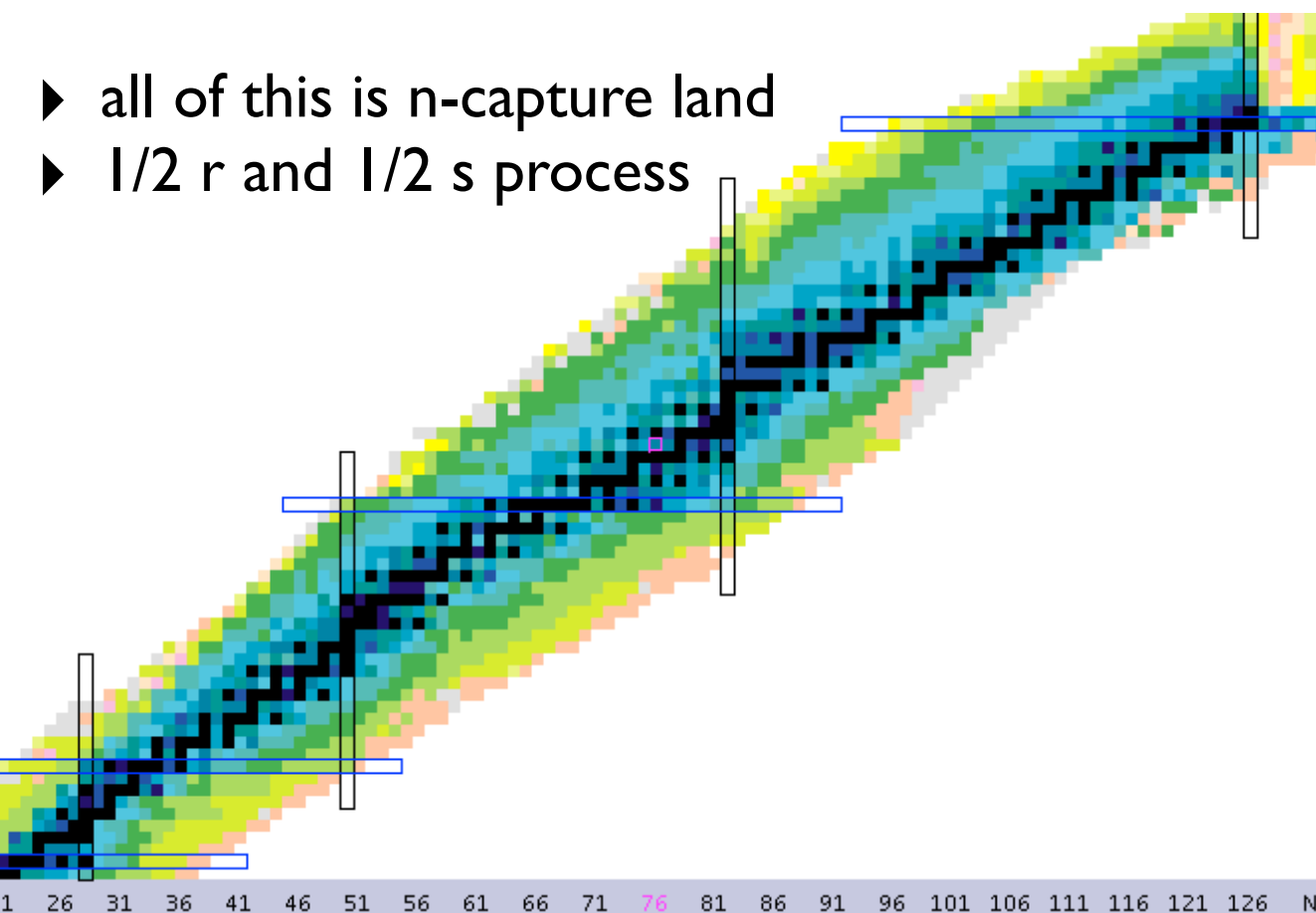


rapid n-capture process
(r process)

$$\tau_\beta > \tau_{(n,\gamma)}$$

$$N_n \approx 10^{20} \text{ cm}^{-1}$$

- ▶ all of this is n-capture land
- ▶ 1/2 r and 1/2 s process

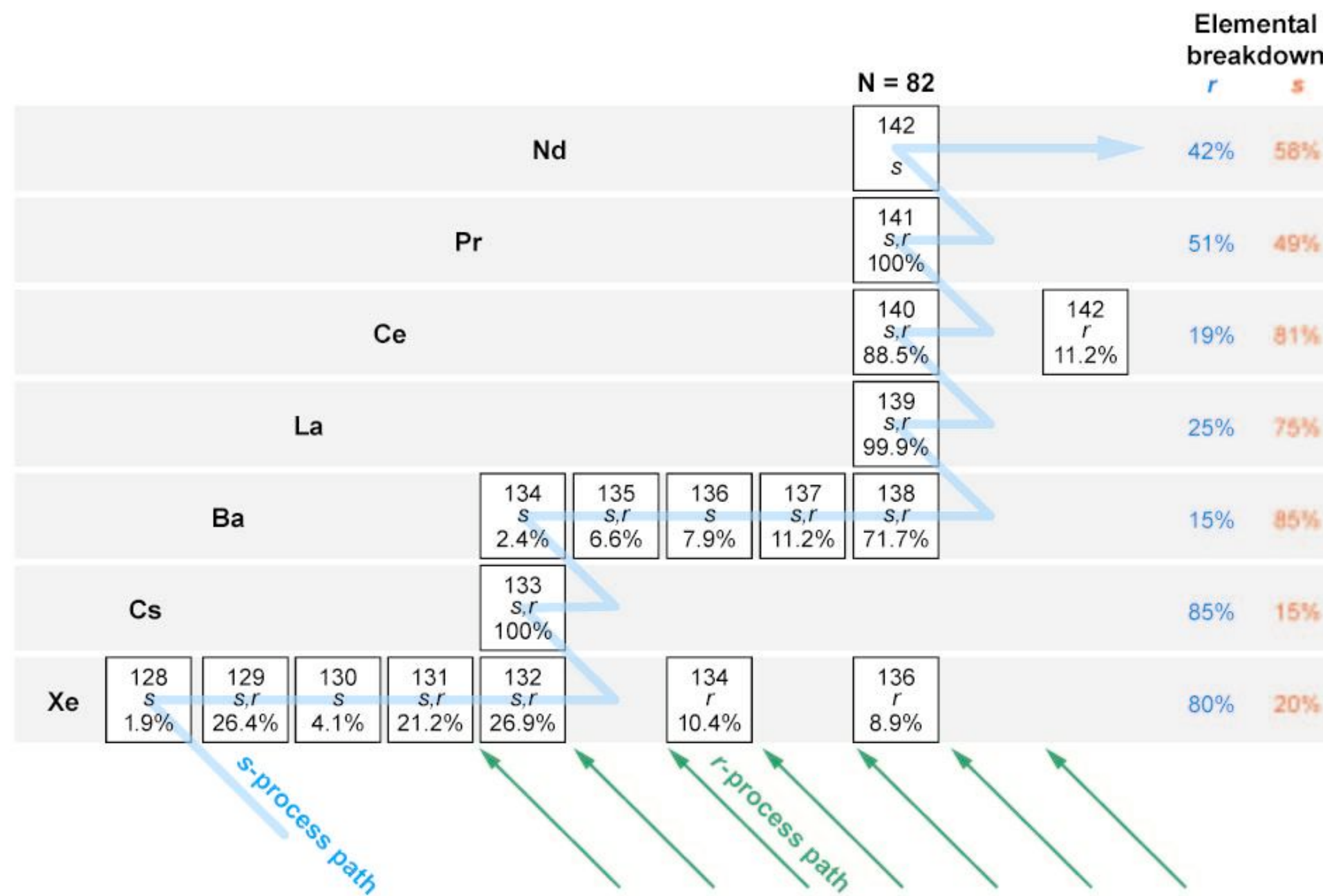


slow neutron capture process

$$\tau_\beta < \tau_{(n,\gamma)}$$

$$N_n \approx 10^7 - 10^{11} \text{ cm}^{-1}$$

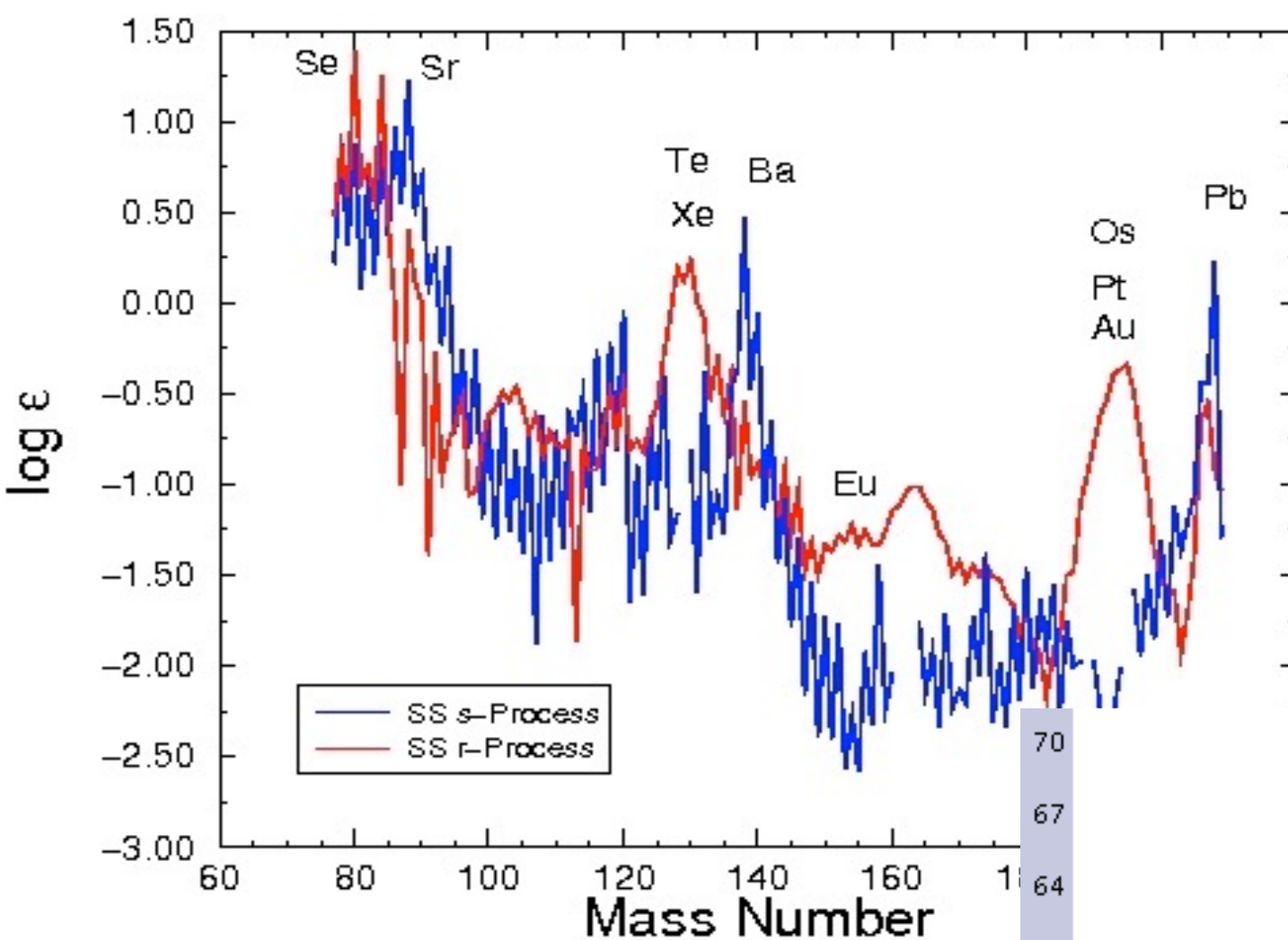
- ▶ there are two main neutron source reactions: $^{13}\text{C}(\alpha, n)^{16}\text{O}$ and $^{22}\text{Ne}(\alpha, n)^{25}\text{Mg}$
- ▶ typical neutron densities for s process are $N_n \sim 10^7 \dots 10^{11} \text{ cm}^{-1}$



A Sneden C, et al. 2008.
R Annu. Rev. Astron. Astrophys. 46:241–88

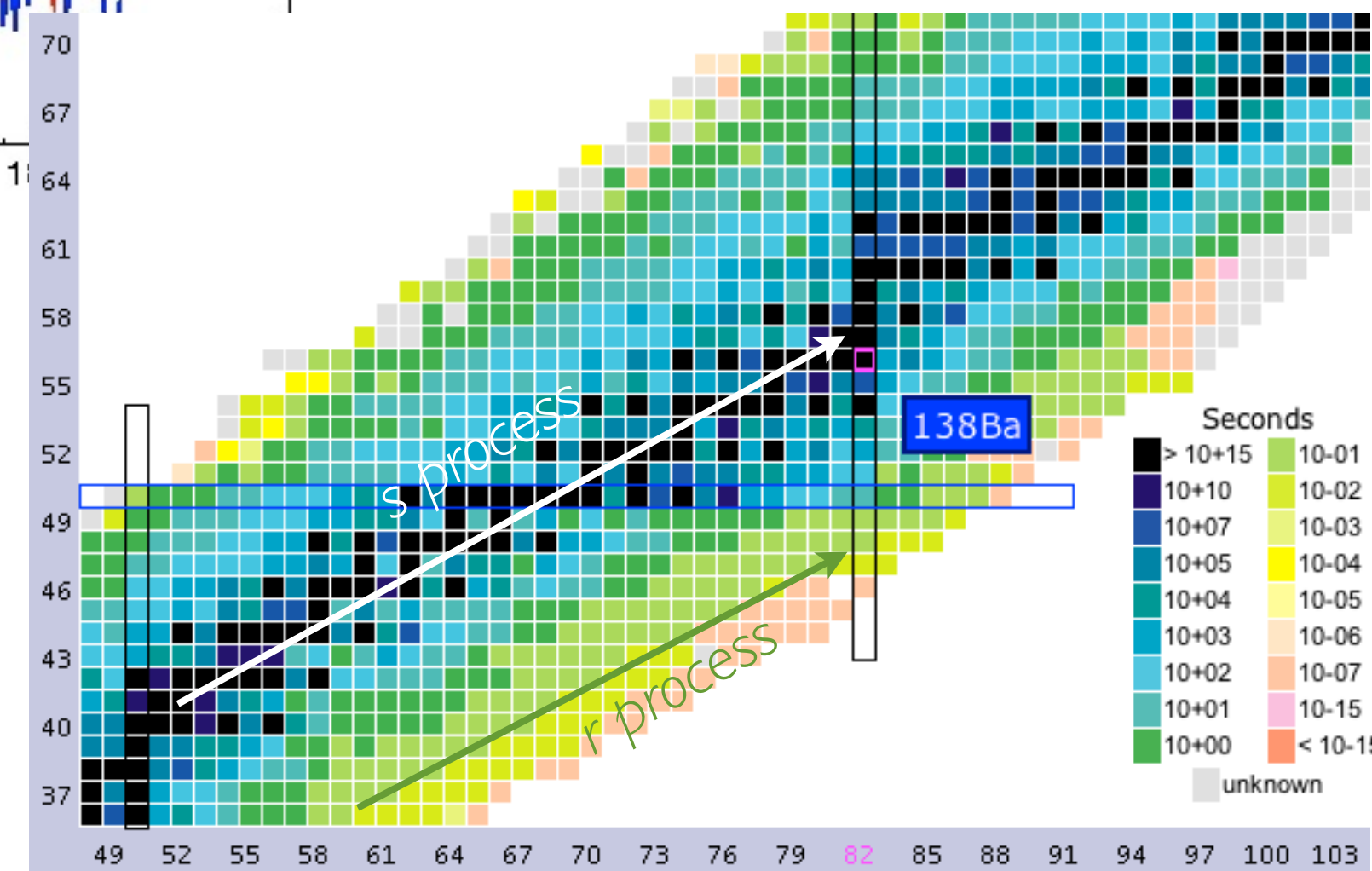
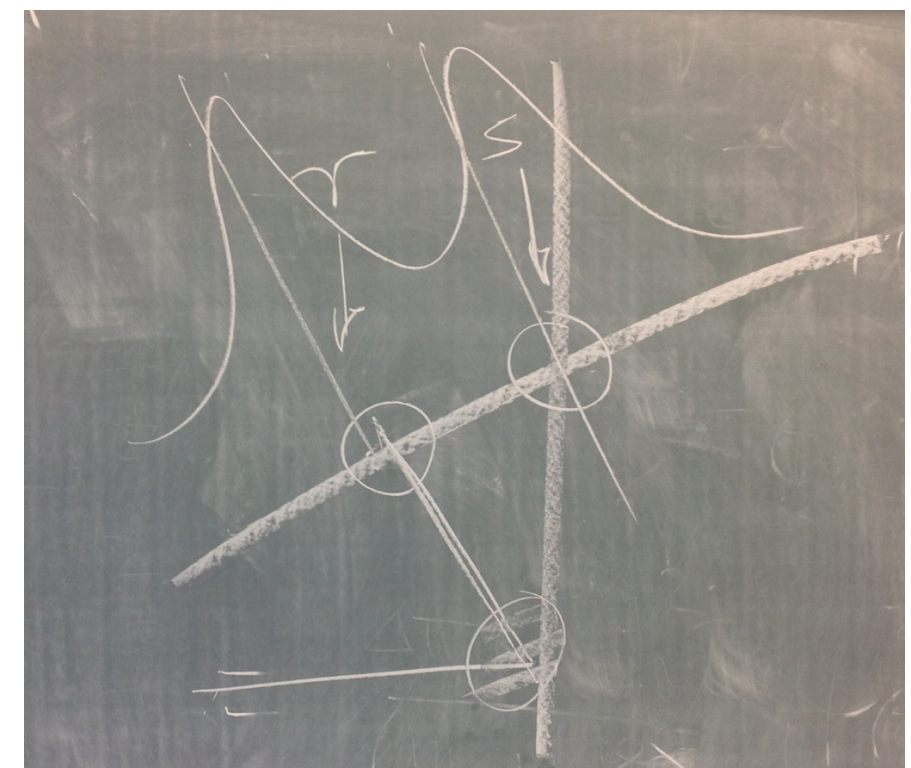
The solar system abundance distribution

84



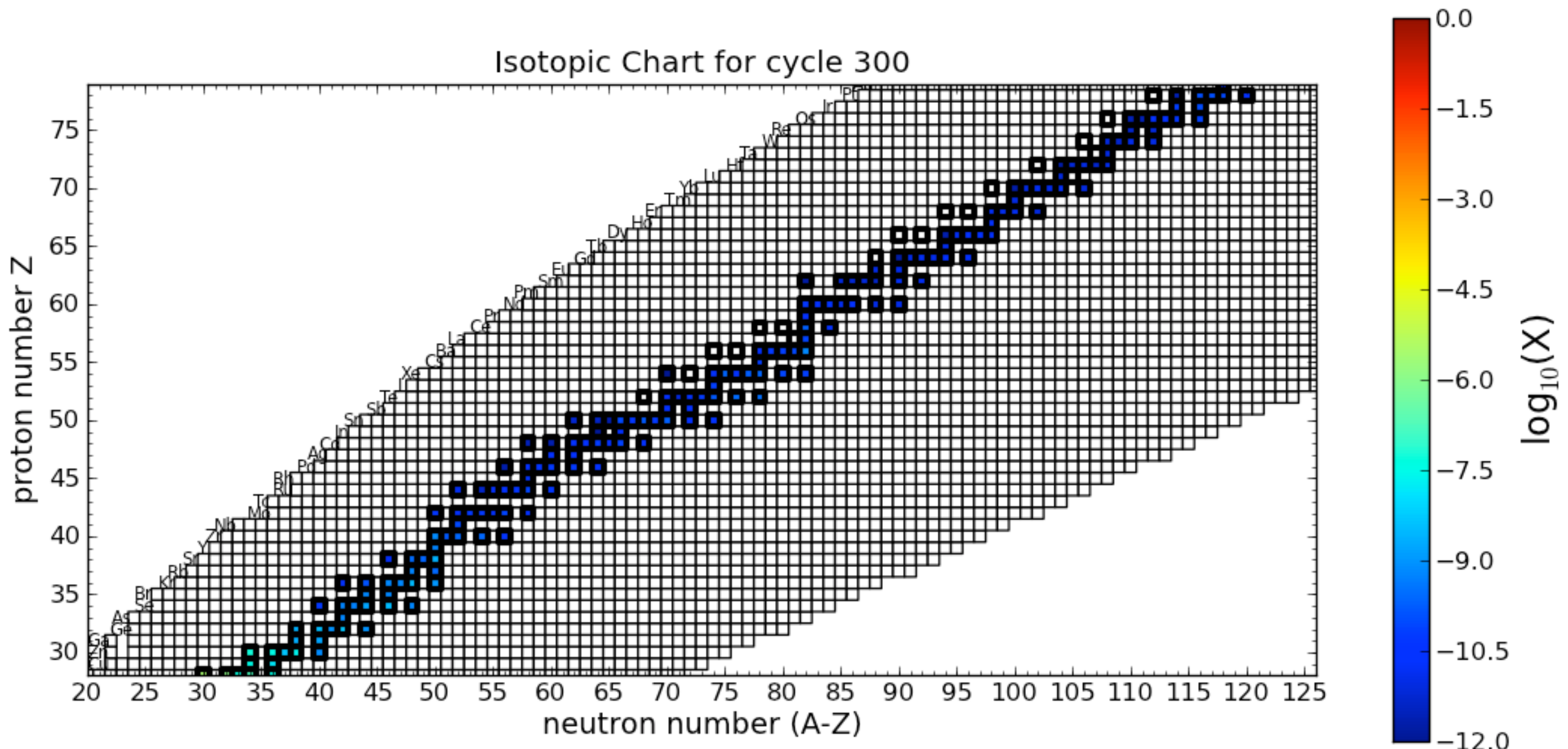
Sneden & Cowan 2003

Rapid vs. slow neutron capture process



i process nucleosynthesis with high neutron exposure

85



i process nucleosynthesis with high neutron exposure

86

